

Solving Inverse Problems for Medical Applications

Inaugural dissertation

to
be awarded the degree of

Dr. sc. med.

presented at
the Faculty of Medicine
of the University of Basel

by
Carlo Seppi
from Spreitenbach AG, Switzerland

Basel, 2023

Original document stored on the publication server of the University of Basel
edoc.unibas.ch

Solving Inverse Problems for Medical Applications by Carlo Seppi is licensed under CC BY 4.0

Approved by the Faculty of Medicine
on application of

Prof. Dr. Philippe C. Cattin – *primary advisor*
University of Basel, Switzerland

Prof. Dr. Azhar Zam – *secondary advisor*
New York University, Abu Dhabi (NYUAD), UAE
New York University, Tandon School of Engineering, USA

Prof. Dr. Dmitry Batenkov – *external expert*
Tel Aviv University, Israel

Dr. Uri Nahum – *further advisor*
University of Basel, Switzerland

Dr. Antal Huck – *further advisor*
University of Basel, Switzerland

Basel, 08.05.2023

Prof. Dr. Primo Schär
Dean

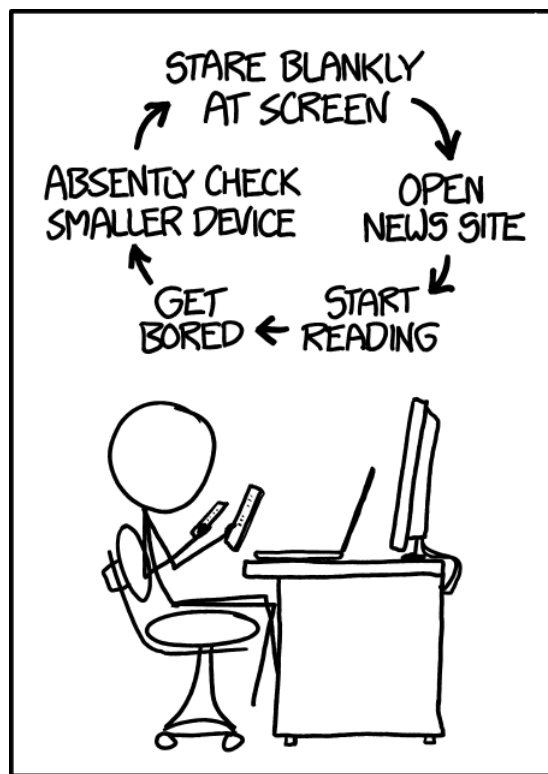
Dedication

*This is dedicated to the animal companions who were part of my life:
Muzungu, Natas, Satoru, Fridolin, and all the spiders living in my apartment.*

Preface

In which right is wrong and we refuse to accept it.
– *Unravel Two*

One of the greatest challenges of a mathematician is when math collides with the real world. A theory can be compared to a flower. A seed is planted, and it grows over time. It might grow into a lovely flower or even a tree. But like most things in life, it must end at one point. E.g., if a new theory makes more sense, the old one becomes obsolete. Solving a problem may work theoretically, or at least the approach seems to be a great idea, but the application in the real world may not work at all. There the fun begins: Rethink, Simplify, and Repeat. This is done until, at one point, you are satisfied with the results; or give up.



<https://xkcd.com/1411/>

e82a8262ae6f09505e37f633e433acc95488aa22af3d288555ac21a13ea1f218

Contents

<i>Acknowledgements</i>	vii
<i>Summary</i>	viii
<i>Zusammenfassung</i>	x
1 Introduction	1
1.1 MIRACLE – Project	1
1.2 Contribution	2
1.3 Outline of the Thesis	3
2 Technical Background	4
2.1 Forward Problem	4
2.2 Inverse Problem	6
2.3 Linear Models	8
2.4 Non-linear Models	10
2.5 Optimization Algorithms	11
2.5.1 Conjugate Gradient (CG) algorithm	11
2.5.2 Gradient Descent (GD)	13
2.5.3 Armijo–Goldstein condition	13
2.5.4 Gauss–Newton (GN) and Conjugate quasi-Newton (CqN) algorithm . .	14
2.5.5 Examples	16
2.6 Partial Differential Equation (PDE)	21
2.6.1 Finite Difference (FD)	22
2.6.2 Finite Elements (FE)	24
2.7 Neural Networks (NN)	26
2.7.1 Fully Connected Layers	27
2.7.2 Convolutional Layers	28
2.7.3 Maxpool Layer	31
2.7.4 Activation Function: ReLU	32
3 Sentinel Lymph Node Fingerprinting	33
4 Joint Inverse Medium and Optimal Control Problem	51

5	Bone Ablation Depth Approximation from Acoustic Waves	61
6	Discussion and Conclusion	71
6.1	Reconstruction of Tc ^{99m} Sources	71
6.1.1	Contribution	71
6.1.2	Conclusion and Future Work	72
6.2	Reconstruction using Acoustic Waves	72
6.2.1	Contribution	73
6.2.2	Conclusion and Future Work	73
6.3	Final Thoughts	74
7	Appendix	75
	Bibliography	78
	<i>Curriculum Vitae</i>	86

Acronyms

AR Augmented Reality. [vii](#), [1](#), [2](#)

CG Conjugate Gradient. [3](#), [11](#), [12](#), [14](#), [16–18](#), [72](#)

CNN Convolutional Neural Network. [26](#)

CqN Conjugate quasi-Newton. [iv](#), [viii](#), [x](#), [3](#), [10](#), [11](#), [14](#), [16](#), [19–21](#)

CT Computed Tomography. [1](#), [26](#)

Er:YAG Erbium-doped Yttrium Aluminium Garnet. [1–3](#), [51](#), [73](#)

FD Finite Difference. [iv](#), [3](#), [21–24](#)

FE Finite Elements. [iv](#), [3](#), [21](#), [22](#), [24](#), [61](#)

GD Gradient Descent. [iv](#), [3](#), [10](#), [11](#), [13](#), [14](#), [19–21](#)

GN Gauss Newton. [iv](#), [3](#), [10](#), [11](#), [14–16](#), [19–21](#)

MSELoss Mean Squared Error Loss. [11](#), [14](#), [15](#), [20](#)

NN Neural Network. [viii](#), [x](#), [3](#), [26](#), [28](#), [31](#), [61](#), [73](#), [74](#)

OCT Optical Coherence Tomography. [2](#), [3](#), [73](#)

PDE Partial Differential Equation. [3](#), [21](#), [22](#), [24](#), [25](#)

ReLU Rectified Linear Unit. [3](#), [32](#)

SLN Sentinel Lymph Node. [viii](#), [x](#), [2](#), [33](#), [72](#)

SLNF Sentinel Lymph Node Fingerprinting. [33](#)

Tc^{99m} Technetium-99m. [v](#), [vii](#), [2](#), [3](#), [5](#), [7](#), [33](#), [71](#), [72](#)

VR Virtual Reality. [1](#)

WSPGL1 Weighted Projected Gradient for ℓ_1 -norm Minimization. [71](#), [72](#)

Acknowledgements

I want to thank my supervisor Prof. Dr. Philippe C. Cattin, for allowing me to dive into the applied world of mathematics at the DBE. During all these years, he has always supported and encouraged me in my studies. In addition, I want to thank my second supervisor Prof. Dr. Azhar Zam, for giving me the opportunity and guidance to conduct the experiments. My deepest gratitude goes to the two postdocs who supervised me: Dr. Uri Nahum and Dr. Antal Huck. Your knowledge and insights helped me better understand my projects and conquer my obstacles, and your never-ending patience in repeatedly correcting my papers improved my writing skills. Prof. Dr. Georg Rauter, Dr. Ferda Canbaz, and Florentin Bieder: I want to thank you for your helpful discussions about my projects. A special thanks to my collaborators of the Journal Club: Dr. Arsham Hamidi, Dr. Eva Schneider, Dr. Samaneh Manavi, Mohammad Nahhas, and Dr. Sandra Drusovam. Your collaboration helped me get new ideas, algorithms, and data I could use during my studies. Of course, I want to mention Peter von Niederhäusern. You introduced me to my first applied mathematical problem. And it was fascinating to design the collimator, take the measurement of Tc^{99m} at the university hospital, analyze the data, and in the end, have an almost real-time visualization of the Tc^{99m} source with the AR glasses.

I was in the Planning and Navigation group (Dr. Uri Nahum, Dr. Antal Huck, Dr. Sara Freund, Dr. Lorenzo Iafolla, Dr. Samaneh Manavi, Marek Zelechowski, Dr. Eva Schneider, Balázs Faludi, Massimiliano Filipozzi, Madina Kojanazarova, and H el ene Corbaz). Thank you very much for the excellent discussion and the coffee breaks. It made work much more pleasant, and I appreciated it. And a thank you to the other CIAN and MIRACLE Group members, who are too many to list all of you here.

Thank you, Corinne Eymann-Baier, Hannah Heissler, Dr. Gabriela Oser, Dr. Sara Freund, Dr. Daniela Vavrecka-Sidler and Dr. Constanze Pfeiffer for helping me with all the organization and bureaucracy the university had to offer. We would not be able to work if we did not have an excellent IT infrastructure, for which I thank Dr. Beat Fasel and Norbet Zentai. I always enjoyed our discussions; it is incredible that you still push for open-source solutions!

Another great experience, which gave us intergroup team building, was the kicker matches we had. Thanks, Massimiliano, C edrick, Lorin, H el ene, Mohammad, Simon, Stefan, Bekim, Georg, Hans, and many more. And of course, I want to thank my friends and relatives, who supported me: Anna, Gianni, Jenny, Hans, Jacqueline, Petra, Ngoloke, Caterina, Dora, Sebastian, Hanna, Eliza, Marco, Salome, Franco, Alessia, Joel, Mischa, Norman, Carla, Carole, Patrick, Tobi, Dennis, Oliver, Ellie, Timo, the other Timo, and the third Timo.

Summary

It is essential to have an accurate feedback system to improve the navigation of surgical tools. This thesis investigates how to solve inverse problems using the example of two medical prototypes. The first aims to detect the [Sentinel Lymph Node \(SLN\)](#) during the biopsy. This will allow the surgeon to remove the [SLN](#) with a small incision, reducing trauma to the patient. The second investigates how to extract depth and tissue characteristic information during bone ablation using the emitted acoustic wave.

We solved inverse problems to find our desired solution. For this purpose, we investigated three approaches: In Chapter 3, we had a good simulation of the forward problem; namely, we used a fingerprinting algorithm. Therefore, we compared the measurement with the simulations of the forward problem, and the simulation that was most similar to the measurement was a good approximation. To do so, we used a dictionary of solutions, which has a high computational speed. However, depending on how fine the grid is, it takes a long time to simulate all the solutions of the forward problem. Therefore, a lot of memory is needed to access the dictionary.

In Chapter 4, we examined the Adaptive Eigenspace method for solving the Helmholtz equation (Fourier transformed wave equation). Here we used a [Conjugate quasi-Newton \(CqN\)](#) algorithm. We solved the Helmholtz equation and reconstructed the source shape and the medium velocity by using the acoustic wave at the boundary of the area of interest. We accomplished this in a 2D model. We note, that the computation for the 3D model was very long and expensive. In addition, we simplified some conditions and could not confirm the results of our simulations in an *ex-vivo* experiment.

In Chapter 5, we developed a different approach. We conducted multiple experiments and acquired many acoustic measurements during the ablation process. Then we trained a [Neural Network \(NN\)](#) to predict the ablation depth in an end-to-end model. The computational cost of predicting the depth is relatively low once the training is complete. An end-to-end network requires almost no pre-processing. However, there were some drawbacks, e.g., it is cumbersome to obtain the ground truth.

This thesis has investigated several approaches to solving inverse problems in medical applications. From Chapter 3 we conclude that if the forward problem is well known, we can drastically improve the speed of the algorithm by using the fingerprinting algorithm. This is ideal for reconstructing a position or using it as a first guess for more complex reconstructions. The conclusion of Chapter 4 is that we can drastically reduce the number of unknown parameters using Adaptive Eigenspace method. In addition, we were able to reconstruct the medium velocity and the acoustic wave generator. However, the model is expensive for 3D simulations.

Also, the number of transducers required for the setup was not applicable to our intended setup. In Chapter 5 we found a correlation between the depth of the laser cut and the acoustic wave using only a single air-coupled transducer. This encourages further investigation to characterize the tissue during the ablation process.

Zusammenfassung

Um die Navigation von chirurgischen Instrumenten zu verbessern, ist ein genaues Feedbacksystem unerlässlich. In dieser Arbeit wurde untersucht, wie ein inverses Problem bei zwei medizinischen Prototypen gelöst werden kann. Das erste zielt darauf ab, die Sentinel-Lymphknoten (SLN) während der Biopsie zu erkennen, damit diese minimal invasiv entfernt werden, was das Trauma des Patienten verringert. Das zweite Projekt befasst sich mit der Frage, wie wir während der Knochenabtragung mithilfe der emittierten akustischen Welle Informationen gewinnen können.

Wir untersuchten drei Ansätze, wie wir die inversen Probleme lösen können: In Kapitel 3 hatten wir eine gute Simulation des Vorwärtsproblems. Wir verglichen die Messung mit den Simulationen des Vorwärtsproblems. Die Simulation, die der Messung am ähnlichsten war, stellt eine gute Lösung dar. Je nachdem, wie fein das Gitter ist, dauert es jedoch sehr lange, alle Lösungen für das Vorwärtsproblem zu simulieren, bzw. es wird viel Arbeitsspeicher benötigt, um auf alle Simulationen zuzugreifen.

In Kapitel 4 lösten wir die Helmholtz-Gleichung (Fourier-transformierte Wellengleichung). Hier verwendeten wir einen [Conjugate quasi-Newton \(CqN\)](#)-Algorithmus um die Form der Quelle und die Mediumgeschwindigkeit zu rekonstruieren. Wir haben dies in einem 2D-Modell durchgeführt. Die Berechnung für das 3D-Modell war sehr lange und rechenintensiv. Wir weisen darauf hin, dass wir einige Bedingungen vereinfachten und die Ergebnisse unserer Simulationen nicht in einem *Ex-vivo*-Experiment bestätigen konnten.

Daher beschlossen wir in Kapitel 5 einen anderen Ansatz zu verwenden. Wir führten mehrere Experimente durch und erfassten viele akustische Messungen während des Ablationsprozesses des Knochens. Dann trainierten wir ein Neuronales Netzwerk (NN), um die Tiefe des Schnittes in einem End-to-End-Modell vorherzusagen. Es handelte sich um ein End-to-End-Netzwerk, was bedeutet, dass fast keine Datenvorverarbeitung benötigt wird. Allerdings gab es auch einige Nachteile, z. B. war es mühsam, die akustische Messung mit der dazugehörigen Tiefe zu kennzeichnen.

In dieser Arbeit wurden mehrere Ansätze zur Lösung inverser Probleme in medizinischen Anwendungen untersucht. Aus Kapitel 3 lernten wir, dass wir, wenn das Vorwärtsproblem gut bekannt ist, die Geschwindigkeit des Algorithmus erheblich verbessern konnten, indem wir den fingerprinting-Algorithmus verwendeten. Dies ist ideal für die Rekonstruktion einer Position oder als erster Ansatz für komplexere Rekonstruktionen. Die Schlussfolgerung aus Kapitel 4 ist, dass wir die Anzahl der unbekannt Parameter mit der adaptiven Eigenschaftsmethode erheblich reduzieren können. Ausserdem können wir die Mediumgeschwindigkeit und den akustischen Wellengenerator rekonstruieren. Allerdings war das Modell für 3D-Simulationen sehr

rechenintensiv. Die Anzahl der Mikrophone, die für das Experiment erforderlich waren, war für unsere geplante Einrichtung nicht anwendbar. In Kapitel 5 haben wir eine Korrelation zwischen der Tiefe des Laser-Schnitts und der akustischen Welle unter Verwendung nur eines luftgekoppelten Mikrophones gezeigt. Das ermutigt weitere Untersuchungen, um das Gewebe während des Ablationsprozesses zu charakterisieren.

Chapter 1

Introduction

1.1 MIRACLE – Project

An important feature of modern medicine is not only treating and curing patients but also improving their quality of life. One way of improving a patients quality of life is to decrease the recovery time after medical procedures such as surgery. The reduction of the recovery time has an additional advantage, namely, that the risk of accompanying illnesses is reduced. This reduction can be achieved by performing minimally invasive procedures [36, 56]. For example, in an osteotomy (the surgical cutting of a bone), the recovery time is decreased by replacing the mechanical tools used in open osteotomies with laser-based ablation [5, 7, 50, 55]. Another development is using robots during surgery, to improve the quality of the cut [16, 46]. Using such robots not only reduces the patient’s healing process but also improves the lifespan of an implant if cement-less fixation is used [70].

The first robotic device in clinics with a free-space laser used for laser-osteotomy is called CARLO[®] (short for “Cold Ablation Robot-guided Laser Osteotome”) [4, 6, 7, 19]. This robot guides the Er:YAG laser along a preplanned cutting path with the help of an optoelectronic tracking system which is previously registered with the Computed Tomography (CT) data from the patient. However, the surgeon’s incision on the patient has to expose the bone so that CARLO[®] can proceed with the ablation of the bone.

To further improve the recovery time, the Flagship project *MIRACLE*¹ (short for “Minimally Invasive Robot-Assisted Computer-guided LaserosteotomE”) was founded at the Department of the Biomedical Engineering of the University of Basel [73]. Their vision is to enable laser osteotomy in minimally invasive surgery, meaning that not the entire bone has to be exposed, but solely a one-centimeter wide incision is needed. Four research groups tackle the MIRACLE project: The group *Planning and Navigation*² dedicate themselves to improving the planning process using Virtual Reality (VR) and Augmented Reality (AR) glasses [27, 43, 57, 91–93] and to have an automated labeling system of the CT images from bones [75–77]. In addition, they develop novel approaches to navigate the endoscope, namely to reconstruct the position of the endoscope accurately [37–39, 58, 59, 74]. Finally, we opt to control the depth of the cut

¹17.03.2023, dbe.unibas.ch/en/research/flagship-project-miracle

²17.03.2023, dbe.unibas.ch/en/planning-navigation

during laser ablation and to analyze the surrounding using the acoustic wave emitted during the ablation process [65, 67, 78]. The second group is called *Biomedical Laser and Optics Group (BLOG)*³. They study the ablation process of different lasers [1, 13–15, 15] and develop a fiber-based laser that can be integrated into the endoscope. In addition, they want to integrate *Optical Coherence Tomography (OCT)* to get additional information of the tissue being ablated [8, 9] and investigate tissue differentiation using acoustic waves [44, 68]. The third group is called *Bio-Inspired Robots for MEDicine-Laboratory (BIROMED-Lab)*⁴, and their goal is to build the robotic endoscope. They are facing the challenge of making the flexible endoscope and controlling it safely [20, 24–26, 28]. The last group, called *Smart Implants*⁵, develops personalized bio-implants with durable 3D printed bio-materials [80] and will further investigate developing implants compatible with minimally invasive surgeries.

1.2 Contribution

The aim of this PhD thesis was to investigate inverse problems that occur in two potential medical devices. The first project investigates a new method to detect the *Sentinel Lymph Node (SLN)* during the biopsy in real time [66, 79, 84–86]. We helped design a pinhole collimator [66] using the optimal design algorithm [31]. In addition, we improved the computational speed to pinpoint the Tc^{99m} source using a fingerprinting algorithm [66]. One of the major achievements was that we were able to reconstruct the Tc^{99m} source using just a single measurement from the detector, hence reconstructing a 3D subspace using a 2D projection from the detector. The design of the collimator and the fingerprinting were then used for further research and as a base-line for the reconstruction [86, 87] to have a real-time reconstruction of the sources visualized with the *AR* glasses [85, 87]. Our vision is that our research will help the surgeon conduct a minimally invasive *SLN* biopsy.

In the second part, we investigated multiple approaches to aid the *MIRACLE* robot in navigating the endoscope and controlling the *Er:YAG* laser. An acoustic wave is emitted during tissue ablation with the *Er:YAG* laser. My task was to extract from these acoustic waves properties of the tissue being ablated. We solved the mathematical optimization problems to simultaneously reconstruct an unknown source of an acoustic wave and its surrounding medium velocity. Using the Adaptive Eigenspace method introduced in [63], we showed in [65] that this is, in fact, possible in the 2D subspace. We also managed to do so in a 3D subspace, but we noticed one major drawback: the computational time is very high. For real-time implementation, we either had to optimize the program and use high-performance computing or find another approach. When we tried to reconstruct the mathematical approach in the real world, we found some additional challenges we had not yet included in our simulations, one of them being the impedance between the bone and the air. A different challenge was that our simulation needs over 100 point transducers (simulated measurement at a single point on the coordinate system, but in reality, it stretches over multiple grid points) and did not include that the shape of the transducer that may influence the acoustic wave.

³17.03.2023, dbe.unibas.ch/en/research/laser-and-robotics/biomedical-laser-and-optics-group

⁴17.03.2023, dbe.unibas.ch/en/research/laser-and-robotics/bio-inspired-robots-for-medicine-lab

⁵17.03.2023, dbe.unibas.ch/en/research/laser-and-robotics/hightech-research-center-hfz/smart-implants

Therefore, we decided to change the methodology to analyze the acoustic wave. We bought tissue samples from the local grocery store, ablated the bone with our [Er:YAG](#) laser, and measured the depth of the cut with the [OCT](#). An acoustic wave is created during the ablation process, which we measured with an air-coupled transducer. The data were then used to train the [NNs](#). In our publication [78], we concluded that depth information is embedded in the acoustic wave. Although the experiments were performed in a dry environment, they encourage future scientists to further investigate this problem for deep bone ablation using an irrigation system.

1.3 Outline of the Thesis

In this chapter, we give an overview of the MIRACLE project and explain our contribution to the project. Chapter 2 will provide the reader with an understanding of the technical background. It will help the reader to understand what *Forward* and *Inverse Problems* are. Then we will explain what *Linear* and *Non-linear Models* are and give examples on how to solve them. We further introduce some *Optimization Algorithms*: [Conjugate Gradient \(CG\)](#), [Gradient Descent \(GD\)](#), [Gauss Newton \(GN\)](#), [Conjugate quasi-Newton \(CqN\)](#), and how to implement an adaptive step size with the *Armijo–Goldstein* condition. Then the *Partial Differential Equation (PDE)* is introduced, and how this can be solved with the help of *Finite Difference (FD)* and *Finite Elements (FE)*. In the final part, we give an overview of the *Neural Network (NN)* and describe the concepts of a *Fully Connected Layer*, *Convolutional Layer*, *Maxpool Layer*, and the *Rectified Linear Unit (ReLU)* activation function. Chapters 3-5 comprise the main contribution of this thesis, namely the publications. Chapter 3 introduces a method to find a good design for a pinhole collimator and how spatial distribution of a [Technetium-99m \(\$Tc^{99m}\$ \)](#) source can be reconstructed efficiently. Chapter 4 investigates the propagation of the acoustic wave and how to reconstruct the medium velocity and the source in an unknown environment. In Chapter 5, we use a [NN](#) to approximate the depth of the cut using the acoustic wave emitted during the bone ablation with an [Erbium-doped Yttrium Aluminium Garnet \(Er:YAG\)](#) laser. In Chapter 6 we discuss our results and what we learned from the project. Finally, Appendix in Chapter 7 has proofs of theorems used to explain some of the technical backgrounds in Chapter 2.

Chapter 2

Technical Background

2.1 Forward Problem

According to the encyclopedia¹, a forward problem is

“[...] the problem of calculating what should be observed for a particular model”.

This means that a forward problem can fit or predict the results of an outcome for a particular condition. In everyday life, we apply forward problems without even noticing. For example, when we buy groceries, each grocery is mapped to a particular value, or when we play billiards, we approximate how the ball rolls according to its surroundings and the angle at which we hit the ball.

We now look at a more mathematical example. Assume, we have two sets of numbers. $\mathcal{A} = \{0, 1, 2, 3, 4, \dots\} = \mathbb{N}_0$ with all the natural numbers (including 0) and $\mathcal{B} = \{0, 1, 2, 3, 4\}$. Our function g maps each of the numbers in \mathcal{A} to a number in \mathcal{B}

$$\begin{array}{ccc} g : \mathcal{A} & \longrightarrow & \mathcal{B} \\ a & \longmapsto & b \end{array} \quad \text{with } a \in \mathcal{A}, b \in \mathcal{B}. \quad (2.1)$$

There exists a simple function g , namely the *modulo 5* function, that maps \mathcal{A} onto \mathcal{B} : We can write each number $a \in \mathcal{A}$ as a combination of $n \in \mathbb{N}$, $p = 5$, and $b \in \mathcal{B}$

$$a = np + b,$$

hence, the function g can be written as follows

$$g(a) = g(np + b) = a \pmod{p} = b. \quad (2.2)$$

In other words: a divided by p is n remainder b . In this example, an element $a \in \mathcal{A}$ represents a condition and $b \in \mathcal{B}$ the corresponding outcome. The function g maps the element a to the element b ; hence, the function g is a forward problem. We show, in Table 2.1, some mapping from elements of the subset \mathcal{A} onto the elements of the subset \mathcal{B} using the mapping function

a	0	1	2	3	4	5	6	7	8	314 159 265 359	$2^{82\,589\,933} - 1$
b	0	1	2	3	4	0	1	2	3	4	1

Table 2.1: Sample mapping of the modulo 5 function $g(a) = b$.

$g(a) = b$. Note, that we prove Theorem 7.1 in the appendix, that $g(2^{82\,589\,933} - 1) = 1$ ($2^{82\,589\,933} - 1$ is the biggest known prime-number, at the time of writing).

The following example is more applied. The goal is to detect a Tc^{99m} source with a detector, and describe the relationship between the position of the source and the resulting image of the detector. Let the pinhole collimator be in front of a γ -ray detector, as visualized in Figure 2.1, and a Tc^{99m} source in front of the collimator. In this case, the forward problem is the projection of the Tc^{99m} source onto the detector. This can be done by simulating photons as a straight line from the Tc^{99m} source, through any of the pinholes, onto the detector.

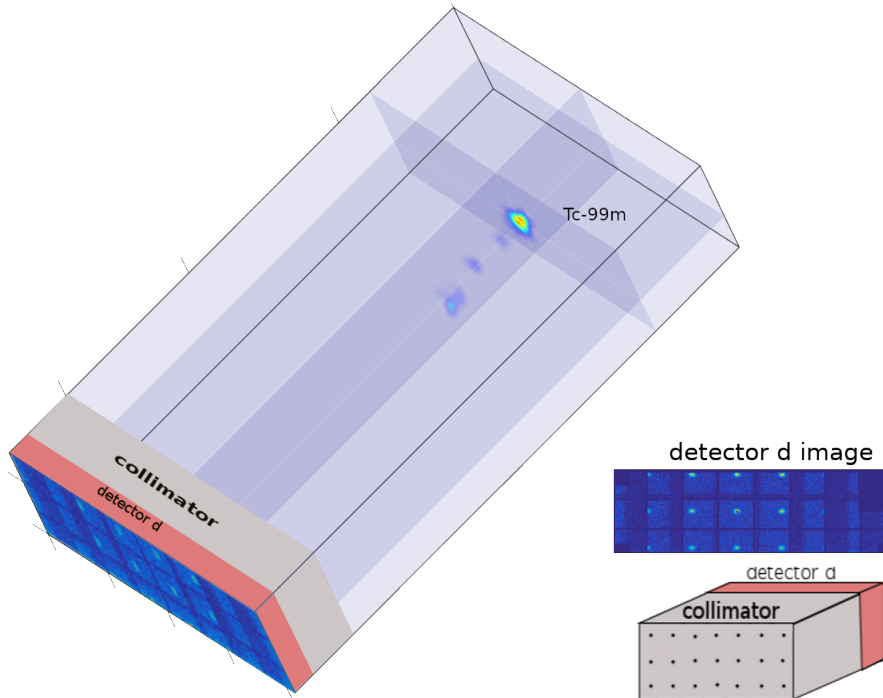


Figure 2.1: The schematic visualizes the setup: γ -rays from the Tc^{99m} source pass through the pinholes of the collimator and are projected onto the detector. The right side depicts an image from the detector, which is a measurement, and the front view of the collimator. The forward problem (Section 2.1) can thus be formulated as: For a given Tc^{99m} source simulate the projection on the detector; and the inverse problem (Section 2.2) as: Reconstruct the position of the Tc^{99m} source with the measurement from the detector.

For the final example, we look at the frequency spectrum of a standing wave. An acoustic

¹14.10.22, [encyclopedia.com/science/dictionaries-thesauruses-pictures-and-press-releases/forward-problem](https://www.encyclopedia.com/science/dictionaries-thesauruses-pictures-and-press-releases/forward-problem)

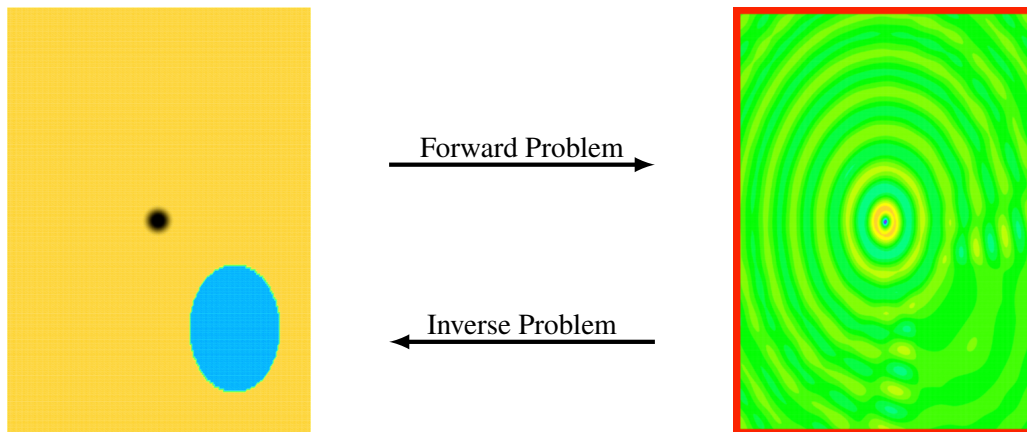


Figure 2.2: On the left side, we visualize an area of interest. In its center is an acoustic wave generator (black), and the area has two different medium velocities (yellow and blue). On the right side, we visualize the acoustic propagation through the various medium velocities, respectively the pressure variation at each point (variation of the colors means different amplitude of the pressure variation). The red box represents the positions of the transducers measuring the acoustic wave. The forward problem (Section 2.1) is then: We have the source information and the medium velocity of the objects (left side) and simulate the propagation of the acoustic wave (right side). The inverse problem (Section 2.2): Under which condition (for which source and for what medium velocity) the measured wave is created (information from the right side to reconstruct the left image).

wave is created from a source or wave generator, e.g., a loudspeaker. The acoustic wave has different propagation speeds within different mediums. For example, in air its medium velocity of 343 m s^{-1} and in water it is 1482 m s^{-1} . On the left side of Figure 2.2, we show an area with two different medium velocities and in its center, an acoustic source or wave generator is located. The forward problem simulates the propagation of the acoustic wave, respectively the pressure variation at each point, as is shown on the right side of Figure 2.2.

2.2 Inverse Problem

Contrary to the forward problem, the inverse problem uses a given observation or measurement to calculate under which conditions the measurement is observed.

Using previous examples, we will explain inverse problems and how to formulate them. The first example is grocery shopping. An example of an inverse problem is if a person goes grocery shopping and only knows how much they paid but does not know the price of each item. Hence, they have an observation “*how much they paid*” and are searching for the initial condition “*how much each item costs*”. It is obvious that without any additional boundary condition, or if the person does not have multiple receipts to evaluate, the problem has no unique solution. Gathering additional data will help the person estimate an initial validated condition: How much they paid for each item. The second example is a billiard game. Here, we observe how the ball

moves on the table and want to deduce the angle at which the ball was hit. Hence, our observation is *the movement of the ball*, and the unknown initial value is *at what angle the ball was hit*. There are also some unknown factors, like the friction of the table. Another parameter for the initial value is at what strength the ball was hit, for this, we need additional boundary conditions, e.g., the weight of the ball and its speed.

The example of Equation 2.1 can be transformed into an inverse problem: We have an observation $b \in \mathcal{B}$, and we are searching for the initial condition $a \in \mathcal{A}$. This can be written as follows

$$\text{for a given } b \in \mathcal{B} \text{ find } a \in \mathcal{A} \text{ s.t. } g(a) = b.$$

Hence, the solution for the inverse problem can be written as

$$\arg \min_a |g(a) - b|. \quad (2.3)$$

Solving this equation can give one or multiple different results. For example, let us assume that function g is the modulo function from Equation 2.2 with $p = 5$. Further, we now search for an initial condition $a \in \mathcal{A}$, which yields $g(a) = 1$. In Table 2.1 we see some possible solutions. We can generalize the results for all $a \in \mathcal{A}$ where

$$a = np + 1, \text{ for } n \in \mathbb{N}_0 \text{ and } p = 5,$$

hence, infinitely many solutions exist. Although all of these results are correct, we may search for a specific result, or better: A result that fulfills certain additional conditions. To this end, we can add some regularization $R(a)$ to Equation 2.3

$$\arg \min_a (|g(a) - b| + \gamma R(a)), \quad (2.4)$$

where $R(a) \geq 0$ is an arbitrary function $R : \mathcal{A} \rightarrow \mathbb{R}_{\geq 0}$ and γ is the regularization parameter $\gamma \in \mathbb{R}_{\geq 0}$. A simple example is when $R(a) = \|a\|_2$ is the Euclidean norm and $\gamma = 1$. When we solve Equation 2.4, then there exist exactly one solution for our example in Equation 2.2, namely,

$$a = 1.$$

Therefore, adding an appropriate regularization function can help find the desired minimum, hence, getting the initial conditions we are looking for.

Another example, is the inverse problems solved in Chapter 3. As previously described and visualized in Figure 2.1, the γ -rays emitted by the $\text{Tc}^{99\text{m}}$ source pass through the pinholes of the collimator and are detected by the detector. Let us formulate the inverse problem: For a given measurement, here, the image from the detector, we search for the condition under which the measurement was observed, i.e., the position of the $\text{Tc}^{99\text{m}}$ source.

The final example we give, is the propagation of the acoustic wave, which is an important part of Chapter 4. As described earlier, the Figure 2.2 visualizes the propagation of the wave in the frequency spectrum through various types of media. Solving the inverse problem involves reconstructing the different medium velocities in the area of interest from the measured acoustic waves.

2.3 Linear Models

This subsection describes how to solve an inverse problem using a linear model. We define

$$x \in \mathbb{R}^K \iff x = [x_1, \dots, x_K] \quad \text{with} \quad x_i \in \mathbb{R} \quad \text{for all} \quad i \in \{1, \dots, K\}.$$

Let the multivariate function g be

$$g : \mathbb{R}^K \longrightarrow \mathbb{R} \\ x \longmapsto y,$$

with the observation $y \in \mathbb{R}$ and the initial condition $x \in \mathbb{R}^K$. During an experiment, we might only know some initial condition parameters. We divide x into two parts: $t \in \mathbb{R}^{\tilde{K}}$ the experimental condition (known parameters of the initial condition) and $\theta \in \mathbb{R}^k$ the unknown parameters of the initial condition. Solving the inverse problem will find the initial condition θ with the given experimental condition t and the corresponding observation y . We can thus write

$$g : \mathbb{R}^K \longrightarrow \mathbb{R} \\ [t, \theta] \longmapsto y \quad \text{with} \quad K = \tilde{K} + k \quad \text{and} \quad x = [t, \theta].$$

During data collection, some random error ε distorts the model. Hence, we can write

$$y^{obs} = g(t^{obs}, \theta) + \varepsilon, \tag{2.5}$$

where ε can result from inaccuracies in the measuring device or a distorting of the model g .

The simplest relationship of a deterministic linear model [72] is when the parameters θ are linearly dependent on the known experimental condition t . Then, there are functions $f_i(t) : \mathbb{R}^{\tilde{K}} \longrightarrow \mathbb{R}$, that approximate the function g as a linear combination of the unknown parameters θ and the functions f_i :

$$f(t) = \begin{bmatrix} f_1(t) \\ \vdots \\ f_k(t) \end{bmatrix} \in \mathbb{R}^{k \times 1} \quad \text{and} \quad \theta = \begin{bmatrix} \theta_1 \\ \vdots \\ \theta_k \end{bmatrix} \in \mathbb{R}^{k \times 1} \quad \text{s.t.} \quad g(t, \theta) \approx f(t)^T \theta.$$

We note that $f(t)^T \in \mathbb{R}^{1 \times k}$ is the transpose of $f(t) \in \mathbb{R}^{k \times 1}$. Hence, we can deduce from Equation 2.5

$$y^{obs} = g(t^{obs}, \theta) + \varepsilon = f(t^{obs})^T \theta + \hat{\varepsilon}, \tag{2.6}$$

where $\hat{\varepsilon}$ is an error. To solve the inverse problem, we find the unknown parameters θ . When just a single unknown $\theta = \theta_1$ exists, then we have just a single function $f(t) = f_1(t)$. A good approximation θ_1 , can be found, when we use Equation 2.6 and get

$$y^{obs} = g(t^{obs}, \theta_1) + \varepsilon = f(t^{obs})^T \theta_1 + \hat{\varepsilon}.$$

For a sufficiently small error $\|\hat{\varepsilon}\|_2$ we can approximate

$$y^{obs} \approx f(t^{obs})^T \theta_1,$$

and a solution is found by minimizing the difference

$$\arg \min_{\theta} \left\| y^{obs} - f(t^{obs})^T \theta \right\|_2.$$

In fact, to find a solution for a single unknown it is sufficient to use one observation y^{obs}

$$\theta_1 = \frac{y^{obs}}{f_1(t^{obs})},$$

and therefore a good approximation for the unknown parameter θ , if $\|\hat{\varepsilon}\|_2$ is small enough. However, in most cases, we have multiple unknowns. We will now generalize the Equation 2.6 to a statistic linear model, with N observations and k unknown parameters θ . We assume that the unknown parameters stay the same for all N known experimental conditions $t_i^{obs} \in \mathbb{R}^{\hat{K}}$. Hence, the i -th observation $y_i^{obs} = g(t_i^{obs}, \theta) + \varepsilon_i$, can be approximated with the linear Equation 2.6 as

$$y_i^{obs} = g(t_i^{obs}, \theta) + \varepsilon_i = f(t_i^{obs})^T \theta + \hat{\varepsilon}_i,$$

with some error $\hat{\varepsilon}_i$. Further, generalizing for N observations, we get a $Y^{obs} \in \mathbb{R}^N$ with

$$\begin{aligned} Y^{obs} &= \begin{bmatrix} y_1^{obs} \\ \vdots \\ y_N^{obs} \end{bmatrix} = \begin{bmatrix} f(t_1^{obs}) & \cdots & f(t_N^{obs}) \end{bmatrix}^T \begin{bmatrix} \theta_1 \\ \vdots \\ \theta_k \end{bmatrix} + \begin{bmatrix} \hat{\varepsilon}_1 \\ \vdots \\ \hat{\varepsilon}_k \end{bmatrix} \\ &= \begin{bmatrix} f_1(t_1^{obs}) & \cdots & f_1(t_N^{obs}) \\ \vdots & \ddots & \vdots \\ f_k(t_1^{obs}) & \cdots & f_k(t_N^{obs}) \end{bmatrix}^T \begin{bmatrix} \theta_1 \\ \vdots \\ \theta_k \end{bmatrix} + \begin{bmatrix} \hat{\varepsilon}_1 \\ \vdots \\ \hat{\varepsilon}_k \end{bmatrix} \\ &= F(t^{obs})^T \theta + E \quad \text{for } t^{obs} = [t_1^{obs}, \dots, t_N^{obs}], \end{aligned} \quad (2.7)$$

where $F(t^{obs}) \in \mathbb{R}^{k \times N}$ is the linear combination of the observations $t^{obs} \in \mathbb{R}^{\hat{K} \times N}$, the unknown parameter $\theta \in \mathbb{R}^k$, and the error $E \in \mathbb{R}^k$. Again, we exploit that for a sufficiently small $\|E\|$ we have

$$Y^{obs} \approx F(t^{obs})^T \theta. \quad (2.8)$$

Therefore a good solution for θ can be found when solving Equation 2.8.

For simplification, we assume that all the linear equations are independent; hence, all columns of $F(t^{obs})$ are linearly independent. Then, we have three cases: The first case is when the number of k unknown parameters θ and number of N observations y_i^{obs} are equal ($k = N$); then there exists exactly one solution $\theta \in \mathbb{R}^k$. The second case is when we have more observations N than unknowns k . This is more robust against outliers in the observations, especially when $N \gg k$. In [72], many classical methods are described to find a good approximation in such a case. The third case is when the number of unknown parameters exceeds the number of observations. In fact, such a case is an ill-posed problem because more than one result exists. Therefore, additional boundary information to the unknown parameters θ can be given to find the desired solution. In [31], some numerical methods are proposed to solve an ill-posed statistical linear equation.

2.4 Non-linear Models

We can describe a non-linear model similarly to the beginning of Section 2.3 and Equation 2.6. For a given experimental condition $t \in \mathbb{R}^{\tilde{K}}$ and an observation $y \in \mathbb{R}$ we search for the initial condition $\theta \in \mathbb{R}^k$

$$\begin{aligned} g : \mathbb{R}^K &\longrightarrow \mathbb{R} \\ [t, \theta] &\longmapsto y \end{aligned} \quad \text{with } K = \tilde{K} + k \text{ and } x = [t, \theta].$$

As before, some random error ε can accrue that distorts the model. Hence, we write

$$y^{obs} = g(t^{obs}, \theta) + \varepsilon. \quad (2.9)$$

Some mathematical models, like the wave-equation, cannot be linearized. Therefore, we introduce an approach to solve non-linear inverse problems. Unlike in Section 2.3, we do not linearize the problem; we will not have a linear equation like Equation 2.8. Therefore, we will use optimization algorithms to solve Equation 2.9. In Section 2.5, we give some examples of algorithms to solve inverse problems, namely: **GD**, **GN**, and **CqN**. A further reading recommendation is the thesis of Eriksson [22] which gives an excellent overview of some optimization methods for non-linear models.

To solve the inverse problem, we need to rewrite Equation 2.9 into a minimization problem. If $\|\varepsilon\|_2$ is sufficiently small, then a good result for a given t^{obs} and the corresponding measurement y^{obs} is

$$\arg \min_{\theta} \left\| g(t^{obs}, \theta) - y^{obs} \right\|_2^2.$$

However, this may not give the desired output for multiple unknowns ($k > 1$). Hence, either some regularization needs to be added, or the number of observations has to be increased. When we have N observations, we get an observation y_i^{obs} for each experimental condition t_i^{obs} , with $i = 1, \dots, N$. We define the loss function $\mathcal{L}(\theta)$ as a dot product, with

$$G(t^{obs}, \theta) = \begin{bmatrix} g(t_1^{obs}, \theta) \\ \vdots \\ g(t_N^{obs}, \theta) \end{bmatrix} \quad \text{and} \quad Y^{obs} = \begin{bmatrix} y_1^{obs} \\ \vdots \\ y_N^{obs} \end{bmatrix}$$

as follows

$$\begin{aligned} \mathcal{L}(\theta) &= \frac{1}{2} \sum_{i=1}^N (g(t_i^{obs}, \theta) - y_i^{obs})^2 \\ &= \frac{1}{2} (G(t^{obs}, \theta) - Y^{obs})^T (G(t^{obs}, \theta) - Y^{obs}) \\ &= \frac{1}{2} \|G(t^{obs}, \theta) - Y^{obs}\|_2^2, \end{aligned} \quad (2.10)$$

and thus we have a good result for θ when solving the minimization problem

$$\arg \min_{\theta} \mathcal{L}(\theta) = \arg \min_{\theta} \left(\frac{1}{2} \sum_{i=1}^N (g(t_i^{obs}, \theta) - y_i^{obs})^2 \right).$$

We note that we use the [Mean Squared Error Loss \(MSELoss\)](#); however, a different loss function can be used. The condition that a loss function should fulfil is that it has a minimum at the desired result.

2.5 Optimization Algorithms

Optimization algorithms are an important part of numerical mathematics. In this section, we show, how to solve a linear model of the form

$$Ax = y, \quad (2.11)$$

with $A \in \mathbb{R}^{N \times M}$ and $x, b \in \mathbb{R}^M$ using the [CG](#) method and how to find the minimum of a function

$$\arg \min_{\theta} \mathcal{L}(\theta),$$

where $\mathcal{L} : \mathcal{A} \rightarrow \mathcal{B}$ is a derivable multi-variable function with $\mathcal{A} \subset \mathbb{R}^N$ and $\mathcal{B} \subset \mathbb{R}$, using the [GD](#), [GN](#), and [CqN](#) algorithms. These algorithms can also be used to solve non-linear models.

2.5.1 Conjugate Gradient (CG) algorithm

The [CG](#) Algorithm [34] is a popular numerical method to solve linear equations in the form of Equation 2.11. It is advantageous for solving large linear systems since it only uses matrix-vector multiplications. Hence, it is not as computationally heavy as matrix-matrix multiplications or finding the inverse of a matrix. To solve a linear equation of the form

$$Hx = b$$

with the [CG](#) algorithm the matrix H has to be positive definite, meaning

$H \in \mathbb{R}^{M \times M}$ is positive definite $\iff x^T H x > 0, \forall x \in \mathbb{R}^M \setminus \{0\}$, H is a symmetric real matrix.

We note that the matrix H can be written as

$$H = A^T A \in \mathbb{R}^{M \times M}$$

and is therefore symmetric, as shown in Theorem 7.2. In fact, we show in Theorem 7.3 that if H is invertible, it is positive definite. Hence, to solve the linear Equation 2.11 we multiply A^T on the left side and we get

$$Hx = b, \quad \text{with } b = A^T y \quad \text{and } H = A^T A$$

so that it can be solved with the [CG](#) algorithm. In Algorithm 1, we give a detailed description of the [CG](#) algorithm. We note that nowhere in the [CG](#) algorithm we compute

$$H = A^T A.$$

This is avoided by computing the matrix-vector multiplication

$$Hx = A^T(Ax).$$

To add additional regularization and to ensure that the matrix H is invertible and therefore positive definite, we can use

$$H = A^T A + \lambda E$$

for a $\lambda \in \mathbb{R}_{>0}$, where E is the identity matrix (instead of $H = A^T A$), as shown in Theorem 7.4. We note, if H is positive semidefinite

$$H \in \mathbb{R}^{M \times M} \text{ is positive semidefinite} \iff \begin{cases} x^T H x \geq 0, \forall x \in \mathbb{R}^M \setminus \{0\} \\ H \text{ is a symmetric real matrix} \end{cases},$$

and b is in the range space of H , then the CG method converges as well [33, 41].

Algorithm 1: The algorithm shows an implementation of the CG method, with three possible implementations to update β_n : (a.1) Polak-Ribière, (a.2) Fletcher-Reeves, and (a.3) Hestenes-Stiefel

Data: solve $Hx = b$, for H real, symmetric, positive definite matrix, b vector, x unknown

Result: find unknown x

x_0 initial guess ;

$r_0 \leftarrow b - Hx_0$;

$p_0 \leftarrow r_0$;

$n \leftarrow 0$;

while $\|r_n\|$ is not small enough **do**

$$\tau_n \leftarrow \frac{r_n^T r_n}{p_n^T H p_n} ;$$

$$x_{n+1} \leftarrow x_n + \tau_n p_n ;$$

$$r_{n+1} \leftarrow r_n - \tau_n H p_n ;$$

calculate β_n ;

$$(a.1) \beta_n \leftarrow \frac{r_{n+1}^T r_{n+1}}{r_n^T r_n} \quad (\text{Polak-Ribière});$$

$$(a.2) \beta_n \leftarrow \frac{r_{n+1}^T (r_{n+1} - r_n)}{r_n^T r_n} \quad (\text{Fletcher-Reeves});$$

$$(a.3) \beta_n \leftarrow \frac{r_{n+1}^T (r_{n+1} - r_n)}{p_n^T (r_{n+1} - r_n)} \quad (\text{Hestenes-Stiefel});$$

$$p_{n+1} \leftarrow r_{n+1} + \beta_n p_n ;$$

$$n \leftarrow n + 1 ;$$

end

2.5.2 Gradient Descent (GD)

The gradient descent algorithm [17, 51] is one of the most commonly used and elementary algorithms to find a local minimum of a function. In order to minimize a function, the function $\mathcal{L}(\theta)$ has to be $\mathcal{L} \in C^1(\mathcal{A})$, meaning that \mathcal{L} is at least one time differentiable in \mathcal{A} . In Algorithm 2, we visualize the gradient descent. First, the gradient of \mathcal{L} is computed with the initial guess $\theta^{(0)}$. Then, the negative gradient of \mathcal{L} is applied with a certain step size α . This is done until a certain breaking condition is fulfilled. In this example, we take the relative error breaking condition

$$\left| \frac{\mathcal{L}(\theta^{(0)}) - \mathcal{L}(\theta^{(n)})}{\mathcal{L}(\theta^{(0)})} \right| > (1 - \varepsilon), \quad (2.12)$$

where $\theta^{(0)}$ is the initial guess of θ and $\theta^{(n)}$ is its value after n updates, with $0 < \varepsilon < 1$. The algorithm is terminated when Equation 2.12 is fulfilled. We note that for a big step size α , the algorithm may not converge, and that for a small step size α , it might take a long time to converge (assuming there exists a minimum). We note that choosing a fixed step-size of α can either lead to very slow convergence or to oscillation around a minimum, as can be seen in Figure 2.4 and Figure 2.5. To avoid such behavior, we can implement the Armijo–Goldstein condition [3], as described in the Subsection 2.5.3.

Algorithm 2: A visualization of the gradient descent algorithm. We note that α can be updated after each iteration, with, e.g., the Armijo–Goldstein condition described in Subsection 2.5.3 and Algorithm 3.

Data: $\alpha > 0$ step size; ε breaking condition
Result: $\arg \min_{\theta} \mathcal{L}(\theta)$
 $\theta^{(0)}$ initial guess ;
 $n \leftarrow 0$;
while $\left| \frac{\mathcal{L}(\theta^{(0)}) - \mathcal{L}(\theta^{(n)})}{\mathcal{L}(\theta^{(0)})} \right| < (1 - \varepsilon)$ **do**
 $n \leftarrow n + 1$;
 $p \leftarrow -\nabla \mathcal{L}(\theta^{(n-1)})$ set gradient as search direction;
 $\theta^{(n)} \leftarrow \theta^{(n-1)} + \alpha p$ apply search direction;
end

2.5.3 Armijo–Goldstein condition

A constant step size can lead to very slow optimization, or even to the optimization algorithm oscillating around a minimum. Therefore, it is important to update the step size during the optimization. One well-known method is the Armijo–Goldstein condition [3], which can be applied if the function being minimized is $\mathcal{L}(\theta) \in C^1(\mathcal{A})$. We show this method in Algorithm 3.

Algorithm 3: The Armijo–Goldstein condition to reduce the step size during the optimization process. In our examples we use $\alpha = 1$, $\sigma = \delta = 0.1$.

Data: α step size, search control parameters $0 < \sigma < 1$ and $0 < \delta < 1$, p search direction

Result: α new step size

```

while  $\mathcal{L}(\theta + \alpha p) > \mathcal{L}(\theta) + \alpha \delta \nabla \mathcal{L}(\theta)^T p$  do
  |  $\alpha \leftarrow \sigma \alpha$  reduce step size;
end

```

2.5.4 Gauss–Newton (GN) and Conjugate quasi-Newton (CqN) algorithm

Algorithm 4: A visualization of the gradient GN and the CqN algorithm. Either use (a.1) or (a.2): (a.1) is the standard approximation (a.2) can have the advantage of additional regularization and ensures that H is positive definite, which can be important for the CG algorithm. Solving $Hp = -\nabla \mathcal{L}(\theta^{(n)})$ with (b.1) is the GN method, (b.2) is the CqN method, which solves it with maximal c iteration (e.g., $c = 2$). We note, that α can be updated with e.g. the Armijo–Goldstein condition described in Subsection 2.5.3 and Algorithm 3.

Data: ε breaking condition

Result: $\arg \min_{\theta} \mathcal{L}(\theta)$

$\theta^{(0)}$ initial guess ;

$n \leftarrow 0$;

```

while  $\left| \frac{\mathcal{L}(\theta^{(0)}) - \mathcal{L}(\theta^{(n)})}{\mathcal{L}(\theta^{(0)})} \right| < (1 - \varepsilon)$  do

```

```

  |  $n \leftarrow n + 1$  ;

```

```

  |  $J \leftarrow \nabla G(t^{obs}, \theta^{(n-1)})$  calculate Jacobian matrix ;

```

```

  | approximate the Hessian Matrix  $H$ ;

```

```

  | (a.1)  $H \leftarrow J^T J$  ;

```

```

  | (a.2)  $H \leftarrow J^T J + \lambda E$  ;

```

```

  | solve  $Hp = -\nabla \mathcal{L}(\theta^{(n)})$  ;

```

```

  | (b.1) standard (GN);

```

```

  | (b.2) maximal  $c$  iterations using CG (CqN) ;

```

```

  | adapt step size  $\alpha$  with Armijo–Goldstein condition;

```

```

  |  $\theta^{(n)} \leftarrow \theta^{(n-1)} + \alpha p$  ;

```

```

end

```

In contrast to the GD, the GN Algorithm [29, 30, 90] can be more robust and faster in the optimization. The GN algorithm locally converges quadratically when we minimize the MSE_{Loss}.

We apply the **GN** algorithm on the **MSELoss** in Equation 2.10. For simplification, we write

$$\mathcal{L}(\theta) = \frac{1}{2} \left\| G(t^{obs}, \theta) - Y^{obs} \right\|_2^2 = \frac{1}{2} \|d(\theta)\|_2^2 = \frac{1}{2} \sum_{n=1}^N (d_n(\theta))^2, \quad (2.13)$$

with the residual vector

$$d(\theta) = \begin{bmatrix} d_1(\theta) \\ \vdots \\ d_N(\theta) \end{bmatrix} = \begin{bmatrix} g(t_1^{obs}, \theta) - y_1^{obs} \\ \vdots \\ g(t_N^{obs}, \theta) - y_N^{obs} \end{bmatrix}.$$

The second order of the Taylor-Approximation of $\mathcal{L}(\theta)$ is

$$\mathcal{L}(\theta) \approx \mathcal{L}(\hat{\theta}) + \nabla \mathcal{L}(\hat{\theta})^T (\theta - \hat{\theta}) + (\theta - \hat{\theta})^T \nabla^2 \mathcal{L}(\hat{\theta}) (\theta - \hat{\theta})$$

and is a polynomial approximation of the order two of the function $\mathcal{L}(\theta)$ evaluated at $\hat{\theta} \in \mathbb{R}^M$ that is close enough to θ . To find the minimum of $\mathcal{L}(\theta)$, we need to search for a θ s.t. $\nabla \mathcal{L}(\theta) = 0$. Hence, using

$$\nabla \mathcal{L}(\theta) \approx \nabla \mathcal{L}(\hat{\theta}) + \underbrace{\nabla^2 \mathcal{L}(\hat{\theta})}_{=p} (\theta - \hat{\theta})$$

we get that

$$-\nabla \mathcal{L}(\hat{\theta}) \approx \nabla^2 \mathcal{L}(\hat{\theta}) p. \quad (2.14)$$

Solving Equation 2.14 and updating θ iteratively gives us the Newton-Method [90]. However, the Hessian matrix $\nabla^2 \mathcal{L}(\theta)$ can be very cumbersome to calculate and expensive to compute. The **GN** method approximates the Hessian matrix $\nabla^2 \mathcal{L}(\theta)$ with the Jacobian matrix of $G(t^{obs}, \theta)$

$$J_G(\theta) = \begin{bmatrix} \nabla d_1(\theta)^T \\ \vdots \\ \nabla d_N(\theta)^T \end{bmatrix} = \begin{bmatrix} \frac{\partial g(t_1^{obs}, \theta)}{\partial \theta_1} & \dots & \frac{\partial g(t_1^{obs}, \theta)}{\partial \theta_M} \\ \vdots & \ddots & \vdots \\ \frac{\partial g(t_N^{obs}, \theta)}{\partial \theta_1} & \dots & \frac{\partial g(t_N^{obs}, \theta)}{\partial \theta_M} \end{bmatrix}$$

as follows

$$\nabla^2 \mathcal{L}(\theta) \approx J_G(\theta)^T J_G(\theta). \quad (2.15)$$

The Hessian matrix can be approximated in that way because the gradient of Equation 2.13 is

$$\nabla \mathcal{L}(\theta) = \sum_{n=1}^N d_n(\theta) \nabla d_n(\theta) = J_G(\theta)^T d(\theta) = J_G(\theta)^T \left(G(t^{obs}, \theta) - Y^{obs} \right), \quad (2.16)$$

and therefore, the Hessian matrix is

$$\begin{aligned} \nabla^2 \mathcal{L}(\theta) &= \sum_{n=1}^N \nabla d_n(\theta) \nabla d_n(\theta)^T + \sum_{n=1}^N d_n(\theta) \nabla^2 d_n(\theta) \\ &= J_G(\theta)^T J_G(\theta) + \sum_{n=1}^N d_n(\theta) \nabla^2 d_n(\theta) \end{aligned} \quad (2.17)$$

In most cases, the first term of Equation 2.17 dominates the second part (for θ close enough to the minimum of $\mathcal{L}(\theta)$); hence, the convergence is similar to Newton's method. The first term is dominant if the $|d_n(\theta)|$ or $|\nabla^2 d_n(\theta)|$ terms are significantly smaller than the eigenvalues of $J_G(\theta)^T J_G(\theta)$. This happens either if the residuals $d_n(\theta)$ are small, or if the residuals $d_n(\theta)$ are nearly affine, hence $|\nabla^2 d_n(\theta)|$ are small. This leads to a rapid local convergence of the GN algorithm [90].

We note that according to Levenberg-Marquardt [90], the GN method finds a solution with

$$(J_G(\theta)^T J_G(\theta) + \lambda E)p = -\nabla \mathcal{L}(\theta_n) \quad (2.18)$$

for an appropriate λ and the unity matrix E .

In Algorithm 4, the GN algorithm is explained. First, an initial guess $\theta^{(0)}$ is defined. Then, while the breaking condition is not fulfilled: First, the Jacobian matrix is computed, second the Hessian matrix H is approximated either with Equation 2.15 or Equation 2.18, and third, the equation

$$Hp = -\nabla \mathcal{L}(\theta^{(n)}) \quad (2.19)$$

is solved. Solving Equation 2.19 with the CG method using a maximal number of c iterations (e.g. $c = 2$), is called the CqN algorithm. For large-scale matrices, the advantage of solving Equation 2.19 with CqN is that it speeds up the algorithm (reducing the computational cost when solving the inverse problem) and still gives a good approximation.

2.5.5 Examples

This subsection will show examples of how to solve a *linear* and a *non-linear* model.

Linear Model

Here, we will give a simple example of how to solve a linear model and explain how to transform the function

$$l(t, \theta) = -t^2 + \theta_1 t + \theta_2, \quad (2.20)$$

with the experimental condition t and the unknown condition θ , into a linear model. First, we bring all the unknowns θ onto one side and all the parameters independent of θ onto the other side

$$g(t, \theta) = l(t, \theta) + t^2 = \theta_1 t + \theta_2. \quad (2.21)$$

We can deduce from the right side of Equation 2.21 and Equation 2.6, that

$$y^{obs} \approx f(t^{obs})^T \theta = \begin{bmatrix} t^{obs} \\ 1 \end{bmatrix}^T \begin{bmatrix} \theta_1 \\ \theta_2 \end{bmatrix}. \quad (2.22)$$

We assume, that we have N measurements, and hence, with the help of Equation 2.7, Equation 2.8, and Equation 2.21 we get

$$F \left(t^{obs} \right) = \begin{bmatrix} t_1^{obs} & \dots & t_N^{obs} \\ 1 & \dots & 1 \end{bmatrix}.$$

We note that in [72] some methods are described to solve linear equations, but in this thesis, we focus solely on the CG Algorithm [34], which is described in more detail in Section 2.5.1. In our example, the equation can easily be solved analytically. The CG method is generally used to solve large linear systems.

We assume, that we have N independent measurements, and $l(t, \theta)$ has an error distribution of $\mathcal{N}(0, 1)$. Further, we assume that the ground truth is $\theta = [\theta_1, \theta_2]^T = [3, 10]^T$, as shown in Table 2.2. We would like to find θ using y^{obs} from Table 2.2 with N observations.

t^{obs}	-5	-3	-1	1	3	5
$l(t^{obs}, \theta)$	-30	-8	6	12	10	0
$l(t^{obs}, \theta) + \varepsilon$	-29.4623	-6.1661	3.7412	12.8622	10.3188	-1.3077
$y^{obs} = g(t^{obs}, \theta) + \varepsilon$	-4.4623	2.8339	4.7412	13.8622	19.3188	23.6923

Table 2.2: We assume that we have N measurements of $l(t^{obs}, \theta)$ where ε is drawn from a $\mathcal{N}(0, 1)$ distribution.

Case 1, $N = 2$

In the first case $N = 2$, with the known experimental condition $t^{obs} = [-5, -3]$, we have

$$Y^{obs} = \begin{bmatrix} -4.4623 \\ 2.8339 \end{bmatrix} = \begin{bmatrix} -5 & -3 \\ 1 & 1 \end{bmatrix}^T \begin{bmatrix} \theta_1 \\ \theta_2 \end{bmatrix} = F(t^{obs})^T \theta$$

a linear system with two equations and two unknowns can be solved analytically, and we thus get

$$\begin{bmatrix} \theta_1 \\ \theta_2 \end{bmatrix} = \begin{bmatrix} 3.6481 \\ 10.4009 \end{bmatrix}$$

as shown in Figure 2.3. We note that it has an error of $\|\theta^{true} - \theta\|_2 = 0.7621$.

Case 2, $N > 2$

Now we assume that we have more measurements than unknowns, e.g., $N = 6$. To be more precise, we assume that we have measurements at $t^{obs} = [-5, -3, -1, 1, 3, 5]$, see Table 2.2. Hence, we have

$$Y^{obs} = \begin{bmatrix} -4.4623 \\ 2.8339 \\ 4.7412 \\ 13.8622 \\ 19.3188 \\ 23.6923 \end{bmatrix} = \begin{bmatrix} -5 & 1 \\ -3 & 1 \\ -1 & 1 \\ 1 & 1 \\ 3 & 1 \\ 5 & 1 \end{bmatrix} \begin{bmatrix} \theta_1 \\ \theta_2 \end{bmatrix} = F(t^{obs})^T \theta.$$

As we can see, we have more equations than unknowns. We cannot get an analytical solution assuming all the equations are linearly independent. However, there exists a simple trick to

t^{obs}	-5	-3	-1	1	3	5
$g(t^{obs}, \theta)$	-30	-8	6	12	10	0
$g(t^{obs}, \theta) + \varepsilon$	-29.4623	-6.1661	3.7412	12.8622	10.3188	-1.3077

Table 2.3: We assume that we have N measurements of $g(t^{obs}, \theta)$ where ε is drawn from a $\mathcal{N}(0, 1)$ distribution.

get the same amount of equations and unknown parameters, namely multiplying both sides by $F(t^{obs})$,

$$F(t^{obs})Y^{obs} = \begin{bmatrix} 199.3489 \\ 59.9860 \end{bmatrix} = \begin{bmatrix} 70 & 0 \\ 0 & 6 \end{bmatrix} \begin{bmatrix} \theta_1 \\ \theta_2 \end{bmatrix} = F(t^{obs})F(t^{obs})^T \theta.$$

Now, we have only two linear equations with two unknowns, and they can be easily solved. We get a very good approximation of

$$\begin{bmatrix} \theta_1 \\ \theta_2 \end{bmatrix} = \begin{bmatrix} 2.8478 \\ 9.9977 \end{bmatrix},$$

as shown in Figure 2.3. It has an error of $\|\theta^{true} - \theta\|_2 = 0.1522$.

We note that for a large-scale linear problem (a lot of unknowns), the **CG** method described in Subsection 2.5.1 is a good and inexpensive approximator since only matrix-vector multiplications are needed.

Case 3, $N < 2$

Assuming now that we have fewer equations than unknowns, e.g., $N = 1$, with $t^{obs} = -1$, hence, we have

$$Y^{obs} = [4.7412] = \begin{bmatrix} -1 \\ 1 \end{bmatrix}^T \begin{bmatrix} \theta_1 \\ \theta_2 \end{bmatrix} = F(t^{obs})^T \theta.$$

We have one equation with two unknowns; therefore, we have infinitely many solutions. Two of them are

$$\begin{bmatrix} \theta_1 \\ \theta_2 \end{bmatrix} = \begin{bmatrix} -4.7412 \\ 0 \end{bmatrix} \quad \text{and} \quad \begin{bmatrix} \theta_1 \\ \theta_2 \end{bmatrix} = \begin{bmatrix} -2.3706 \\ 2.3706 \end{bmatrix},$$

as shown in Figure 2.3. In such a case, additional boundary conditions can improve the results.

Non-linear Model

We give an easy example of a non-linear function $f : \mathbb{R} \rightarrow \mathbb{R}$

$$g(t, \theta) = (\theta_1 - t)(\theta_2 + t) \quad \text{with} \quad \begin{bmatrix} \theta_1 \\ \theta_2 \end{bmatrix} = \begin{bmatrix} 5 \\ 2 \end{bmatrix}.$$

In fact, it is the same function as $l(t, \theta)$ in Equation 2.20 as visualized in Figure 2.3. We will use the same values as in Table 2.2, and display the values of the function $g(t^{obs}, \theta)$ in Table 2.3. We

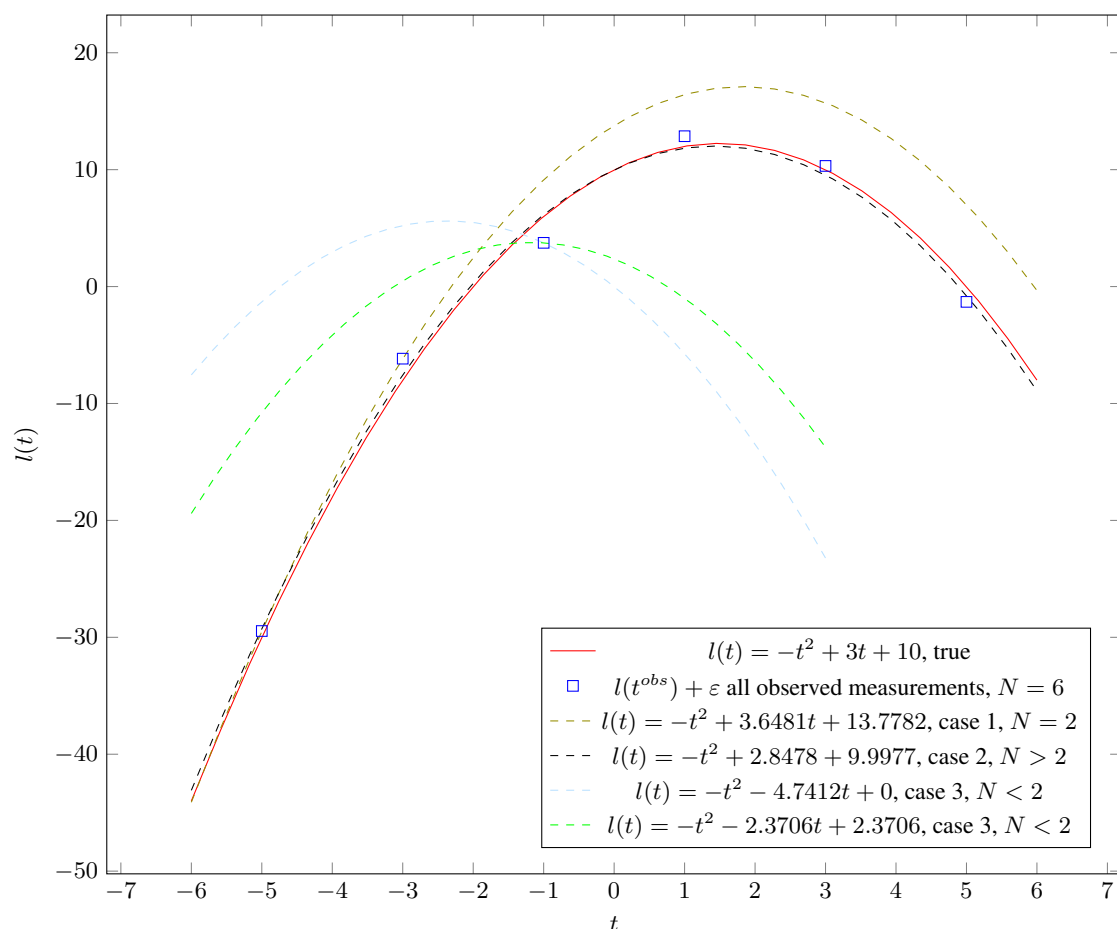


Figure 2.3: A visualization of the function $l(t, \theta)$ of Equation 2.20, and the resulting reconstruction of the model, assuming that θ is unknown, and only N measurements at the points of Table 2.2 are known.

define the gradient $\nabla \mathcal{L}(\theta)$ and the Hessian matrix $\nabla^2 \mathcal{L}(\theta)$ as follows

$$\nabla \mathcal{L}(\theta) = \begin{bmatrix} \frac{\partial \mathcal{L}(\theta)}{\partial \theta_1} \\ \vdots \\ \frac{\partial \mathcal{L}(\theta)}{\partial \theta_k} \end{bmatrix} \quad \text{and} \quad \nabla^2 \mathcal{L}(\theta) = \begin{bmatrix} \frac{\partial^2 \mathcal{L}(\theta)}{\partial \theta_1 \partial \theta_1} & \cdots & \frac{\partial^2 \mathcal{L}(\theta)}{\partial \theta_k \partial \theta_1} \\ \vdots & \ddots & \vdots \\ \frac{\partial^2 \mathcal{L}(\theta)}{\partial \theta_1 \partial \theta_k} & \cdots & \frac{\partial^2 \mathcal{L}(\theta)}{\partial \theta_k \partial \theta_k} \end{bmatrix}.$$

We minimize the function $\mathcal{L}(\theta)$ in Equation 2.10 using the GD, GN, and CqN (see Subsection 2.5.2 and Subsection 2.5.4). For these optimizations, we need to calculate the gradient $\nabla \mathcal{L}(\theta)$ and approximate the Hessian matrix $\nabla^2 \mathcal{L}(\theta)$. Because of Equation 2.16 and Equation 2.15, it is sufficient to calculate the Jacobian matrix $J_G(\theta)$ of $G(t^{obs}, \theta)$. Hence using

Equation 2.16, we calculate

$$J_G(\theta) = \begin{bmatrix} \theta_2 + t_1^{obs} & \theta_1 - t_1^{obs} \\ \vdots & \vdots \\ \theta_2 + t_N^{obs} & \theta_1 - t_N^{obs} \end{bmatrix}$$

and therefore get

$$\nabla \mathcal{L}(\theta) = J_G(\theta)^T \left(G(t^{obs}, \theta) - Y^{obs} \right). \quad (2.23)$$

Then with Equation 2.15 the approximation for the Hessian matrix of $\mathcal{L}(\theta)$ is

$$\nabla^2 \mathcal{L}(\theta) \approx J_G(\theta)^T J_G(\theta).$$

The resulting θ from all the algorithms are similar. In Figure 2.4 we show the value of the **MSELoss** $\mathcal{L}(\theta)$ after each iteration, and in Figure 2.5 we show the development of θ_1 and θ_2 after each iteration with the initial guess of $\theta = [0, 0]^T$. We note that it is essential that the **GD** have a good step size. Otherwise, it may converge very slowly or not at all. Therefore, using the Armijo-Goldstein condition can drastically improve the performance of the **GD**. In general, finding the step size with the Armijo-Goldstein condition improves the number of iterations needed to find a good approximation of θ .

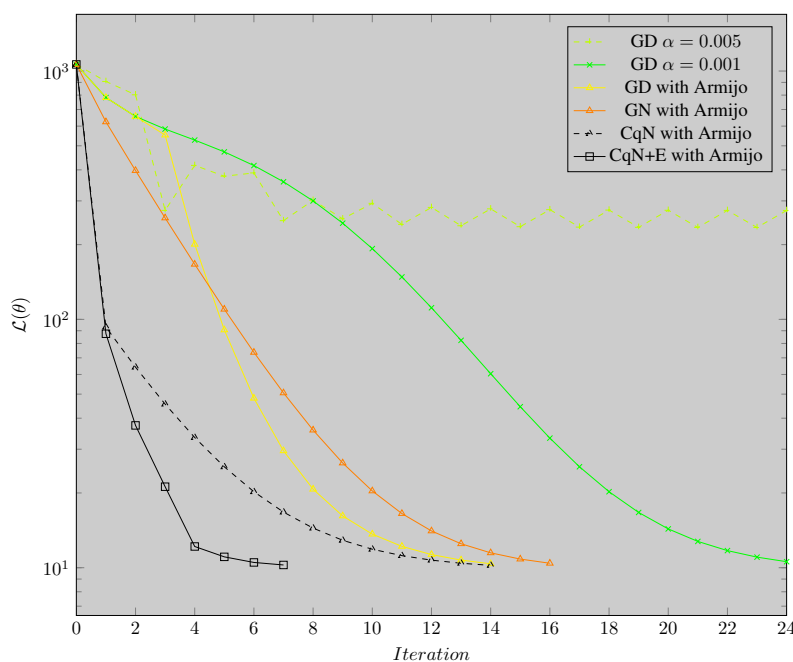


Figure 2.4: Comparing the $\mathcal{L}(\theta)$ value of Equation 2.10 using **GD** with step size $\alpha = 0.005$, $\alpha = 0.001$, and Armijo-Goldstein condition. In addition, we solve the minimization problem with **GN**, **CqN**, and add the unity matrix to the Hessian approximation (**CqN+E**).

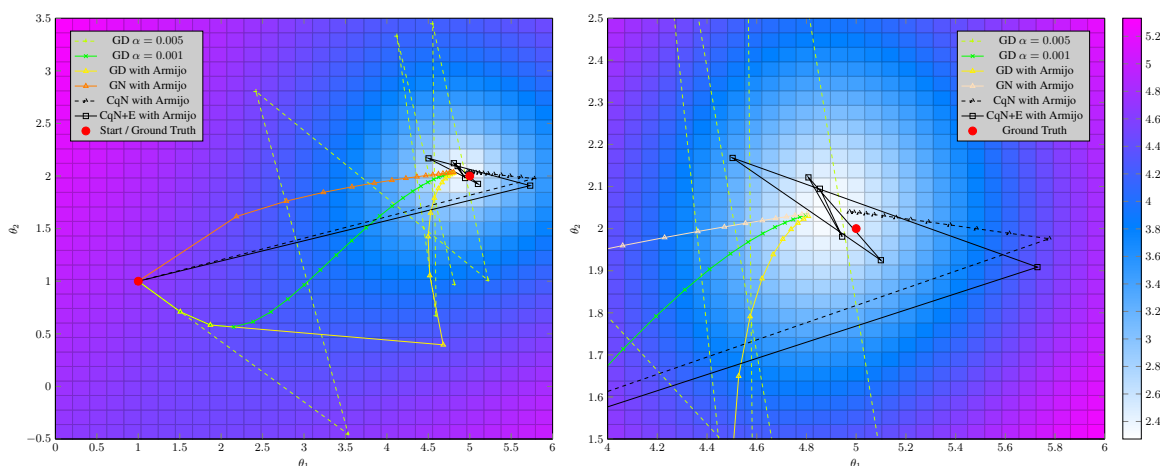


Figure 2.5: The background of the figure shows the value (colorbar) of the loss function $\mathcal{L}(\theta)$. The lines visualize the minimization process of $\mathcal{L}(\theta)$ of Equation 2.10 resulting θ_1 and θ_2 after each iteration with GD using the step size $\alpha = 0.005$, $\alpha = 0.001$, and Armijo-Goldstein condition. In addition, the GN, CqN, and adding the unity matrix to the Hessian approximation using CqN (CqN+E) are shown. On the left, we see the optimization process from the start to end, and on the right just a limited area of the optimization process towards the end. The initial guess is $\theta^{(0)} = (1, 1)$ and the ground truth is $\theta = (5, 2)$.

2.6 Partial Differential Equation (PDE)

Sine, cosine, and ln are at a party. Sine approaches cosine and says, “Hey, what’s ln doing over in the corner by herself?”. Cosine responds, “You see, ln doesn’t integrate very well.”.

– unknown

A PDE is a relation between a multi-variable function with various partial derivatives [88]. These are not only used in the pure mathematical field but also in fields like physics and engineering. In this thesis, we use PDEs for a more fundamental understanding of the propagation of the acoustic waves in the tissues. With the help of the PDE of the wave equation, we aim to reconstruct the structure and the medium velocity of different tissues. This section uses [63] as a basis to explain the transformation of the PDE from the wave equation to the Helmholtz equation and the description of FD and FE. The PDE of the wave equation is

$$-\nabla \cdot (u(x)\nabla \bar{y}(x, t)) + \bar{y}_{tt}(x, t) = \bar{f}(x, t), \quad (2.24)$$

where $u(x) > 0$ is the squared medium velocity, $\bar{f}(x, t)$ the source function and $\bar{y}(x, t)$ the pressure variation. We note, that $x \in \mathbb{R}^n$ is the n dimensional space domain and $t \in \mathbb{R}_{\geq 0}$ the time domain. From this PDE, the Helmholtz equation can be derived. A time-harmonic wave can express the source and the wave field; hence, we can use the Fourier transform of the time variable and separate time and space dimensions to write \bar{f} and \bar{y} as:

$$\bar{y}(x, t) = y(x)e^{-i\omega t} \quad \text{and} \quad \bar{f}(x, t) = f(x)e^{-i\omega t}, \quad (2.25)$$

where ω is the angular frequency, $f(x)$ the source function and $y(x)$ the pressure variation. By substituting Equation 2.25 into the wave Equation 2.24, we get the frequency dependent form of the wave equation; namely, the Helmholtz equation

$$-\nabla \cdot (u(x)\nabla y(x)) - \omega^2 y(x) = f(x).$$

In our approach, we use the Sommerfeld boundary condition, which is an absorbing boundary condition [10, 11, 21]

$$\begin{cases} -\nabla \cdot (u(x)\nabla y(x)) - \omega^2 y(x) = f(x), & \text{in } \Omega^\circ = \Omega \setminus \partial\Omega \\ \frac{\partial y(x)}{\partial \mathbf{n}} - ik(x)y(x) = 0, & \text{on } \Gamma = \partial\Omega \end{cases}, \quad (2.26)$$

where $k(x) = \frac{\omega}{\sqrt{u(x)}}$ is the wave-number at time-frequency ω and

$$\frac{\partial y(x)}{\partial \mathbf{n}} := \mathbf{n} \cdot \nabla y(x)$$

is the normal derivative, where \mathbf{n} denotes the normal on the boundary $\Gamma = \partial\Omega$.

It is generally challenging to solve a PDE analytically, and sometimes an analytical solution does not even exist. Therefore, we solve it numerically by discretizing the PDE using either FD or FE [63].

2.6.1 Finite Difference (FD)

The FD grid is a uniformly staggered mesh, as visualized in Figure 2.6. The PDE is solved numerically on the grid points. We will explain how to solve the Helmholtz Equation 2.26 using FD in a 2D space. It can be generalized to higher dimensions as well. First, we separate the functions $y = y(x)$ and $f = f(x)$ into the real (r) and imaginary (i) parts,

$$y = y^{(r)} + iy^{(i)}, \quad f = f^{(r)} + if^{(i)},$$

therefore obtaining a double real-valued system instead of a singly complex-valued system. Since the real part, $y^{(r)}$ and the imaginary part $y^{(i)}$ are only coupled on the boundary Γ ; they can be computed separately on Ω° . Hence, the discretized real part of the Equation 2.26 at the grid point (i, j) can be written as

$$-\frac{\partial}{\partial x^{(1)}} \left(u_{i+\frac{1}{2},j} \frac{y_{i+1,j}^{(r)} - y_{i,j}^{(r)}}{h} \right) - \frac{\partial}{\partial x^{(2)}} \left(u_{i,j+\frac{1}{2}} \frac{y_{i,j+1}^{(r)} - y_{i,j}^{(r)}}{h} \right) - \omega^2 y_{i,j}^{(r)} = f_{i,j}^{(r)}, \quad (2.27)$$

where the second order approximation of the first derivative is

$$\frac{\partial}{\partial x^{(1)}} y^{(r)} \Big|_{x=x_{i+\frac{1}{2},j}} = \frac{y_{i+1,j}^{(r)} - y_{i,j}^{(r)}}{h} \quad \text{and} \quad \frac{\partial}{\partial x^{(2)}} y^{(r)} \Big|_{x=x_{i,j+\frac{1}{2}}} = \frac{y_{i,j+1}^{(r)} - y_{i,j}^{(r)}}{h}.$$

We note that

$$\frac{\partial}{\partial x^{(i)}} \left(u(x) \frac{\partial y(x)}{\partial x^{(i)}} \right) = \frac{\partial}{\partial x^{(i)}} u(x) \frac{\partial}{\partial x^{(i)}} y(x) + u(x) \frac{\partial^2}{\partial x^{(i)2}} y(x).$$

Further, we assume that $u(x)$ is a piecewise constant function in the area

$$\begin{aligned} x_{i,j}^{(1)} < x^{(1)} < x_{i+1,j}^{(1)} \\ x_{i,j}^{(2)} < x^{(2)} < x_{i,j+1}^{(2)} \end{aligned} \quad \text{for all } i \text{ and } j,$$

hence,

$$\frac{\partial}{\partial x^{(i)}} u(x) = 0 \quad \text{for all } \begin{aligned} &x_{i,j} < x^{(1)} < x_{i+1,j}^{(1)} \\ &x_{i,j} < x^{(2)} < x_{i,j+1}^{(2)} \end{aligned}.$$

We discretize Equation 2.27 to

$$\begin{aligned} & - \left(u_{i+\frac{1}{2},j} \frac{y_{i+1,j}^{(r)} - y_{i,j}^{(r)}}{h^2} - u_{i-\frac{1}{2},j} \frac{y_{i,j}^{(r)} - y_{i-1,j}^{(r)}}{h^2} \right) \\ & - \left(u_{i,j+\frac{1}{2}} \frac{y_{i,j+1}^{(r)} - y_{i,j}^{(r)}}{h^2} - u_{i,j-\frac{1}{2}} \frac{y_{i,j}^{(r)} - y_{i,j-1}^{(r)}}{h^2} \right) - \omega^2 y_{i,j}^{(r)} = f_{i,j}^{(r)} \end{aligned}$$

or

$$\begin{aligned} & - \frac{1}{h^2} \left[u_{i+\frac{1}{2},j} y_{i+1,j}^{(r)} + u_{i-\frac{1}{2},j} y_{i-1,j}^{(r)} + u_{i,j+\frac{1}{2}} y_{i,j+1}^{(r)} + u_{i,j-\frac{1}{2}} y_{i,j-1}^{(r)} \right] \\ & + \frac{1}{h^2} \left[u_{i+\frac{1}{2},j} + u_{i-\frac{1}{2},j} + u_{i,j+\frac{1}{2}} + u_{i,j-\frac{1}{2}} \right] y_{i,j}^{(r)} - \omega^2 y_{i,j}^{(r)} = f_{i,j}^{(r)}. \end{aligned}$$

The system for the imaginary part $y^{(i)}$ is similarly determined. In the final step, we look at the Sommerfeld boundary condition using the second order of FD. The boundary condition is

$$\frac{\partial y(x)}{\partial \mathbf{n}} - ik(x)y(x) = 0 \quad \text{on } \Gamma,$$

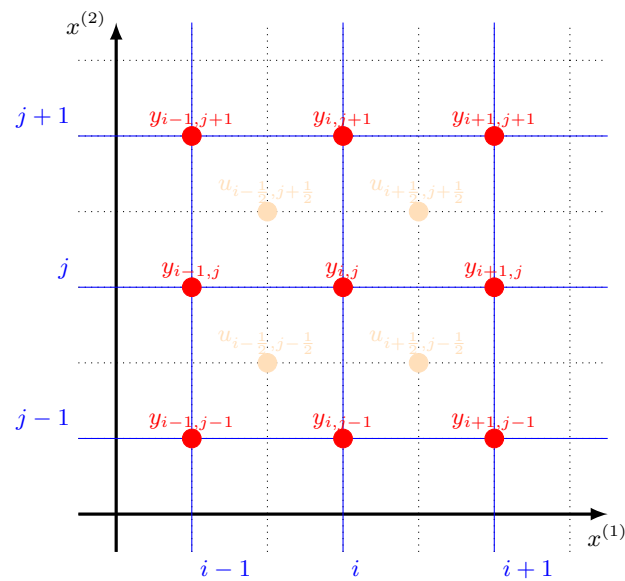
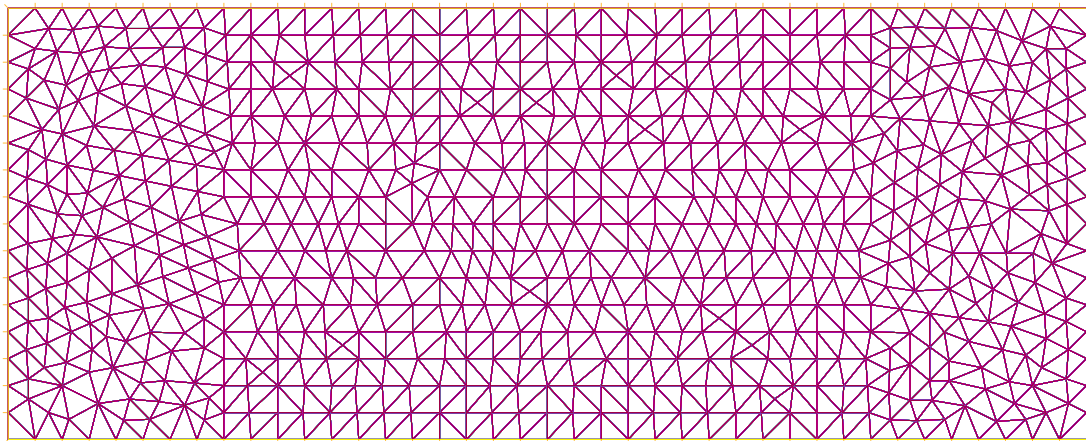
and is discretized on the upper boundary of Γ by

$$\frac{y_{N+1,j} - y_{N,j}}{h} - i \frac{\omega}{\sqrt{u_{N+\frac{1}{2},j}}} y_{N,j} = 0 \quad \text{on } \Gamma.$$

Now, by separating the real and the imaginary part of y on the boundary, we get

$$\begin{cases} y_{N+1,j}^{(r)} = y_{N,j}^{(r)} - \frac{\omega h}{\sqrt{u_{N+\frac{1}{2},j}}} y_{N,j}^{(i)} \\ y_{N+1,j}^{(i)} = y_{N,j}^{(i)} + \frac{\omega h}{\sqrt{u_{N+\frac{1}{2},j}}} y_{N,j}^{(r)} \end{cases} \quad \text{on } \Gamma$$

The other boundaries are similarly calculated.

Figure 2.6: Visualization of a staggered grid used in the **FD** method.Figure 2.7: Visualization of a 2D **FE** mesh using triangle.

2.6.2 Finite Elements (**FE**)

One of the main advantages of **FE** compared to the **FD** method is that the mesh is more flexible. Hence, for complex geometries and mesh adaptation, **FE** is recommended [40]. To solve **PDEs** with the help of the **FE** method, a subspace has to be divided into smaller subparts called finite elements. The finite elements are triangular or quadrilateral in a 2D subspace, see Figure 2.7 as an example. The **PDE** is solved with an equivalent variations formulation of the problem. This allows a formulation of a piecewise polynomial function in each **FE** represented in a large linear system. To do so, we use the weak form. As described in [83], the weak form is the observation

that two finite-dimensional vectors $u, v \in \mathbb{R}^d$ are equal, if and only if their inner product with any vector $\varphi \in \mathbb{R}^d$ are equal:

$$u = v \in \mathbb{R}^d \iff \forall \varphi \in \mathbb{R}^d, u \cdot \varphi = v \cdot \varphi. \quad (2.28)$$

To find the semi-discrete problem of the PDE in Equation 2.28, we multiply it by the complex conjugate \bar{v} of a test function $v \in H^1(\Omega)$. Then, we integrate it over Ω and get the following variational formulation: We search for the unique solution $y \in H^1(\Omega)$ [23, 61] where

$$a(y, v) - \omega^2(y, v)_{L^2} - i\omega b(y, v) = (f, v)_{L^2}, \quad \forall v \in H^1(\Omega)$$

where $(\cdot, \cdot)_{L^2}$ is the $L^2(\Omega)$ hermitian product, and the sesquilinear forms are given by

$$a(y, v) = \int_{\Omega} u(x) \nabla y(x) \nabla \bar{v}(x) dx$$

and

$$b(y, v) = \int_{\Gamma} \sqrt{u(x)} y(x) \bar{v}(x) dx.$$

We now look at a finite element of our mesh; in other words, we look at a finite dimension subspace $V_h \subset H^1(\Omega)$ of a piecewise polynomial function of degree p . This leads to the semi-discrete Galerkin formulation, where we find $y_h \in V_h$ such that

$$a(y_h, v) - \omega(y_h, v)_{L^2} - i\omega b(y_h, v) = (f, v)_{L^2}, \quad \forall v \in V_h. \quad (2.29)$$

Let $\{\varphi_i\}_{i=1}^N$ denote a nodal Lagrangian basis [89] of V_h . We can then write, for all $v_h \in V_h$,

$$y_h = \sum_{j=1}^N Y_j \varphi_j, \quad \text{with} \quad (\varphi_i, \varphi_j)_{L^2} = \begin{cases} 0 & , \quad i \neq j \\ 1 & , \quad i = j \end{cases}.$$

Hence, the semi-discrete formulation of Equation 2.29 is equivalent to

$$\sum_{j=1}^N Y_i a(\varphi_j, \varphi_i) - \omega^2 \sum_{j=1}^N Y_j (\varphi_j, \varphi_i)_{L^2} - i\omega \sum_{j=1}^N Y_j b(\varphi_j, \varphi_i) = (f, \varphi_i)_{L^2}$$

for all $i = 1, \dots, N$. Finally, we can write it as a matrix-vector multiplication:

$Y = [Y_1, \dots, Y_N]^T \in \mathbb{R}^{N \times 1}$ is the unknown discretized pressure variation, solved by the equation

$$KY - \omega^2 MY - i\omega BY = R,$$

where $R \in \mathbb{R}^{N \times 1}$ and $M, N, B \in \mathbb{R}^{N \times N}$ are given by

$$R_i = (f, \varphi_i)_{L^2}, \quad M_{i,j} = (\varphi_j, \varphi_i)_{L^2}, \quad K_{i,j} = a(\varphi_j, \varphi_i), \quad B_{i,j} = b(\varphi_j, \varphi_i),$$

for $i, j = 1, \dots, N$. We note that the matrices M and K are sparse, symmetric, and positive semi-definite and that the matrix B is sparse, symmetric, and has a low rank.

2.7 Neural Networks (NN)

The world is a very strange place, and the dice are always rolling.
– Tom Robbins

NN [12] are well established in medical imaging [18, 49, 53, 75], speech and signal processing [32, 42, 48, 62]. The fundamental principle of a NN is to interpret an input and compute the desired output. In medical imaging, an input may be a CT data set, and the output will be segmented bones. In speech recognition, an audio recording is used as an input and results in a word classification, respectively word recognition as an output. Another example, discussed in more detail in Chapter 5, predicts the depth of the cut during bone ablation. There the NN uses an acoustic wave emitted during the bone ablation to predict the depth of the cut. In this case, the NN solves the forward problem, which maps the acoustic waves (the subset \mathcal{A}) to the depth of the cut (the subset \mathcal{B}).

The simplest explanation of a NN is that it is a combination of derivable functions f_i that map a set \mathcal{A} onto another set \mathcal{B}

$$f = f_K \circ \dots \circ f_0 : \mathcal{A} \longrightarrow \mathcal{B}.$$

The NN we use is called a feed-forward neural network [2]. This means that the function f maps the set \mathcal{A} directly on the set \mathcal{B} without using any loops or recurrent connections. The functions f_i are usually fully connected layers, convolution layers, Maxpool layers, activation functions, and some normalization. These functions have different weights, and depending on the structure and the weights, the NN will perform better or worse. To get a well-performing network, we need to optimize the weights. Therefore, we first need to solve the following inverse problem: For a given acoustic wave (known initial condition), what are the unknown parameters θ (here, *what are the weights*), so that we can get *the desired depth* (observation). Hence, when we solve the inverse problem, we find the unknown parameters θ ; thus, we find the weights, which we will use to solve the forward problem.

Solving the inverse problem of a NN is referred to as training the network. To train the network, we first need to separate our measured data (initial condition) and its corresponding label (observation). In most cases, the data is divided into three disjoint subsets: Training, validating, and testing data. The training data is used to find the unknown parameters by solving the inverse problem, and the validating data is used to validate the performance of the forward problem of the network. The best-performing parameters on the validation data are then used to test the network's performance on previously unseen data, namely, the testing data. This strategy helps to find suitable parameters and avoids over-optimizing on the training data.

We use a Convolutional Neural Network (CNN), where, first, we have several convolutional layers (see Subsection 2.7.2). A Maxpool layer follows each convolutional layer (see Subsection 2.7.3). After multiple convolutional layers, the output is flattened to a one-dimensional vector. This is then used as input for the fully connected layers. A dropout may be applied onto the fully connected layer (see Subsection 2.7.1). In the final step, the output of the fully connected layer is the desired output. We note that after each layer, a batch normalization can be applied. The loss function is minimized using the optimizer Adam [47]. We will not show

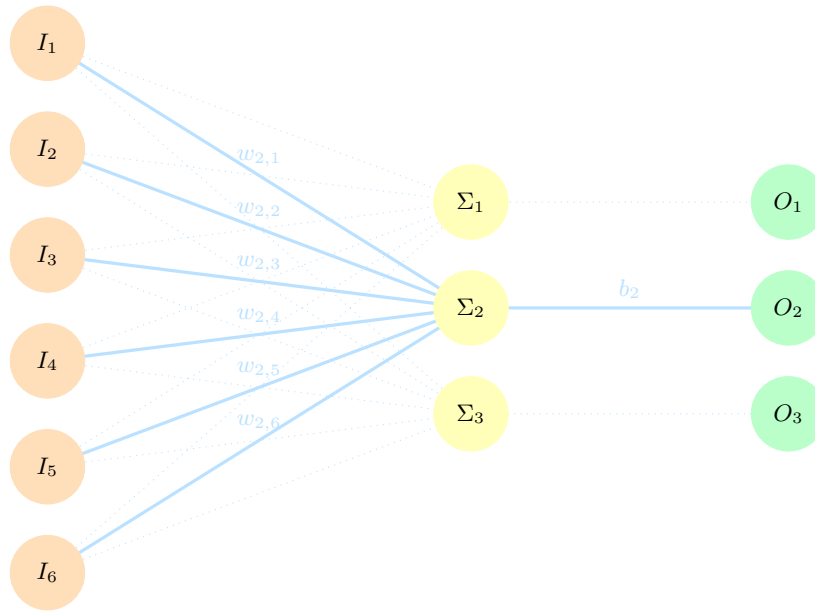


Figure 2.8: Visualization of a fully connected layer. Each element (neuron) of the input layer I is multiplied by the weight $w_{j,i}$. Σ_j represents the sum of the weighted I . Then the bias b is added, and in a final step, the activation function σ is applied to map the input layer I to the output layer O .

how the gradient is calculated because this has been shown in great detail in the thesis of Andermatt [2].

2.7.1 Fully Connected Layers

A fully connected layer can be described as a matrix-vector multiplication. To better visualize the multiplication, we take a look at Figure 2.8. In our example, we have an input vector I of the size $N_I = 6$ and an output vector O of the size $M_O = 3$. Each element of I and O are called neurons. As the word fully connected indicates, each neuron of I is connected with each neuron of O . We describe the mapping of the input layer I to the neuron O_j as follows

$$\sigma([w_{j,1}I_1] + \dots + [w_{j,N_I}I_{N_I}] + b_j) = \sigma\left(\sum_{i=1}^{N_I} [w_{j,i}I_i] + b_j\right) = O_j.$$

In the mapping from I to O_j , each neuron I_i of the input is multiplied by the weight $w_{j,i}$. Then we take the sum over all $i = 1, \dots, N_I$ and add the bias b_j . In the final step, an activation function σ is applied, as described in Subsection 2.7.4. To generalize the mapping between the neurons I and O we write it as a matrix-vector multiplication:

$$\sigma(W \cdot I + b) = \sigma\left(\begin{bmatrix} w_{1,1} & \dots & w_{1,N_I} \\ \vdots & \ddots & \vdots \\ w_{M_O,1} & \dots & w_{M_O,N_I} \end{bmatrix} \cdot \begin{bmatrix} I_1 \\ \vdots \\ I_{N_I} \end{bmatrix} + \begin{bmatrix} b_1 \\ \vdots \\ b_{M_O} \end{bmatrix}\right) = \begin{bmatrix} O_1 \\ \vdots \\ O_{M_O} \end{bmatrix} = O,$$

with the weight matrix $W \in \mathbb{R}^{M_O \times N_I}$, the input vector $I \in \mathbb{R}^{N_I \times 1}$, the bias $b \in \mathbb{R}^{M_O \times 1}$, and the output vector $O \in \mathbb{R}^{M_O \times 1}$. We note that the input and output sizes can be chosen arbitrarily. If multiple fully connected layers follow each other, then the output size of the previous layer has to be the same as the input size of the current layer. The final layer has the same output size as the desired output of the network, or in our case, the dimension of \mathcal{B} . We note that the weights have a linear dependency; hence, the derivative function exists. Therefore, the gradient can be found for each layer and used for the backpropagation. A dropout can be applied on the fully connected layers during the training. A dropout randomly omits weights. This improves the robustness and, therefore, avoids over-optimization of the network.

2.7.2 Convolutional Layers

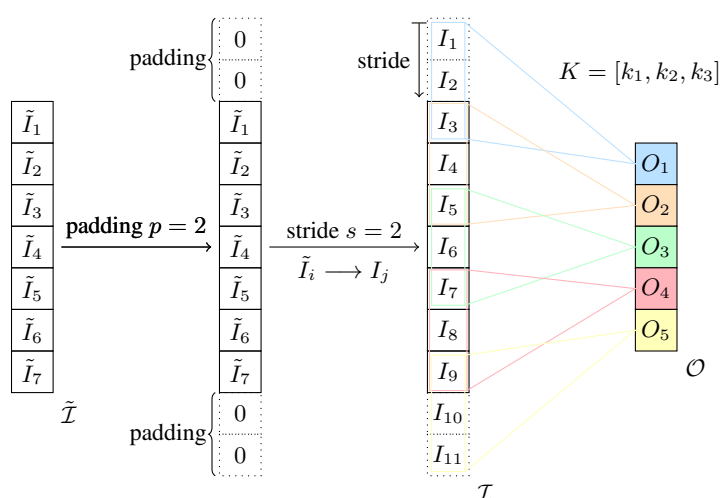


Figure 2.9: A convolution of an array $\tilde{\mathcal{I}} = [\tilde{I}_1, \dots, \tilde{I}_7]$ with a kernel $K = [k_1, k_2, k_3]$, with padding size $p = 2$ (two zeros are added on each boundary which we will refer to as $\mathcal{I} = [I_1, \dots, I_{11}]$), and stride set to $s = 2$ (the kernel K moves two entries, e.g., $O_1 = I_1 \cdot k_1 + I_2 \cdot k_2 + I_3 \cdot k_3$ and $O_2 = I_3 \cdot k_1 + I_4 \cdot k_2 + I_5 \cdot k_3$), leads to an output vector $\mathcal{O} = [O_1, \dots, O_5]$.

Another common layer used for NN are convolutional layers. For simplification, we show the convolution in the 1D case. However, it will work similarly for multidimensional cases. First, we will explain what a convolution is, then how the neural network uses the convolutional layers.

We explain how convolution works with the variables padding p , stride s , and kernel size k . In our example, we set the input array $\tilde{\mathcal{I}}$ to $\tilde{N}_I = 7$. The padding $p = 2$ indicates the number of zeros added to the boundaries, as shown in Figure 2.9. In our case, it will add two zeros on the top and bottom of the array. We define the resulting array of the size $N_I = 11$ as \mathcal{I} . A convolution with the kernel $K = [k_1, k_2, k_3]$, with stride $s = 2$, on the array $\mathcal{I} = [I_1, \dots, I_{N_I}]$

$$\mathcal{I} * K = \mathcal{O},$$

is calculated as follows: The first entry O_1 of the output array $\mathcal{O} = [O_1, \dots, O_{M_O}]$ is

$$O_1 = k_1 I_1 + k_2 I_2 + k_3 I_3,$$

as visualized in Figure 2.9 with the blue triangle. The stride indicates how far the kernel shifts to calculate the next output O_2 , as visualized with the orange triangle. In our case, we have stride $s = 2$; hence, the kernel shifts two indices to calculate the next output. Therefore, we get

$$O_2 = k_1 I_3 + k_2 I_4 + k_3 I_5.$$

We can generalize the equation to calculate the output O_j for an arbitrary kernel size k , and an arbitrary stride size of s

$$O_j = k_1 I_{s(j-1)+1} + k_2 I_{s(j-1)+2} + \dots + k_k I_{s(j-1)+k} = \sum_{i=1}^k k_i I_{s(j-1)+i}.$$

The length M of the output array \mathcal{O} depends on the length \tilde{N}_I of the input array \tilde{I} , the kernel size k , the stride s , and the padding p . It can be calculated with the formula

$$M_O = \left\lfloor \frac{\tilde{N}_I + 2p - k}{s} + 1 \right\rfloor, \quad (2.30)$$

which, in our case, is $M_O = 5$.

The 1D convolutional layer used in PyTorch [71] has some additional properties. In the previous example, the number of input and output channels is one. However, in PyTorch, the number of channels can vary. In Figure 2.10, we give an example of $N_L = 4$ input channels and $M_L = 3$ output channels. For simplification, we use stride $s = 1$ and padding $p = 0$. One of the major differences between single and multiple input and output channels are the number of weights of the kernel. In the previous example, the kernel K had $k = 3$ weights, and only one kernel existed. In Figure 2.10, we see that the kernel K of the size k now has more than k weights. The number of total weights of a kernel is the number of input channels N_L times the size of the kernel; here, it is $N_L \cdot k = 4 \cdot 3 = 12$. In addition, instead of a single kernel, we now have M_L kernels, one for each output channel. Therefore, in our example the output $O_{i,2}$, with $i \in \{1, \dots, M_L\}$ can be formulated as follows

$$\begin{aligned} O_{i,2} &= I_{1,2} k_{1,1}^i + I_{1,3} k_{1,2}^i + I_{1,4} k_{1,3}^i + \dots \\ &\quad \dots + I_{N_L,2} k_{N_L,1}^i + I_{N_L,3} k_{N_L,2}^i + I_{N_L,4} k_{N_L,3}^i \\ &= [I_{1,2} k_{1,1}^i + I_{1,3} k_{1,2}^i + I_{1,4} k_{1,3}^i] + \dots \\ &\quad \dots + [I_{N_L,2} k_{N_L,1}^i + I_{N_L,3} k_{N_L,2}^i + I_{N_L,4} k_{N_L,3}^i] \\ &= \sum_{n=1}^{N_L} [I_{n,2} k_{n,1}^i + I_{n,3} k_{n,2}^i + I_{n,4} k_{n,3}^i] \end{aligned} \quad (2.31)$$

We generalize the equation by assuming that the input has N_L channels, and each channel has the length \tilde{N}_I . Therefore, the input can be represented as a matrix $\tilde{\mathcal{I}} \in \mathbb{R}^{N_L \times \tilde{N}_I}$. The padding size increases each channel's boundary, as visualized in Figure 2.9. Therefore, after padding, we get a matrix of the size $\mathcal{I} \in \mathbb{R}^{N_L \times N_I}$, with $N_I = \tilde{N}_I + 2p$. Since the stride is s and the kernel size is k , we can deduce the length of the output M_O of each layer with the Equation 2.30

$$M_O = \left\lfloor \frac{\tilde{N}_I + 2p - k}{s} + 1 \right\rfloor.$$

When we have M_L output channels, we can represent the output as a matrix $\mathcal{O} \in \mathbb{R}^{M_L \times M_O}$. We note that each output channel \mathcal{O}_i has its own kernel K^i . We generalize Equation 2.31 and write for each entry $O_{i,j}$ in the matrix \mathcal{O} the following

$$\begin{aligned} O_{i,j} &= I_{1,s(j-1)+1}k_{1,1}^i + \cdots + I_{1,s(j-1)+k}k_{1,k}^i + \cdots \\ &\quad \cdots + I_{N_I,s(j-1)+1}k_{N_I,1}^i + \cdots + I_{N_I,s(j-1)+k}k_{N_I,k}^i \\ &= \left[I_{1,s(j-1)+1}k_{1,1}^i + \cdots + I_{1,s(j-1)+k}k_{1,k}^i \right] + \cdots \\ &\quad \cdots + \left[I_{N_I,s(j-1)+1}k_{N_I,1}^i + \cdots + I_{N_I,s(j-1)+k}k_{N_I,k}^i \right] \\ &= \sum_{n=1}^{N_L} \left[I_{n,s(j-1)+1}k_{n,1}^i + \cdots + I_{n,s(j-1)+k}k_{n,k}^i \right] \\ &= \sum_{n=1}^{N_L} \left[\sum_{m=1}^k I_{n,s(j-1)+m}k_{n,m}^i \right] \\ &= \sum_{n=1}^{N_L} \sum_{m=1}^k I_{n,s(j-1)+m}k_{n,m}^i. \end{aligned}$$

Finally, similarly to the previous Subsection 2.7.1, a bias $b_{i,j}$ is added, and a non-linear activation function σ is applied. Hence, we get the final output of the convolutional layer for each entry in $\tilde{\mathcal{O}}$

$$\tilde{O}_{i,j} = \sigma(O_{i,j} + b_{i,j}) = \sigma \left(\sum_{n=1}^{N_L} \sum_{m=1}^k I_{n,s(j-1)+m}k_{n,m}^i + b_{i,j} \right),$$

or simpler

$$\tilde{\mathcal{O}} = \sigma(\mathcal{O} + b),$$

with the final output $\tilde{\mathcal{O}} \in \mathbb{R}^{M_L \times M_O}$ and the bias $b \in \mathbb{R}^{M_L \times M_O}$ having the same dimensions as \mathcal{O} . Again, similarly to the previous Subsection 2.7.1, the parameters which are determined during the training of the network, namely $k_{n,m}^i$ and $b_{i,j}$ are a linear combination, apart from the non-linear activation function. Therefore, the gradient can be computed easily.

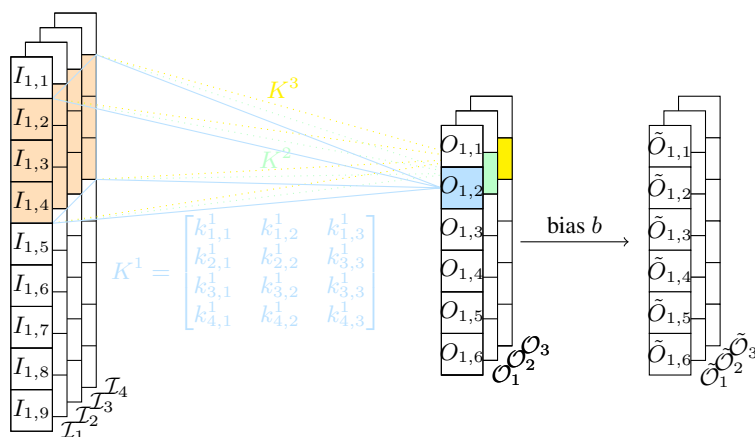


Figure 2.10: An example of a convolution in a NN using $N_L = 4$ channels as input $\mathcal{I} = [\mathcal{I}_1, \dots, \mathcal{I}_{N_L}]$ and $M_L = 3$ channels as output $\mathcal{O} = [\mathcal{O}_1, \dots, \mathcal{O}_{M_L}]$. In this case, we have no padding ($p = 0$), and the stride is set to one ($s = 1$). The kernel of the size $k = 3$ has the dimensions of the input channel; hence, it is of the form $K^i \in \mathbb{R}^{N_L \times k}$ and each output channel has its own kernel, implying, $i = 1, \dots, M_L$. The entry $O_{1,2}$ of the output array is calculated as follows $O_{1,2} = I_{1,2}k_{1,1}^1 + I_{1,3}k_{1,2}^1 + I_{1,4}k_{1,3}^1 + \dots + I_{4,2}k_{4,1}^1 + I_{4,3}k_{4,2}^1 + I_{4,4}k_{4,3}^1$. A bias b is added, and an activation function is applied to get the output $\tilde{\mathcal{O}}$ of the convolutional layer.

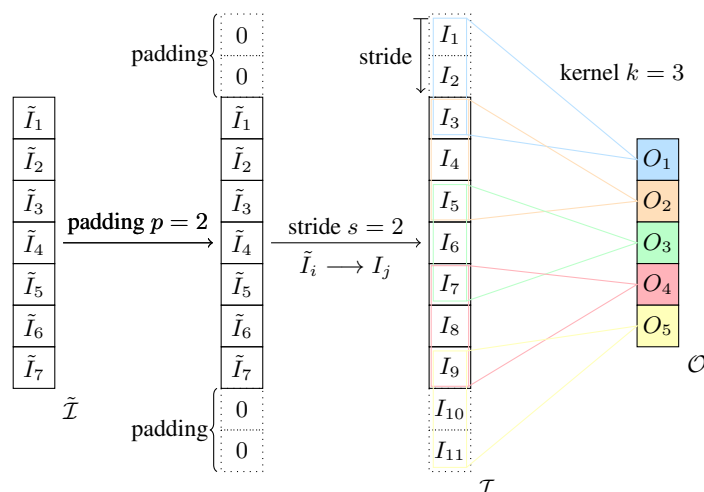


Figure 2.11: Maxpool layer on an input array $\tilde{\mathcal{I}} = [\tilde{I}_1, \dots, \tilde{I}_7]$ of the size $N_I = 7$ with a kernel of the size $k = 3$, with padding size $p = 2$, and stride set to $s = 2$. This leads to an output vector $\mathcal{O} = [O_1, \dots, O_5]$ of the size $M_O = 5$.

2.7.3 Maxpool Layer

As the name indicates, the Maxpool layer calculates the maximum values of the input in a certain way. Similarly to the convolutional layer in the previous Section 2.7.2, a padding of size p adds p zero values on the boundary of the array, as visualized in Figure 2.11. Hence, we get the array

$\mathcal{I} = [0, \dots, 0, \tilde{\mathcal{I}}, 0, \dots, 0] = [I_1, \dots, I_N]$ of the size $N = \tilde{N} + 2 \cdot p$. The kernel of the size k takes k consecutive entries of the array \mathcal{I} and calculates its maximum for the output. That is, the entry O_1 of the output array \mathcal{O} is

$$O_1 = \max\{I_1, \dots, I_k\},$$

or concretely $O_1 = \max\{I_1, I_2, I_3\}$ in the example illustrated in Figure 2.11. As before, the stride s skips the next s entries of the array to calculate the next maximum. Therefore, we can generalize the equation to

$$O_j = \max\{I_{s(j-1)+1}, \dots, I_{s(j-1)+k}\},$$

yielding, for instance, $O_3 = \max\{I_5, I_6, I_7\}$ in the above. The output size can be calculated similarly to the convolutional layers given in Equation 2.30. We note that this layer is used to downsample, resp. pool features and highlights the most present feature in the patch. It has no weights and therefore does not change during the training of the network.

2.7.4 Activation Function: ReLU

An activation function is generally placed after a fully-connected or convolutional layer. According to [35, 52, 54], a feed-forward network can approximate any continuous function, which is compact in \mathbb{R}^n under a mild assumption of the activation function. It is further generalized in [52], where the only condition of the activation function $\sigma : \mathbb{R} \rightarrow \mathbb{R}$ is that it shall not be a polynomial. A common and well-performing activation function is the **ReLU** activation function

$$\sigma(x) = \text{ReLU}(x) = \max\{0, x\} = \begin{cases} x, & x > 0 \\ 0, & x < 0 \end{cases}$$

which is continuously differentiable in $\mathbb{R} \setminus \{0\}$ and results in the unit step function

$$\sigma'(x) = \frac{\partial}{\partial x} \text{ReLU}(x) = \begin{cases} 1, & x > 0 \\ 0, & x < 0 \end{cases},$$

as visualized in Figure 2.12.

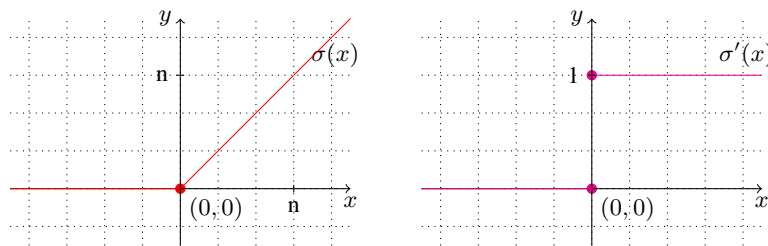


Figure 2.12: On the left side is the **ReLU** activation function $\sigma(x) = \max\{0, x\}$ which is undefined at position 0 and on the right side its derivation $\sigma'(x)$.

Chapter 3

Sentinel Lymph Node Fingerprinting

This publication is a continuation of the work of [79, 84]. To know if a cancer has spread, a biopsy of the SLN is done [81, 82]. This is done by injecting the patient with Tc^{99m} around the tumor, whereupon the Tc^{99m} accumulates in the SLN. Using a γ detector, these SLN can be found and removed. We aim to accurately pinpoint these SLNs so that the surgeon can operate minimally invasively.

In our previous work [79, 84], we used a multiple pinhole collimator, in which all pinholes were separated with septum walls, to detect the Tc^{99m} sources *ex-vivo*. One of the drawbacks was that the computation time was long and not applicable in real-case scenarios. In addition, the accuracy was limited. In this paper, we introduce the Sentinel Lymph Node Fingerprinting (SLNF) algorithm, increases the reconstruction's accuracy and speed. In addition, we use the optimal design method proposed in [31] to give mathematical reasoning as to why the reconstruction improves when removing the septum walls. With the optimal design method, we found new positions of the pinholes, that provides us with a better reconstruction of the Tc^{99m} sources.

In this paper, we are solving two inverse problems. The first one is finding the position of the Tc^{99m} sources or, in other words, for which position of the Tc^{99m} sources (condition) we get the image on the detector (measurement). The second one is what pinhole designs are a good condition to find the position of the Tc^{99m} sources.

Publication. This following paper [66] was published on the 5th of June 2019 in the *Physics in Medicine and Biology* Journal. We note that *Uri Nahum* (Postdoc) and *Carlo Seppi* (Ph.D. Student) are shared authors, and that the order of these authors is alphabetical.

PAPER

Sentinel lymph node fingerprinting

To cite this article: Uri Nahum *et al* 2019 *Phys. Med. Biol.* **64** 115028

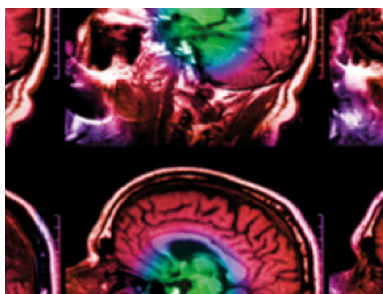
View the [article online](#) for updates and enhancements.

You may also like

- [Silica-coated gold nanoplates as stable photoacoustic contrast agents for sentinel lymph node imaging](#)
Geoffrey P Luke, Ashvin Bashyam, Kimberly A Homan *et al.*
- [The use of \$^{99m}\text{Tc-Al}_2\text{O}_3\$ for detection of sentinel lymph nodes in cervical cancer patients](#)
I G Sinilkin, V I Chernov, A Yu Lyapunov *et al.*
- [Bevacizumab loaded solid lipid nanoparticles prepared by the coacervation technique: preliminary *in vitro* studies](#)
Luigi Battaglia, Marina Gallarate, Elena Peira *et al.*

Recent citations

- [CdTe compact gamma camera for coded aperture imaging in radioguided surgery](#)
Paolo Russo *et al*
- [Peter A. von Niederhäusern *et al*](#)


IPEM | IOP

Series in Physics and Engineering in Medicine and Biology

Your publishing choice in medical physics,
 biomedical engineering and related subjects.

Start exploring the collection—download the
 first chapter of every title for free.



PAPER

Sentinel lymph node fingerprinting

RECEIVED
9 October 2018

REVISED
14 March 2019

ACCEPTED FOR PUBLICATION
3 April 2019

PUBLISHED
5 June 2019

Uri Nahum^{1,3,4} , Carlo Seppi^{1,3}, Peter A von Niederhäusern¹ , Simon Pezold¹, Stephan K Haerle²
and Philippe C Cattin¹

¹ Department of Biomedical Engineering (CIAN), University of Basel, Allschwil, Switzerland

² Head and Neck Surgical Oncology, Hirslanden Clinic St. Anna, Luzern, Switzerland

³ Equal contributor.

⁴ Author to whom any correspondence should be addressed.

E-mail: uri.nahum@unibas.ch

Keywords: sentinel lymph node detection, fingerprinting, 3D reconstruction, freehand SPECT, multi-pinhole collimator, optimal design, optimal control

Abstract

Background. When locating the sentinel lymph node (SLN), surgeons use state-of-the-art imaging devices, such as a 1D gamma probe or less widely spread a 2D gamma camera. These devices project the 3D subspace onto a 1D respectively 2D space, hence losing accuracy and the depth of the SLN which is very important, especially in the head and neck area with many critical structures in close vicinity. Recent methods which use a multi-pinhole collimator and a single gamma detector image try to gain a depth estimation of the SLN. The low intensity of the sources together with the computational cost of the optimization process make the reconstruction in real-time, however, very challenging.

Results. In this paper, we use an optimal design approach to improve the classical pinhole design, resulting in a non-symmetric distribution of the pinholes of the collimator. This new design shows a great improvement of the accuracy when reconstructing the position and depth of the radioactive tracer. Then, we introduce our Sentinel lymph node fingerprinting (SLNF) algorithm, inspired by MR-fingerprinting, for fast and accurate reconstruction of the tracer distribution in 3D space using a single gamma detector image. As a further advantage, the method requires no pre-processing, i.e. filtering of the detector image. The method is very stable in its performance even for low exposure times. In our *ex vivo* experiments, we successfully located multiple Technetium 99m (Tc-99m) sources with an exposure time of only one second and still, with a very small L^2 -error.

Conclusion. These promising results under short exposure time are very encouraging for SLN biopsy. Although, this device has not been tested on patients yet, we believe: that this approach will give the surgeon accurate 3D positions of the SLN and hence, can potentially reduce the trauma for the patient.

1. Background

Among the types of cancer in the head and neck area, oral and oropharyngeal squamous cell carcinoma are very typical. If initial staging cannot rule out an extensive spreading of the cancer, the standard of care includes the complete surgical removal of the lymph nodes in the vicinity. Post-resection analysis has shown, however, that this invasive intervention was only warranted in about 30% of the patients (Byers *et al* 1988, van den Brekel *et al* 1996). A biopsy of the SLN, i.e. the first draining lymph node(s) after the tumor, has shown to be a good indicator whether the tumor already spread through the lymphatics (Shoib *et al* 2001, Stoeckli *et al* 2001) and complete removal of the lymphnodes is warranted. To identify these SLN, radioactive tracer (Tc-99m) is injected around the tumor. After some hours, the highest concentration of the radio-active tracer is found in the SLN and hence can be located using a gamma detector. Surgeons either use a 1D gamma probe (Sullivan *et al* 2001, Hayashi *et al* 2003, Povoski *et al* 2009, Civantos *et al* 2010) or a 2D gamma camera (Gerbaudo *et al* 2002, Vermeeren *et al* 2010, Ozkan and Eroglu 2015, Hellingman *et al* 2015), to locate the SLN. These types of detectors have no depth perception in finding the SLN, or need preoperative imaging aid, an additional tracking device or multiple detectors to get a depth perception. An alternative is the freehand SPECT device, which is introduced in Mandapathil *et al* (2014) and Hellingman *et al* (2015). Although (Mandapathil *et al* 2014) is able to give a 3D approximation of the SLN,

an optical tracking device is needed with multiple images from the detector, while in Hellingman *et al* (2015) the pinhole collimator is only used to increase the resolution. In Jaszczak *et al* (1994), the authors proposed on using a SPECT camera with a pinhole collimator instead of a parallel hole collimator to measure the tracer distribution. Furthermore, by increasing the number of pinholes (resulting in a multi-pinhole collimator), the sensitivity is improved, hence allowing a reduction of the Tc-99m activity (dosage) injected.

Quantification of radioactive tracer distribution for SLN detection has proven itself as a useful approach (Alex and Krag 1993, Britten 1999, Warncke *et al* 2007). Nevertheless, the state-of-the-art approaches suffer from a host of challenges such as a long exposure time of the detector to the radioactive source(s), pre-processing of the gamma detector image, images from several angles are needed for the depth reconstruction, long computation-time of an ill-posed optimization method, poor depth control, lack of sensitivity for two sources located behind each other and the results may suffer from a post-processing step or a reader bias in locating the position of the source(s).

In this publication, we propose a novel multi-pinhole based collimator together with a processing algorithm that overcomes the above mentioned drawbacks. In contrast to our previous work (von Niederhäusern *et al* 2016, Seppi *et al* 2017), we introduce here a fast and accurate processing approach, inspired by MR-fingerprinting. Fingerprinting for MR images became very popular in the last years. Using a unique fingerprint for the data, pattern recognition algorithms are used to find the fingerprint in a predefined dictionary, see for example (Allen and Stott 2003, Zhang *et al* 2003). Instead of using an optimization method or huge dictionaries with complex optimization methods, the proposed approach uses a reduced dictionary and inquires low memory and a short runtime. The detection algorithm can be performed in a few seconds, even on a standard laptop, and gives results which are very close to the true position of the source(s). Our *ex vivo* experiments using multiple Tc-99m sources underpin the accuracy and precision of our approach.

This paper is organized as follows: first, we show how to improve our multi-pinhole collimator, inspired by the optimal design approach (Haber *et al* 2008), resulting in a non-symmetric distribution of the pinholes. Second, we introduce the SLNF algorithm for the detection of the radioactive tracer positions. Then, we perform experiments with different exposure times and different dictionaries. At last, we demonstrate the superiority of our new collimator design (non-symmetric distribution of the pinholes) in a comparative study with the previous collimator design (regular distributed pinholes with septum walls).

2. Method

In our experiments, we use a PILATUS3 gamma detector produced by DECTRIS Ltd. (5405 Baden-Dättwil, Switzerland). The detector features 487×195 pixels, with each pixel having a size of $172 \times 172 \mu\text{m}$. The gamma detector's CMOS readout ASICs uses cadmium telluride as the sensor-material. This technology allows direct detection of the gamma rays, where each signal generated by the pixel of the sensor is amplified, discriminated and counted. Our custom design collimator was manufactured by an external company. It is composed of 3D printed and machined tungsten parts, with a density of 19.25 g cm^{-3} and the dimension of $86.9 \times 36 \times 36 \text{ mm}^3$. Further, the cylindrical shaped pinholes, with a diameter of 1 mm, are drilled through the 1 mm thick front plate.

In front of the detector/collimator, we place one or more sources in several known positions, see figure 2. In our experiments, we use Tc-99m samples as radioactive sources. The photons are propagating through the pinholes of the collimator and hit the detector in a randomly distributed way.

Let u be a three-dimensional subspace of \mathbb{R}^3 in front of the collimator which contains radioactive tracers. The relationship between u and the detector image d can be described by the linear system

$$Au = d. \quad (1)$$

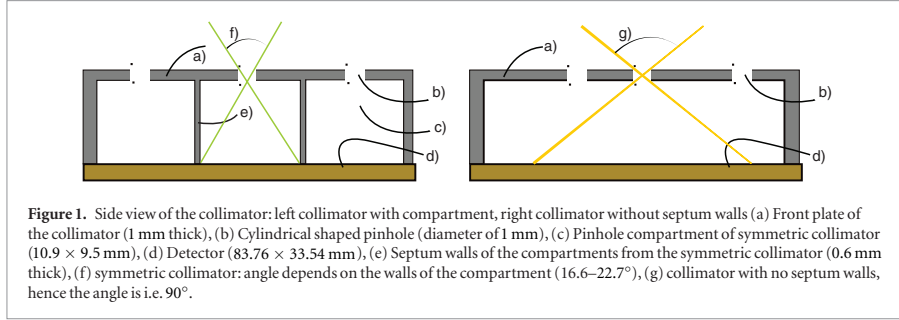
The projection matrix $A \in \mathbb{R}^{N_d \times N_u}$, which is dependent on the design of the collimator and its pinholes, is built to translate the sources to their detector image. The numbers N_u and N_d represent the number of discretization points of u and the number of pixels on the detector, respectively.

2.1. Optimal design of the pinhole distribution

In previous experiments (von Niederhäusern *et al* 2016, Seppi *et al* 2017) the collimator in figure 3 was used. Although, Seppi *et al* (2017) achieved a good localization in the xy -plane, its depth accuracy (z -axis) was limited. Here, we aim to find a good pattern for the pinholes on the collimator front plate such that 3D estimations are improved, hence the approximation of the depth (z -axis) improved.

To improve the depth estimation, the sources must be seen on the detector from multiple angles. This can be done by removing the septum walls in the collimator, see figures 1 and 6.

In Haber *et al* (2008), an optimal design for large-scale linear ill-posed inverse problems was introduced. Adapting this approach for our experiments, we find an optimal collimator design, i.e. an optimal distribution of the collimator's pinholes for improved 3D localization of the sources. Here, we examine $N_p = 200$ possible



pinholes for some given subspace u containing radioactive tracer(s). In figure 4, we illustrate the 200 possible pinholes marked with white dots.

For each pinhole p_m , $m = 1, \dots, N_p$, we build a projection matrix A_m . The matrix A_m projects the component of u through the *single pinhole* p_m onto the detector image d_m . The photons hit the detector in a stochastic process, which numerical simulation cannot precisely imitate. Therefore, we write

$$d_m = A_m u + \varepsilon_m. \quad (2)$$

Here, ε_m represents the noise (e.g. intrinsic spatial resolution of the detector, scattered photons, photons penetrating the collimator walls) in the experiment, which has different probabilities for each detector pixel. Hence, the variable ε_m must be in the same dimension as the image of the detector d_m and we write for each $\varepsilon_m = [\varepsilon_{m,i}]_{i=1}^{N_d}$. We assume that each $\varepsilon_{m,i}$ is independent and identically distributed (i.i.d) random variable with a mean value of 0 and variance of σ^2 (here, σ depends on the number of photon reaching the detector).

For each pinhole p_m , we define a weight w_m , $m = 1, \dots, N_p$, where the weights w_m are the solution of

$$\arg \min_w \sum_{m=1}^{N_p} w_m \|d_m - A_m u\|_{L^2}^2, \quad \text{s.t. } w_m \geq 0 \quad (3)$$

where $w = [w_1, w_2, \dots, w_{N_p}]^T$. Note, that the L^2 -norm is defined as

$$\|v\|_{L^2} = \left(\sum_i v_i^2 \right)^{1/2} \quad \text{for } v = [v_1, \dots, v_{N_v}] \in \mathbb{R}^{N_v}.$$

We write (3) in matrix form:

$$\arg \min_w (d - Au)^T W (d - Au), \quad (4)$$

where

$$A = \begin{pmatrix} A_1 \\ A_2 \\ \vdots \\ A_{N_p} \end{pmatrix}, \quad d = \begin{pmatrix} d_1 \\ d_2 \\ \vdots \\ d_{N_p} \end{pmatrix} \quad \text{and} \quad W = \begin{pmatrix} W_1 & & \\ & \ddots & \\ & & W_{N_p} \end{pmatrix},$$

with $W_m = \text{diag}(w_m, w_m, \dots, w_m) \in \mathbb{R}^{N_d \times N_d}$, $w_m \geq 0$, for $m = 1, \dots, N_p$. Note that, A is not a square matrix, hence, A is not invertible. Following (Haber *et al* 2008), we find a solution of (4) by minimizing the equivalent equation

$$\arg \min_w \mathcal{J}(w) = \arg \min_w \left(\sigma^2 \mathcal{V}(w) + \beta \sum_{m=1}^{N_p} w_m \right), \quad \text{s.t. } w_m \geq 0, m = 1, \dots, N_p, \quad (5)$$

with

$$\mathcal{V}(w) = \text{trace}(WAC(w)^{-2}A^T W) \quad \text{and} \quad C(w) = A^T W A \quad (6)$$

and β has typically a small value (here, we choose $\beta = 10^{-2}$). To reduce computation cost we approximate the trace (Golub and Von Matt 0000, Hutchinson 1990) in (6) as

$$\text{trace}(H) \approx v^T H v,$$

where v is a random vector of i.i.d. entries of values ± 1 with the probability of $1/2$. Hence, we approximate $\mathcal{V}(w)$ through $\hat{\mathcal{V}}(w)$

$$\hat{\mathcal{V}}(w) = v^T W A C(w)^{-2} A^T W v = w^T V(w)^T V(w) w, \quad \text{with} \quad V(w) = C(w)^{-1} A^T \text{diag}(v).$$

We replace $\mathcal{V}(w)$ in (5) with $\hat{\mathcal{V}}(w)$ and get

$$\arg \min_w \hat{\mathcal{J}}(w) = \arg \min_w \left(\sigma^2 \hat{\mathcal{V}}(w) + \beta \sum_{m=1}^{N_p} w_m \right), \quad \text{s.t. } w_m \geq 0, m = 1, \dots, N_p. \quad (7)$$

To optimize (7), we compute the gradient and the Gauss–Newton (G–N) approximation of the Hessian of $\hat{\mathcal{V}}(w)$ with respect to w . First, we compute the gradient

$$\nabla \hat{\mathcal{V}}(w) = \nabla [w^T V(w)^T V(w) w] = 2J_v(w)^T V(w) w$$

where

$$J_v(w) = \frac{\partial [V(w) w]}{\partial w} = V(w) - C(w)^{-1} A^T \text{diag}(A r_v) \quad \text{with} \quad r_v = V(w) w_{\text{fixed}} \quad (8)$$

and w_{fixed} is a fixed w .

Remark 1. We omit the long description of technical details. The steps (4)–(8) serve as referencing point to understand the detailed explanation in Haber *et al* (2008).

Next, we compute the G–N approximation of the Hessian

$$\Delta \hat{\mathcal{J}} \approx \sigma^2 J_v^T J_v.$$

To find a search direction for the optimization, we solve in each G–N iteration the system

$$\Delta \hat{\mathcal{J}} p = -\nabla \hat{\mathcal{J}}. \quad (9)$$

For an efficient solution of (9) we opt for the inexact Newton method, where we solve the inner iteration using the conjugate gradient (CG) method (Haber *et al* 2000, Grote *et al* 2017). We iterate in both G–N and CG iterations until a relative residuum of 0.1 is reached. Starting with equal weights for all $w_m = 1$ for $m = 1, \dots, N_p$, we optimize (7) and find the weights w_m with the highest values. The pinholes p_m corresponding to those highest weights are the most essential pinholes for the reconstruction.

Remark 2. To compare different collimator designs we fix the number and the position of the pinholes and solve (6). Further, the collimator with the smallest $\mathcal{V}(\mathbf{1})$ value, with $\mathbf{1} = [1, \dots, 1]$, is the collimator of choice.

2.2. Optimal design for known sources

To conclude how the holes are distributed on the collimator, we solve (7) for four different sub-spaces u : with one, two, three and four sources with a diameter of 5 mm (approximated size of the lymph node). We start with 200 possible pinholes (all of them have a diameter of 1 mm), shown in figure 4. In figure 5, the 24 white dots correspond to the resulting 24 pinholes with the highest weight (the number 24 is taken from Seppi *et al* (2017), to compare the results with the symmetric collimator discussed in this paper) and the big red dots corresponding to the (x, y) position of the source(s) (they were located at a distance of 100–150 mm from the collimator front plate respectively).

Although the process gives a clear suggestion for each experiment, in reality the positions of the sources are not known and the optimization selects each time a different pinhole combination with respect to the position of the source(s). In all of the experiments performed, there were, however, two common properties:

- (i) The pinholes are spread over the entire collimator front plate.
- (ii) The pinholes are spread non-symmetrically.

Actually, if we initiate the optimal design process with symmetrically distributed pinholes (see right side of figure 6), the optimal design optimization breaks the symmetry. A major drawback of the examples given above, is that they show only one possible design for a single subspace u and neglect all other sub-spaces. We built a collimator with the properties mentioned above and introduce it on the left of figure 6. To ensure, the superiority of the new collimator we compare it to the symmetric collimator (with and without septum walls). We solve $\mathcal{V}(\mathbf{1})$ in equation (6) (with $\mathbf{1} = [1, \dots, 1]$) for 100 randomly chosen subspaces with one, two, three and four sources. The mean value of (6) from the collimators without septum walls (figure 6) are at least three times smaller than for the symmetric collimator with septum walls (figure 3). Additionally, all the mean values of the symmetric

Table 1. Comparison between the symmetric collimator (with and without septum walls) and the non-symmetric collimator for optimal design: mean value of $\mathcal{V}(\mathbf{1})$ in equation (6) (with $\mathbf{1} = [1, \dots, 1]$) for 100 randomly chosen subspace with one, two, three and four sources.

Number of sources	1	2	3	4
$\mathcal{V}(\mathbf{1})$ value of symmetric-collimator (with septum walls)	5.44	10.70	15.95	22.37
$\mathcal{V}(\mathbf{1})$ value of symmetric-collimator (no septum walls)	1.41	2.14	3.41	4.82
$\mathcal{V}(\mathbf{1})$ value of non symmetric-collimator	0.98	2.01	3.32	4.00

breaking collimator are lower than the one with symmetric pinholes. Hence, the new non-symmetric collimator proves itself as a good choice in our optimal design process (see table 1). Clearly, this design is not a perfect optimal design for all combination of sources, and yet, we show in our *ex vivo* experiments the superiority of the new symmetry breaking design, in comparison to the symmetric designs.

2.3. Dictionary

Let u be a subspace containing a single source at the position (20, 50, 140) mm. We use (1) to compute the corresponding detector image d_1 as shown on the top left of figure 7. Next, we consider a slightly different position of the source: (21, 50, 140) mm (i.e. we change the position of the x coordinate by 1 mm). The computed corresponding detector image d_2 for this source is shown on the top right of figure 7. Even though we changed the position of the source by just 1 mm in the horizontal direction x , the changes on the resulting detector image are evident, as can be seen on the bottom of figure 7, where we show the difference $d_1 - d_2$ between the detector images. Similar results can be seen when changing the position slightly in the y and z directions. In the following, we take advantage of this sensitivity of the detector image to small changes in the source position to get a very fast and robust reconstruction of the position of the sources.

Here, we build a dictionary of computed detector images, which holds all the projections of all source positions in our 3D subspace onto the detector. When performing an experiment, a detector image d^{true} is produced. Then, we use a coherency functional

$$\mathcal{C} : \mathbb{R}^{N_d} \rightarrow \mathbb{R},$$

to find the image in the dictionary with the highest coherency to d^{true} . The detected source is the one corresponding to the image where \mathcal{C} gets its global maximum (for the choice of \mathcal{C} we refer to section 2.4). In an optimal situation, we would like to have a dictionary containing all detector images for all numbers of sources and their combinations. This is, unfortunately, impossible. Even if we restrict the reconstruction to a maximum number of three sources, in a subspace of $30 \times 80 \times 100 \text{ mm}^3$, with a coarse grid of 3 mm between the sources. The following number of matrices with the size of 487×195 would have to be stored:

$$\binom{8580}{1} + \binom{8580}{2} + \binom{8580}{3} = 105,271,459,150.$$

Since this is impossible on a standard computer, we reduce the dictionary only to images corresponding to a single source. In the example described above, we reduce the number of entries of the dictionary to 8580. In the following (section 2.4), we show how it is still possible to find multiple sources using this reduced dictionary. This is done in an iterative process. Since the images for a single source in the dictionary are sparse (see figure 7, for example) we can store them easily without any special memory requirements.

Note, that we locate the center of the Tc-99m source (diameter 5–7 mm). Hence, even a small error can still be within the diameter of the source.

2.4. SLNF algorithm

Here, we want to define the requirements of the functional \mathcal{C} . Let u_1 respectively u_2 be two 3D subspaces containing a single radioactive tracer s_1 respectively s_2 , and let s be one of the sources in the true subspace u . The radioactive sources s_1 and s_2 assumed to be within Euclidean space distances, $\text{dist}(s_1, s)$ and $\text{dist}(s_2, s)$, which are not too large. Let d_1 respectively d_2 be the detector images in the dictionary representing the projection of the source s_1 respectively s_2 (using (1)). We seek for a functional \mathcal{C} , s.t.

$$\mathcal{C}(d_1) > \mathcal{C}(d_2), \quad \text{if } \text{dist}(s_1, s) < \text{dist}(s_2, s). \quad (10)$$

Having such a functional \mathcal{C} , we apply it on each detector image in the dictionary D and find the index in the dictionary where the coherency functional finds its maximum. Several functionals can be applied here and fulfill the above mentioned requirement. To get fast and reliable results, we follow (Ma *et al* 2013) and choose

$$\mathcal{C}(d) = \|d \circ d^{\text{true}}\|_{\mathbb{F}} = \sqrt{\sum_{ij} (d_{ij} \cdot d_{ij}^{\text{true}})^2}. \quad (11)$$

Here, the operator \circ denotes the Hadamard product and \mathbb{F} denotes the Frobenius norm. In other words: the higher the value of $\mathcal{C}(d)$, the more similar are d^{true} and d .

In figure 8, we visualize the principle of the coherency functional $\mathcal{C}(d)$ on a simplified example. In figure 8(a), we have the measured image d^{true} with noise (e.g. photons penetrating the collimator walls) and in the center the measured projection of the source (yellow). In the left column of figures 8(b)–(d) we have three simulated detector images d^1, d^2 and d^3 . These correspond to three different source positions P^1, P^2 and P^3 . Each value of the pixel of d^{true} is represented as d_{ij}^{true} and each pixel of the images d^ℓ is represented as d_{ij}^ℓ for $\ell = 1, 2, 3$, respectively. For this simplified example, we only choose the three aforementioned images d^1, d^2, d^3 for the dictionary D , hence we have $D = \{d^1, d^2, d^3\}$. In the right column of figures 8(b)–(d) we show the Hadamard multiplication, i.e. a pixel-wise multiplication, of d^ℓ and d^{true} (for all pixel entries we compute $d_{ij}^\ell \cdot d_{ij}^{\text{true}}$). The coherency functional $\mathcal{C}(d^\ell)$ in (11) is the quadratic sum of all the pixel from the resulting image. We observe, that d^1 covers the whole projection of the source, d^2 does not intersect with the projection and only the noise is observed. In the case of d^3 the projection is partially covered. As mentioned, the coherency functional $\mathcal{C}(d)$ in equation (11), compares the simulated detector images d from the dictionary D to the true detector image d^{true} . The more similar the images are, the higher is the value of $\mathcal{C}(d)$. We have the highest value from d^1 with $\mathcal{C}(d^1) = 216$ (where the whole projection is observed), the lowest value from d^2 with $\mathcal{C}(d^2) = 125$ (where only noise is observed) and the value for d^3 with $\mathcal{C}(d^3) = 167$. In conclusion, the dictionary entry d^1 , corresponding to the source P^1 , is the most similar to the measured image d^{true} , since its coherency value is the highest. Hence, we assume that the true source position corresponds to P^1 .

The dictionary D contains images corresponding only to a single source. However, u may contain more than one source and hence we find all sources in an iterative process:

Algorithm 1. SLNF: Finding the position of the radioactive sources using a predefined dictionary.

Input: a detector image d^{true} , dictionary of corresponding detector images D for all possible locations of sources p .

Output: position of sources L .

1. Evaluate $\mathcal{C}(d_i), \forall d_i \in D$ and set m as the median of all $\mathcal{C}(d_i)$
2. repeat until $\max(\mathcal{C}(d_i)) < \delta \cdot \log(m)$
 - 2.1. set i^* as the index i of the global maximum of \mathcal{C}
 - 2.2. add to $L \leftarrow p_{i^*}$
 % the i^* 's index of p is the approximation of the source
 % with the highest intensity.
 - 2.3. Set d^{true} to zero where $d_{i^*} > 0$
 % delete the values in the true detector image
 % corresponding to i^* to reveal another
 % possible source.
 - 2.4. update \mathcal{C} with the modified d^{true}
3. return L

In the first step of the algorithm, we evaluate \mathcal{C} on all the detector images in the dictionary and compute the median m for the stop criteria of the algorithm. If the maximum of \mathcal{C} is significantly higher than m , there is another source to be found (step 2). After saving the information of the source (step 2.1), we delete its corresponding information from the true detector image d^{true} (step 2.3). In the last step of the loop we update \mathcal{C} with the modified d^{true} (step 2.4). If the maximal value of \mathcal{C} is still significantly higher than m , there is another source to be found and the process is repeated. The loop finally breaks when the maximal value of \mathcal{C} is close to m , i.e. there is no significant activity on the detector, that correlates to a source. Hence, all sources are found.

Remark 3.

- The images d_i in the dictionary D are highly sparse. On average, more than 97% of the entries in d_i are zero. Hence, the computation can be run very fast without any special memory requirements.
- The sequence in which we find the sources is a non-increasing sequence of intensities, i.e. the algorithm finds the sources from the strongest to the weakest intensity.
- With the non-symmetric collimator the parameter δ was experimentally chosen for every exposure time.
- Another possibility for automatic detection of the number of sources is using deep neural network. First results on simulated detectors images has shown very good results, and in the future, we plan on refining this approach using real patient data.

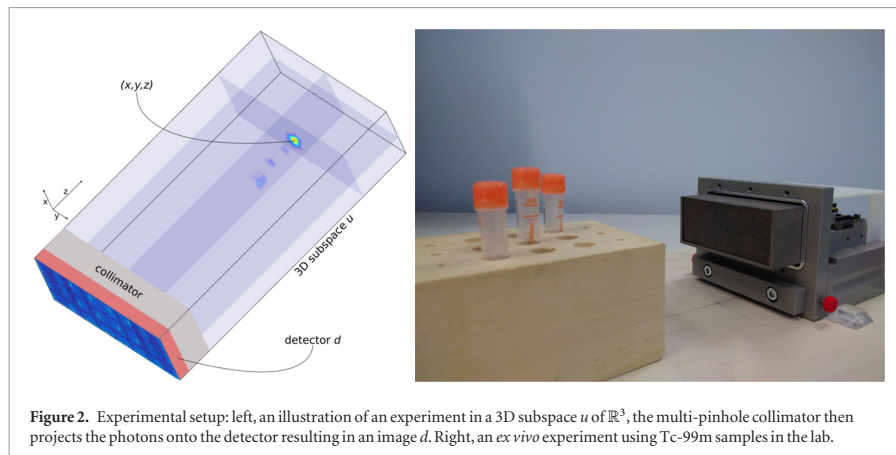


Figure 2. Experimental setup: left, an illustration of an experiment in a 3D subspace u of \mathbb{R}^3 , the multi-pinhole collimator then projects the photons onto the detector resulting in an image d . Right, an *ex vivo* experiment using Tc-99m samples in the lab.

Table 2. Seven different experiments with Tc-99m in the lab and reconstruction of the source positions using a detector which was exposed for one resp. 16 s to the sources using the new non-symmetric collimator.

#	True position(s) in mm	Reconstruction with 1 s in mm	L^2 -error in mm	Mean in mm	Reconstruction with 16 s in mm	L^2 -error in mm	Mean in mm
1	(21, 41, 130)	(20, 42, 128)	2.4	2.4	(20, 42, 130)	1.4	1.4
2	(21, 41, 130)	(20, 42, 130)	1.4	5.3	(20, 42, 130)	1.4	2.2
	(26, 21, 110)	(26, 22, 101)	9.1		(26, 21, 107)	3	
3	(21, 41, 130)	(20, 41, 131)	1.4	9.6	(20, 41, 127)	3.2	3.2
	(16, 21, 130)	(14, 22, 130)	2.2		(15, 22, 127)	3.3	
	(26, 61, 150)	(24, 63, 175)	25.2		(24, 63, 149)	3	
4	(21, 41, 130)	(20, 42, 130)	1.4	1.8	(20, 42, 130)	1.4	2.4
	(16, 21, 130)	(15, 21, 132)	2.2		(15, 22, 127)	3.3	
5	(16, 21, 130)	(15, 22, 127)	3.3	4	(15, 22, 127)	3.3	4
	(26, 61, 130)	(25, 63, 134)	4.6		(25, 63, 134)	4.6	
6	(21, 41, 110)	(21, 41, 108)	2	4	(21, 41, 111)	1	2.2
	(21, 41, 150)	(18, 42, 145)	5.9		(18, 42, 149)	3.3	
7	(16, 21, 130)	(16, 22, 126)	4.1	—	(15, 21, 129)	1.4	5.3
	(21, 41, 150)	(20, 43, 153)	3.7		(19, 42, 144)	6.4	
	(26, 21, 110)	—	—		(26, 22, 102)	8.1	

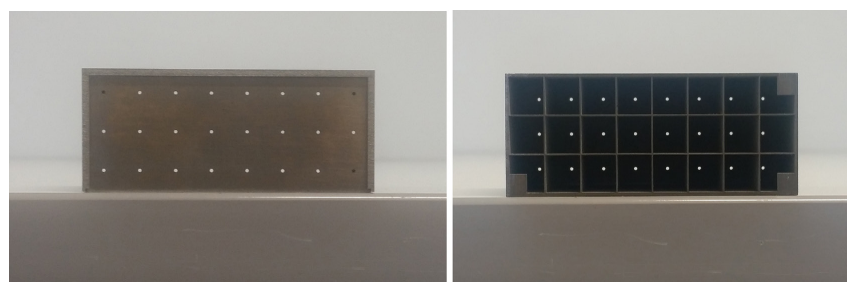


Figure 3. Symmetric collimator: a pinhole collimator with 24 compartments and 24 pinholes matching the centers of the compartment. Front view (left) and rear view (right).

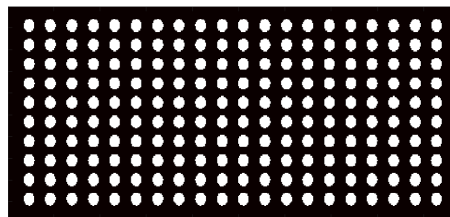


Figure 4. Optimal collimator design: 200 possible pinholes marked in white.

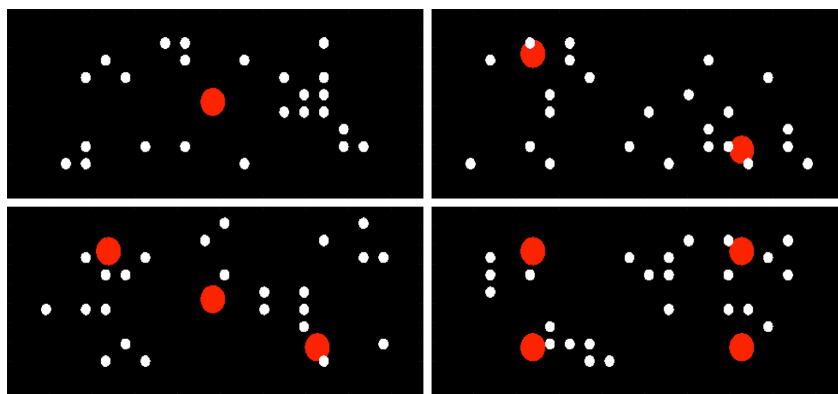


Figure 5. Optimal design: white circles represent the pinholes with the highest weights, given by solving (7) and red circles represents the (x, y) position of the source(s).

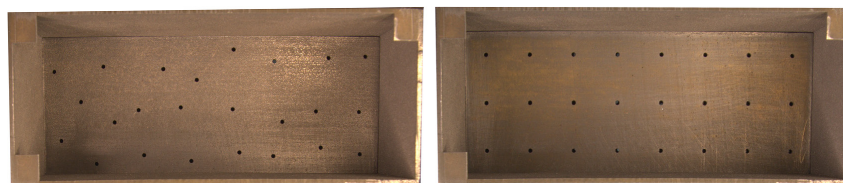


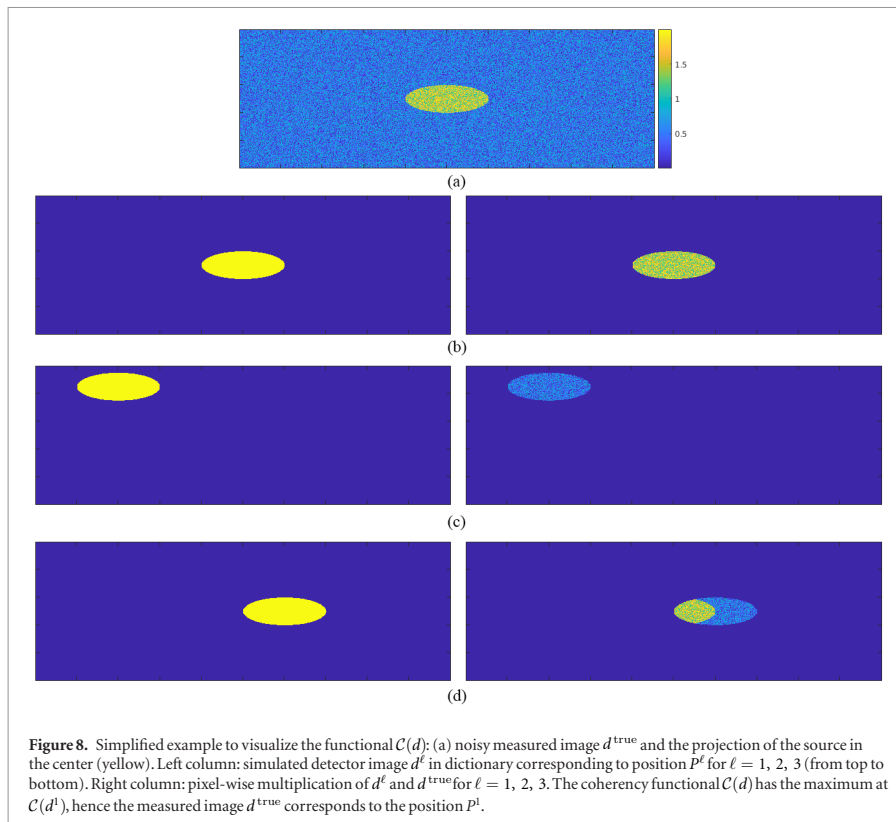
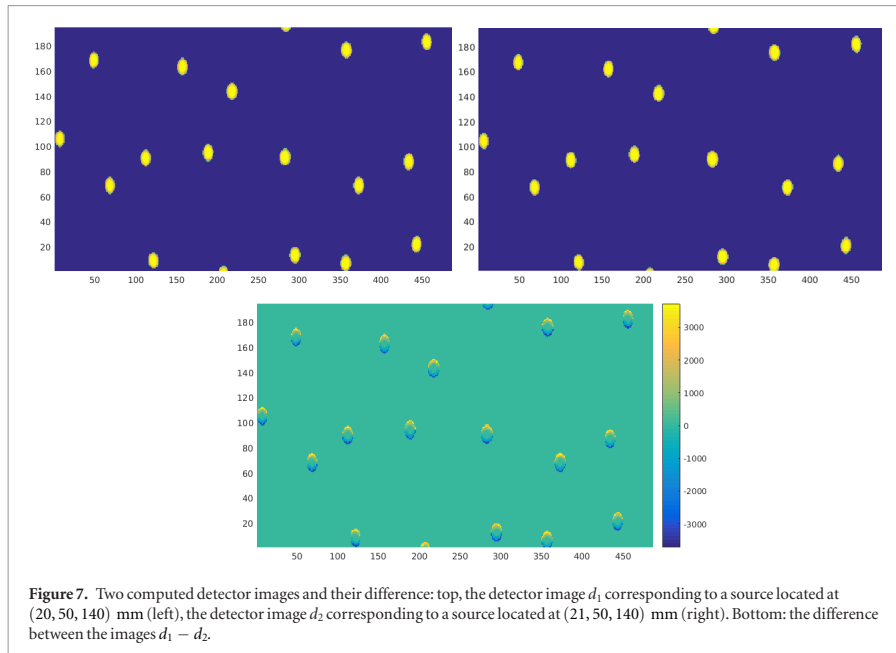
Figure 6. New collimator without septum walls: 24 pinhole collimator with non-symmetric pinholes (left) and the collimator with symmetric pinholes (right).

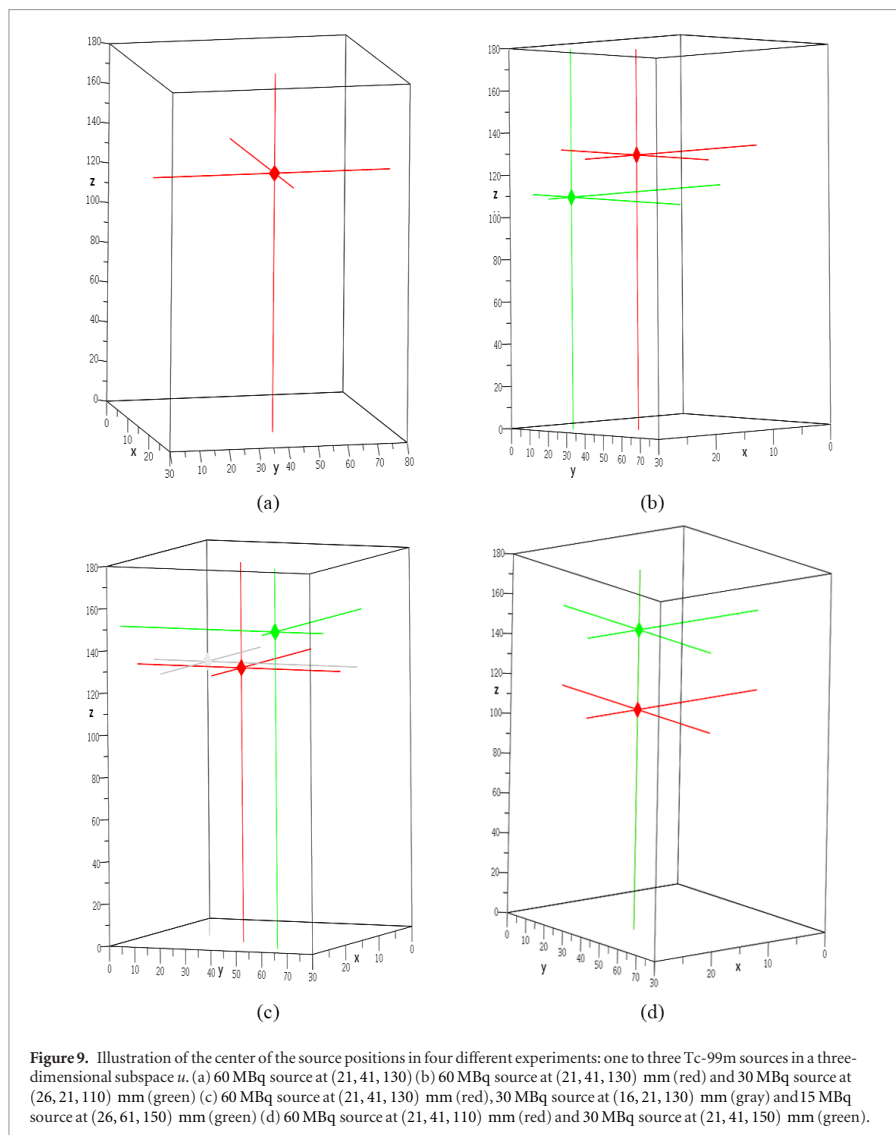
3. Results

In this section, we reconstruct the 3D position of the radioactive sources using a single 2D image of the detector. The image is received from the detector after placing up to three sources in different positions in front of the collimator and the detector (see figure 2). All veils are filled with a fluid of 19 ml with different strength of Tc-99m.

For the illustration of algorithm 1, we use a dictionary, that includes all detector images corresponding to all single sources in a subspace u of $30 \times 80 \times 180 \text{ mm}^3$ with a grid spacing of 1 mm in each direction. Moreover, we use detector images, produced by exposing the detector for 16 s to the sources. After illustrating the algorithm and its functionality, we compare the results with images received after an exposure time of one second to the sources, see section 3.4.

Remark 4. Four rectangular areas can be seen on the corners of the detector image, see for example on the right of figure 10. The big empty rectangle on the bottom right is due to a faulty sensor area of the detector. The other three rectangles are used to geometrically align the collimator to the detector. Despite these non-sensitive areas, the positional estimations of the detector are very accurate proving the robustness of the developed design and processing.

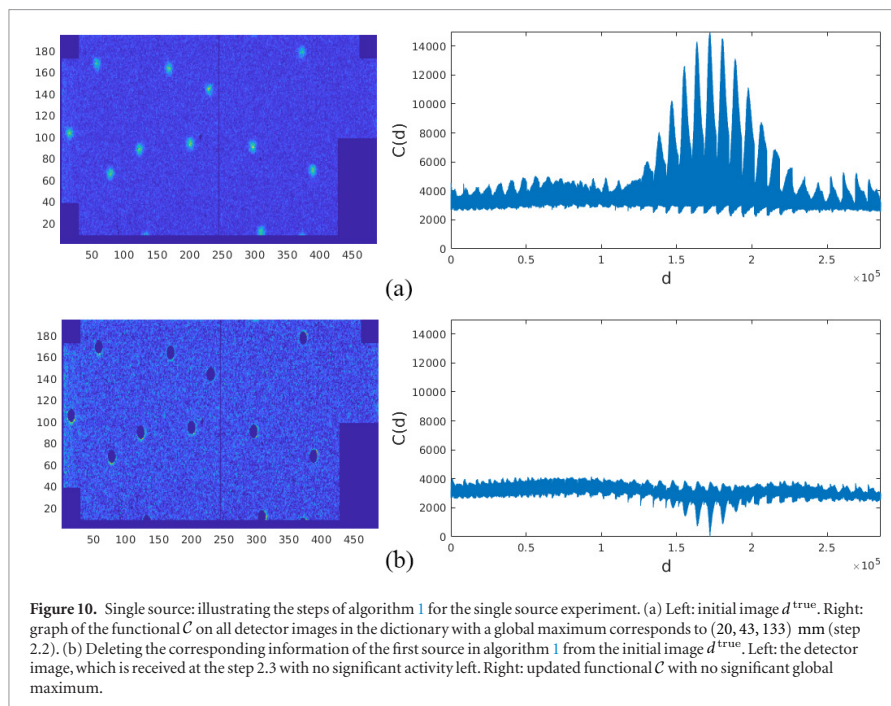




3.1. One source experiment

First, we consider a single Tc-99m source with an intensity of 60 MBq, located at the position (21, 41, 130) mm, as illustrated in figure 9(a) (the lines in the figure visualize the axes in the 3D subspace).

On the right of figure 10(a), we plot the functional \mathcal{C} evaluated on all detector images in the dictionary D . We remind the reader that the more similar the true detector image is to the detector image of the dictionary, the higher is the value of the functional \mathcal{C} . We find its maximum on the 172 159th entry of the dictionary. This entry corresponds to the point (20, 42, 130) mm. This yields a very small L^2 -error of 1.4 mm. Next, we delete the information corresponding to the source found from d^{true} , as described in step 2.3 of algorithm 1 and shown on the left of figure 10(b). Then, we update the functional \mathcal{C} with the modified detector image as in step 2.3 of algorithm 1 and plotted on the right of figure 10(b). Now, there is no significant activity left, i.e. the maximum of the functional \mathcal{C} is not significantly larger than its median m . Hence, all sources have been found and the algorithm terminates (see, algorithm 1, step 2).



Remark 5. Note that the other clear local maxima of \mathcal{C} , shown on the right of figure 10(a), correspond to sources in the close neighborhood of the located point.

3.2. Two sources experiment

Now, we consider a subspace u with two sources at (21, 41, 130) mm and (26, 21, 110) mm with intensities of 60 MBq and 30 MBq, respectively. In figure 9(b), we plot the sources, where the red color represents a source with higher intensity and the green color a weaker one.

On the right of figure 11(a), we plot the functional \mathcal{C} applied on the dictionary. The functional \mathcal{C} finds its global maximum at the 172 159th entry of the dictionary, which corresponds to a source located at (20, 42, 130) mm. We follow algorithm 1 and delete the corresponding information of the source found from d^{true} (see step 2.3 of algorithm 1 and figure 11(b), left). On the left of figure 11(b), we see that there is still significant activity left after deleting the corresponding information of the last source found. We update the functional \mathcal{C} , with the modified detector image (step 2.4) and evaluate it for all images of the dictionary (see figure 11(b), right). Indeed, the remaining activity is translated to a new clear global maximum of \mathcal{C} . The maximum is on the 220 606th entry of the dictionary, which corresponds to the source located at (26, 21, 107) mm. Following algorithm 1, we repeat the process until no significant activity remains (see figure 11(c)). The algorithm finds two sources with a remarkable mean L^2 -error of 2.2 mm.

3.3. Three sources experiment

Next, we consider a subspace u with three sources at the positions (21, 41, 130) mm, (26, 61, 150) mm and (16, 21, 130) mm with intensities of 60 MBq, 30 MBq and 15 MBq, respectively. In figure 9(c), we plot the sources and mark different intensities with different colors: from strongest to weakest: red, green and gray.

In figure 12, we plot the four different detector images, during the algorithm (we omit the graphs of \mathcal{C} , since they are similar to the ones showed in the previous examples). In the first three images a significant activity exists, which corresponds to an additional source. On the fourth detector image (bottom right of figure 12) there is no such activity left. Hence, the loop breaks in step 2 of algorithm 1. The algorithm finds three sources at the following positions: (20, 41, 127) mm, (15, 22, 127) mm and (24, 63, 149) mm. Again, the mean L^2 -error is very small and equal to 3.2 mm.

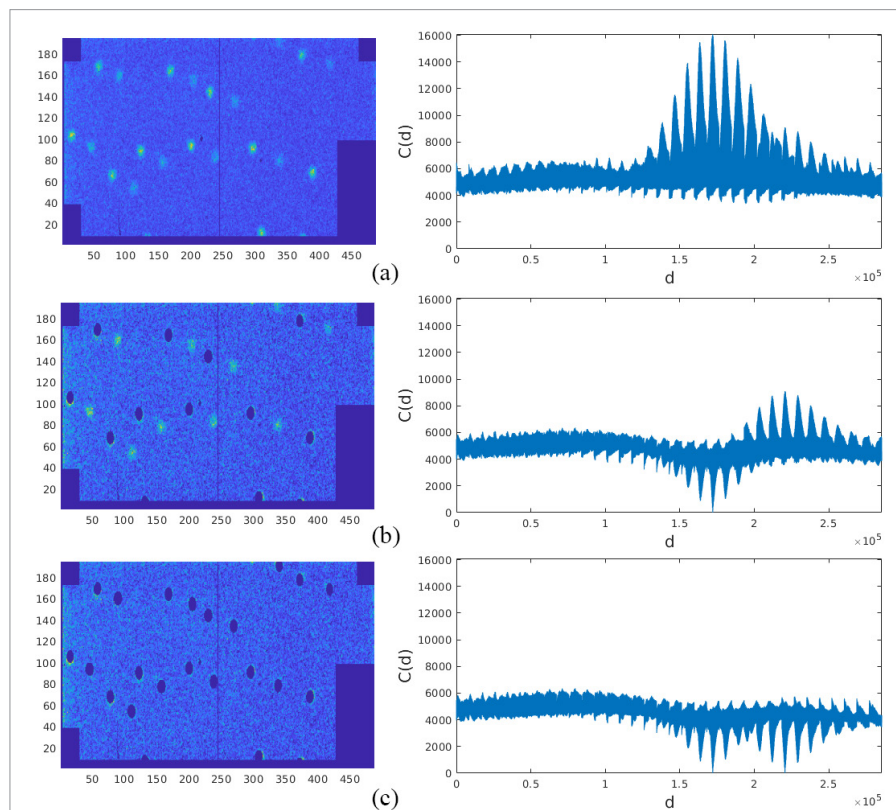


Figure 11. Illustrating the steps of algorithm 1 for two sources experiment. (a) Left: initial image d^{true} . Right: the functional C evaluated on all detector images in D with a global maximum corresponding to (20, 42, 130) mm (step 2.2). (b) Deleting the corresponding information of the first source from the initial image d^{true} . Left: detector image received in step 2.3 with significant activity left. Right: updated functional C in step 2.4, with a global maximum corresponds to (26, 21, 107) mm. (c) Deleting the corresponding information of the second source. Left: detector image received in step 2.3 with no significant activity left. Right: updated functional C in step 2.4, with no significant global maximum.

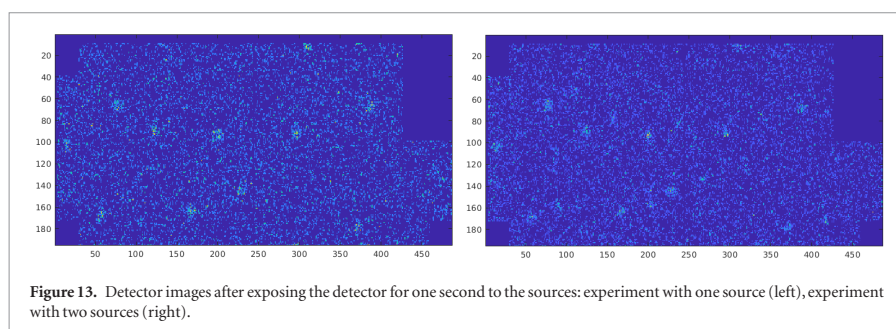
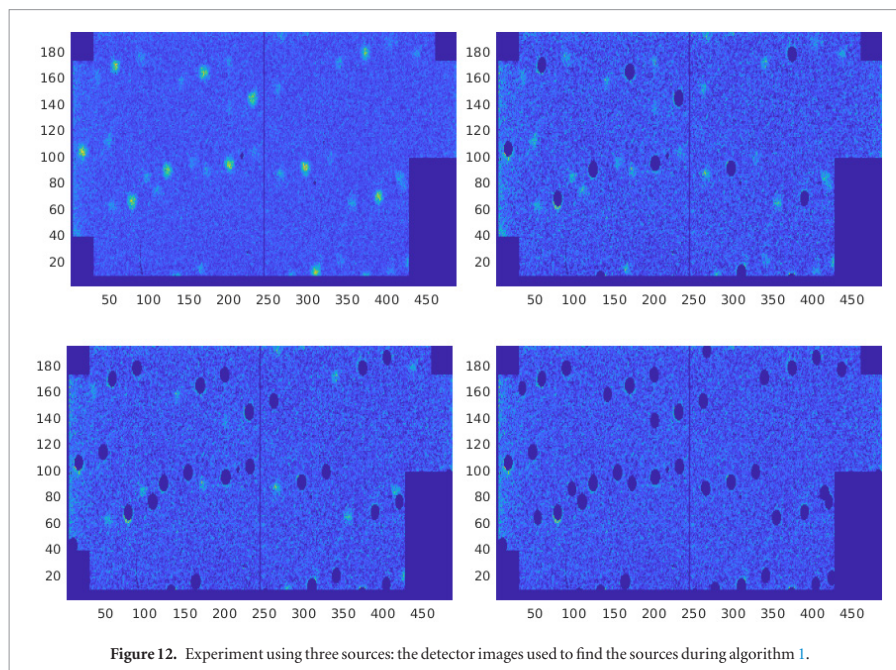
3.4. One second exposure of the detector to the sources

In this experiment we repeat the tests described above, but this time we expose the detector only for one second. 60 MBq is a higher dosage than generally measured in the SLN. Hence, it is utmost important to be able to reconstruct the images with a low exposure time. This enables us to use slightly longer exposure times to detect weaker radiant sources.

The number of photons detected when exposing the detector to the sources for one second decreases and the signal to noise ratio is drastically increased. In figure 13, we plot such images for the source combination described in sections 3.1 (left) and 3.2 (right). Although it seems that these images contain very limited data, the SLNF is able to extract all source positions with a small L^2 -error.

In table 2, we show seven different source combinations, with an exposure time of one second resp. 16 s. In experiments 1–3 in table 2, we use the same source positions and source intensities described in sections 3.1–3.3. In experiments 4 and 5, we present another two source combinations and their successful position detection.

The SLN in the body might be located in such way, that one SLN with a weak intensity is hidden behind another one with a higher intensity. We consider this case as a very challenging one. In experiment 6, we consider this case in the lab when we locate a weaker source exactly behind a stronger one. In this experiment, the subspace u contains two sources at the positions (21, 41, 110) mm and (21, 41, 150) mm with intensities of 60 MBq and 30 MBq, respectively. In figure 9(d), we illustrate the position of these sources. Again, the red color represents a source with higher intensity and the green color a weaker one. The robustness of the SLNF is again demonstrated in this experiment, when the results hold a small L^2 -error of less than 4 mm. In the case of twin SLN (two SLN very close to each other), the SLNF algorithm might detect them as a single source. This should not be a major problem, since the medical doctor will take them both out. Finally, we investigate in experiment 7a different



combinations of three sources. Although it does not find all the sources with one second exposure time, it still manages to find all the sources with an exposure time of 16 s with a mean L^2 -error of 5.3 mm.

Remark 6. If we reduce the dictionary from $30 \times 80 \times 180 \text{ mm}^3$ to $30 \times 80 \times 170 \text{ mm}^3$ we get a remarkable reduction of the error in experiment 3 for 1 s exposure time: the third source is now at (24, 63, 154), which reduces the mean error from 9.6 mm to 2.8 mm.

3.5. Error estimation

At last, we compare our choice of the non-symmetrical collimator, shown on the right of figure 6, with a symmetric distributed pinhole pattern, shown in figure 3. In figure 14, we compare the L^2 -error of the two collimators for up to three sources (the source combinations are those shown in sections 3.1–3.3). This time we expose the sources for different times: 1, 2, 4, 8 and 16 s. The advantage of the non-symmetrical distributed pinhole collimator is clear: the accuracy is very high, even for multiple sources with exposure time as low as one second. When using the symmetric collimator this is, unfortunately, not the case. In some experiments, especially in multiple sources, exposing the detector to the sources through the symmetric collimator for 16 s yields a higher L^2 -error with compare to the non-symmetric collimator for a single second. The comparison was repeated for some other source positions and similar results were shown.

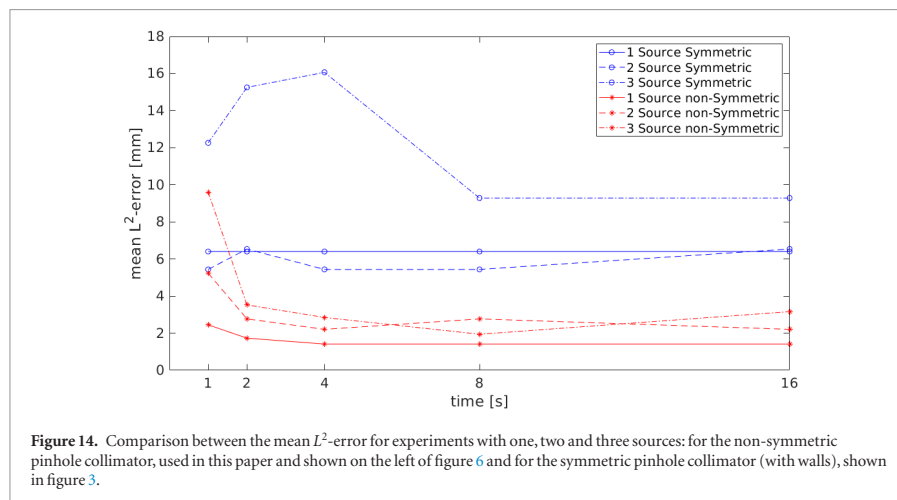


Figure 14. Comparison between the mean L^2 -error for experiments with one, two and three sources: for the non-symmetric pinhole collimator, used in this paper and shown on the left of figure 6 and for the symmetric pinhole collimator (with walls), shown in figure 3.

Remark 7. The symmetric collimator without septum walls, shown on the right of figure 6, provides often similar results to the non-symmetric collimator. However, In the case when two sources are located behind each other, which is very relevant in the detection of sentinel lymph-nodes, only the non-symmetric collimator is able to locate both of them. Actually, we discover in the experiment setup shown in figure 9(d) (with an exposure time of 16 s), that the symmetric collimator has a high mean L^2 -error of 18.3 mm and the non-symmetric collimator provides a remarkable low error of 2.2 mm. This experiment supports as well the superiority of the non-symmetrical collimator.

4. Discussion

We introduce a new approach using a single gamma detector image. The method improves accuracy and reduces the run time dramatically with respect to former methods using, for example, non-linear optimization. Using a single gamma detector image, can be a drawback, especially when two sources are located very close and exactly behind each other. In our experiments, the method had difficulties when two sources are under 20 mm away from each other in depth, but share the same horizontal and vertical values. In this situation, the methods show a single source, which is positioned exactly between the sources. The medical doctor will remove all lymph nodes around the detected position, and hence, will remove both sentinel lymph nodes in this case.

In head and neck melanoma, we may find an intensity which can be at least twenty times smaller than the one we used in this paper. Since we used a very short exposure time, we can increase it to more than 20 s to get similar results. In addition, we aim to improve our *ex vivo* experiment into a more realistic model, by adding a hot background.

We use a non-symmetric collimator without septum walls. Although this collimator is not a fully optimal design (an other random distribution of pinholes might be marginally more optimal) it proofs itself as a good choice. Not only in our optimal design process, but also in our *ex vivo* experiments it exceeds the symmetric designs and gives good results even under low exposure time.

Our device is still limited with regards to the field of view to solely the front of the collimator. However, due to the pinholes, we can measure activity of sources on the side of the collimator, but still in the field-of-view of the pinholes. This can be improved, by taking in account the whole field of view of all the pinholes and not solely the area directly in front of the collimator. Furthermore, a bigger, stationary device, e.g. built-in under the patient bed, can increase it further. Alternatively, a surgeon could use it as a portable device to receive live updates of the area of interest.

5. Conclusions

We introduce a new approach, the SLNE, for sentinel lymph node detection using a single gamma detector image. Furthermore, we show that our new non-symmetric collimator not only improves the accuracy of the reconstruction in comparison to the previous one (symmetric), but also enables very short exposure times. In

ex vivo experiments the method is able to find the 3D position of multiple Tc-99m sources. SLNF needs only a few seconds of computational time to locate the position of the sources and without any pre-processing of the gamma detector image.

The results of the algorithm are robust for multiple sources and its reliability is demonstrated. The robustness of our approach (also in depth) is a very critical aspect for SLN detection in the head and neck area, where important blood vessels and nerves are located.

In the future, we will test our approach on patients, where the radioactive intensity in the sentinel lymph nodes might be lower. Further, we will increase the measurable subspace to the field of view of the pinholes instead of solely in front of the collimator. This can ensure that the dictionary will cover all the possible positions of the measurement from the detector. Our promising results for one second exposure time and the remarkable robustness of our algorithm for different source positions and exposure times are, however, very encouraging.

Acknowledgments

We want to acknowledge Michael Rissi and Spyridon Gkoumas, who support us from DECTRIS Ltd. 5405 Baden-Dättwil, Switzerland. Further, we want to thank Nicolas Guillaume (University Hospital Basel), who provided the Tc-99m used in our experiments.

ORCID iDs

Uri Nahum  <https://orcid.org/0000-0001-6186-1830>

Peter A von Niederhäusern  <https://orcid.org/0000-0002-3878-5611>

References

- Alex J and Krag D 1993 Gamma-probe guided localization of lymph nodes *Surgical Oncol.* **2** 137–43
- Allen M and Stott P 2003 Estimating signal amplitudes in optimal fingerprinting, part I: theory *Clim. Dyn.* **21** 477–91
- Britten A J 1999 A method to evaluate intra-operative gamma probes for sentinel lymph node localisation *Eur. J. Nucl. Med. Mol. Imaging* **26** 76–83
- Byers R M, Wolf P F and Ballantyne A J 1988 Rationale for elective modified neck dissection *Head Neck* **10** 160–7
- Civantos F J, Zitsch R and Bared A 2010 Sentinel lymph node biopsy for oral cancer *Early Diagnosis, Treatment of Cancer Series: Head and Neck Cancers* ed W M Koch (Philadelphia: Content Repository Only!) ch 11, pp 201–22
- Gerbaudo V H, Sugarbaker D J, Britz-Cunningham S, Di Carli M F, Mauerer C and Treves S T 2002 Assessment of malignant pleural mesothelioma with 18F-FDG dual-head gamma-camera coincidence imaging: comparison with histopathology *J. Nucl. Med.* **43** 1144–9
- Golub G H and Von Matt U 1997 Tikhonov regularization for large scale problems *Workshop on Scientific Computing* (Berlin: Springer) pp 3–26
- Grote M J, Kray M and Nahum U 2017 Adaptive eigenspace method for inverse scattering problems in the frequency domain *Inverse Problems* **33** 025006
- Haber E, Ascher U M and Oldenburg D 2000 On optimization techniques for solving nonlinear inverse problems *Inverse Problems* **16** 1263
- Haber E, Horesh L and Tenorio L 2008 Numerical methods for experimental design of large-scale linear ill-posed inverse problems *Inverse Problems* **24** 055012
- Hayashi H, Ochiai T, Mori M, Karube T, Suzuki T, Gunji Y, Hori S, Akutsu N, Matsubara H and Shimada H 2003 Sentinel lymph node mapping for gastric cancer using a dual procedure with dye- and gamma probe-guided techniques *J. Am. Coll. Surgeons* **196** 68–74
- Hellingman D et al 2015 Detecting near-the-injection-site sentinel nodes in head and neck melanomas with a high-resolution portable gamma camera *Clin. Nucl. Med.* **40** e11–6
- Hutchinson M F 1990 A stochastic estimator of the trace of the influence matrix for laplacian smoothing splines *Commun. Stat. - Simul. Comput.* **19** 433–50
- Jaszczak R, Li J, Wang H, Zalutsky M and Coleman R 1994 Pinhole collimation for ultra-high-resolution, small-field-of-view spect *Phys. Med. Biol.* **39** 425
- Ma D, Gulani V, Seiberlich N, Liu K, Sunshine J L, Duerk J L and Griswold M A 2013 Magnetic resonance fingerprinting *Nature* **495** 187–92
- Mandapathil M, Teymoortash A, Heinis J, Wiegand S, Güldner C, Hoch S, Roeßler M and Werner J A 2014 Freehand spect for sentinel lymph node detection in patients with head and neck cancer: first experiences *Acta Oto-Laryngologica* **134** 100–4
- Ozkan E and Eroglu A 2015 The utility of intraoperative handheld gamma camera for detection of sentinel lymph nodes in melanoma *Nucl. Med. Mol. Imaging* **49** 318–20
- Povoski S P, Neff R L, Mojzisek C M, O'Malley D M, Hinkle G H, Hall N C, Murrey D A, Knopp M V and Martin E W 2009 A comprehensive overview of radioguided surgery using gamma detection probe technology *World J. Surgical Oncol.* **7** 11
- Seppi C, Nahum U, von Niederhäusern P A, Pezold S, Rissi M, Haerle S K and Cattin P C 2017 Compressed sensing on multi-pinhole collimator spect camera for sentinel lymph node biopsy *Int. Conf. on Medical Image Computing and Computer-Assisted Intervention* (Berlin: Springer) pp 415–23
- Shoaib T, Soutar D S, MacDonald D G, Camilleri I G, Dunaway D J, Gray H W, McCurrach G M, Bessent R G, MacLeod T I and Robertson A G 2001 The accuracy of head and neck carcinoma sentinel lymph node biopsy in the clinically n0 neck *Cancer* **91** 2077–83
- Stoeckli S J, Steinert H, Pfaltz M and Schmid S 2001 Sentinel lymph node evaluation in squamous cell carcinoma of the head and neck *Otolaryngol. Head Neck Surgery* **125** 221–6

- Sullivan D P, Scharf S C and Komisar A 2001 Intraoperative gamma probe localization of parathyroid adenomas *Laryngoscope* **111** 912–7
- van den Brekel M W, van der Waal I, Meijer C J, Freeman J L, Castelijns J A and Snow G B 1996 The incidence of micrometastases in neck dissection specimens obtained from elective neck dissections *Laryngoscope* **106** 987–91
- Vermeeren L, Olmos R A V, Klop W M C, Balm A J and van den Brekel M W 2010 A portable (γ)-camera for intraoperative detection of sentinel nodes in the head and neck region *J. Nucl. Med.* **51** 700
- von Niederhäusern P A, Maas O C, Rissi M, Schneebeli M, Haerle S and Cattin P C 2016 Augmenting scintigraphy images with pinhole aligned endoscopic cameras: a feasibility study *Int. Conf. on Medical Imaging and Virtual Reality* (Berlin: Springer) pp 175–85
- Warnecke S H, Mattei A, Fuechsel F G, Z' Brun S, Krause T and Studer U E 2007 Detection rate and operating time required for γ probe-guided sentinel lymph node resection after injection of technetium-99m nanocolloid into the prostate with and without preoperative imaging *Eur. Urol.* **52** 126–33
- Zhang L, Eugeni E E, Parthun M R and Freitas M A 2003 Identification of novel histone post-translational modifications by peptide mass fingerprinting *Chromosoma* **112** 77–86

Chapter 4

Joint Inverse Medium and Optimal Control Problem

The main goal of the MIRACLE project is to cut bones with laser light. To improve navigation and avoid cutting sensitive tissue, it is essential to have an accurate feedback system. The first approach was made in the work [67], where they were able to reconstruct the bone's structure and the ablation's position in a 2D simulation using only two transducers. They assumed that the source is precisely known, presupposing, the source's form and frequency composition. However, this cannot be assumed. For example, when ablating with an Er:YAG laser, the acoustic wave may change depending on the kind of tissue and its water content. Hence, we cannot assume that the form and the generated frequencies are known during the ablation process.

This paper investigates the challenge when the source form and the medium surrounding the source are unknown. We can reconstruct the medium velocity and the source by solving the Helmholtz equation with the Adaptive Eigenspace introduced in [63]. Here, we solve the following inverse problem in a 2D simulation: What are the form of the source and the medium velocity for the measured acoustic wave?

There is one major limitation. The computation time was too long for the 2D simulation to be suitable for a real-time application. Furthermore, the number of transducers required is not feasible, and generalizing everything in 3D space is not realistic.

Publication This following paper [65] was published on the 12th of June 2019 in the *PASC '19: Proceedings of the Platform for Advanced Scientific Computing Conference*. We note that Uri Nahum (Postdoc) and Carlo Seppi (Ph.D. Student) are shared authors, that the order of these authors is alphabetical.

Joint Inverse Medium and Optimal Control Problem for Acoustic Waves

Uri Nahum*

Department of Biomedical
Engineering, University of Basel
Allschwil, Switzerland
uri.nahum@unibas.ch

Carlo Seppi*[†]

Department of Biomedical
Engineering, University of Basel
Allschwil, Switzerland
carlo.seppi@unibas.ch

Philippe C. Cattin

Department of Biomedical
Engineering, University of Basel
Allschwil, Switzerland
philippe.cattin@unibas.ch

ABSTRACT

Background: Ever since endoscopes were invented, surgeons try to widen their field of usage by developing novel surgical approaches. An obvious advantage of the endoscope is the minimal invasiveness, but this comes at a price of reduced dexterity, loss of tactile feedback and difficulty in orientation. One of the challenges is to acquire the data of the neighborhood to find the relative position of the endoscope to the surrounding tissues.

Methods & Results: In this paper, we present a mathematical approach to reconstruct unknown source(s) position(s) (e.g. endoscope, which produces a signal in different frequencies) and a medium (e.g. tissue surrounding the endoscope). We solve the joint Inverse Medium and Optimal Control on the Helmholtz equation, where both source(s) and medium velocity are unknown. The use of the Adaptive Eigenspace Inversion (AEI) in combination with frequency stepping, proves itself to be a good solution. We underline our claim, with two-dimensional numerical experiments.

Conclusion: The application of this method together with its promising results can potentially aid to navigate an endoscope through the body while collecting information on the surrounding tissue. These results may also find their application in geophysics.

CCS CONCEPTS

• **Mathematics of computing** → **Partial differential equations; Discrete optimization**; *Discrete mathematics; Nonlinear equations*; Solvers; Numerical differentiation; • **Computing methodologies** → **Optimization algorithms**.

KEYWORDS

Inverse medium problem, unknown source term, optimal control, Helmholtz equation, full waveform inversion, PDE constrained optimization, frequency stepping, multi-parameter problems, Adaptive Eigenspace Inversion.

*Equal Contributor

[†]Corresponding author

Permission to make digital or hard copies of all or part of this work for personal or classroom use is granted without fee provided that copies are not made or distributed for profit or commercial advantage and that copies bear this notice and the full citation on the first page. Copyrights for components of this work owned by others than the author(s) must be honored. Abstracting with credit is permitted. To copy otherwise, or republish, to post on servers or to redistribute to lists, requires prior specific permission and/or a fee. Request permissions from permissions@acm.org.

PASC '19, June 12–14, 2019, Zurich, Switzerland

© 2019 Copyright held by the owner/author(s). Publication rights licensed to ACM.
ACM ISBN 978-1-4503-6770-7/19/06...\$15.00

<https://doi.org/10.1145/3324989.3325718>

ACM Reference Format:

Uri Nahum, Carlo Seppi, and Philippe C. Cattin. 2019. Joint Inverse Medium and Optimal Control Problem for Acoustic Waves. In *Proceedings of the Platform for Advanced Scientific Computing Conference (PASC '19)*, June 12–14, 2019, Zurich, Switzerland. ACM, New York, NY, USA, 9 pages. <https://doi.org/10.1145/3324989.3325718>

1 INTRODUCTION

Minimally invasive surgery reduces the trauma of patients [20, 25]. The method of choice is to insert the endoscopes through small ports into the body. Multiple methods have been introduced to track the position of the endoscope [1, 7, 22–24, 35], but it is also important to know the surrounding tissues, to collect information or to perform a surgery [29]. Here, we have multiple unknown parameters (the surrounding tissue and the position of the endoscope) and hence, we have a joint inverse medium and optimal control problem.

To solve the joint inverse medium and optimal control problem, a multi-parameter inverse problem must be solved, which has been a challenging area of research since more than three decades [38]. In recent years, this problem has been addressed extensively in geophysics [10, 13, 31, 34, 39], e.g. for exploring gas and oil occurrence two distinct parameters are crucial: density and bulk-modulus. This paper deals with a different multi-parameter problem: the two parameters are the unknown medium (e.g. position and wave velocity of the tissue) and the position of the source (e.g. wave sources in the endoscope).

Multi-parameter inverse problems pose various challenges [27]:

- (1) Cross-talk – one of the consequences of optimizing several parameters simultaneously within the same equation manifests itself as unwanted artifacts, resulting from the parameters influencing each other [31]. For instance, when the gradients are coupled regularization problems can occur [33].
- (2) Ill-posedness – in addition, the multi-parameter inverse problem is ill-posed [34], i.e. there is no admissible solution, the solution is not unique or the solution does not depend continuously on the input data.

Different methods have been introduced to address the multi-parameter inverse medium problem. In [34] the full-Newton method and the data-driven strategy are presented. Here, the expected decrease is defined in the misfit functional and combined with a separate Tikhonov (TV) regularization term for each parameter to reduce the Cross-talk between them. Moreover, for the penalty formulation, a sparse version of the Gauss-Newton Hessian is used with prior information of the parameters with respect to the similarity of the

structures [10, 33]. In addition [39] proposed the use of random successive sources (hence, multiple right hand sides) to solve the multi-parameter inversion.

Acoustic waves travel through different tissues with different velocities. Knowledge of these velocity profiles can assist the classification of tissue and structure while the medium velocity is reconstructed. In some cases, the position of the endoscope within the body is unknown. To improve the navigation through the body, not only the velocity profile is important but also the position of the sources. The optimal control problem is then affected by the medium, and hence the resulting combined optimal and inverse medium problem must be solved. The Adaptive Eigenspace (AE) representation of the time-dependent scattering problems, was proposed by [5, 6] and has been extended to a fix frequency for electromagnetic inverse medium problems [5]. It was also used for image processing [28] and strongly relates to nonlinear spectral representation [11]. In [15, 16, 27] the AEI for a single and multi-parameter inverse medium problems was investigated and the eigenspace of the TV regularization gradient was used. The problem was well regularized by slowly increasing the number of eigenfunctions with the time-frequency.

Several approaches have been introduced, where both medium and source are unknown, see for example [12, 29, 32, 36]. In a similar approach to the solution of the multi-parameter inverse problem, which has been introduced in [16], we solve the inverse medium and optimal control problems – where we not only reconstruct the medium velocity (helpful for tissue classification), but also the form and position of the source(s) using the Adaptive Eigenspace Inversion (AEI).

2 THE MEDIUM-CONTROL INVERSE HELMHOLTZ PROBLEM

We begin by introducing the time dependent propagation of a wave through a medium. This can be described with the acoustic wave equation

$$\tilde{y}_{tt}(x, t) - \nabla \cdot (u(x) \nabla \tilde{y}(x, t)) = \tilde{f}(x, t). \quad (1)$$

Herein, $u > 0$ represents the squared medium velocity, \tilde{f} resp. f is the source function, \tilde{y} resp. y the pressure variation – i.e. the wave field – and ω the time-frequency. Using the Fourier transform of the time variable, we write

$$\tilde{y}(x, t) = y(x)e^{-i\omega t} \quad \text{and} \quad \tilde{f}(x, t) = f(x)e^{-i\omega t}. \quad (2)$$

In our simulation, we use unbounded domains. Hence, we need artificial boundaries to mimic the unbounded exterior. One possible approach are perfectly matched layers [4, 17, 37]. Another one is the use of absorbing boundary conditions [2, 3, 9], e.g. Sommerfeld boundary condition. In our case, we use the Sommerfeld boundary condition for the Helmholtz equation:

$$\begin{cases} -\omega^2 y - \nabla \cdot (u \nabla y) = f, & \text{in } \Omega^o = \Omega \setminus \partial\Omega, \\ \frac{\partial y}{\partial \mathbf{n}} -iky = 0, & \text{on } \Gamma = \partial\Omega, \end{cases} \quad (3)$$

where $k(x) = \frac{\omega}{\sqrt{u(x)}}$ is the wave-number at time-frequency ω and

$$\frac{\partial y(x)}{\partial \mathbf{n}} := \mathbf{n} \cdot \nabla y(x)$$

is the normal derivative, where \mathbf{n} denotes the normal on the boundary $\Gamma = \partial\Omega$.

In the following, we introduce the reduced-space approach [14, 18, 21]. This takes advantage of the adjoint and state variables on the control variable u and f , by reducing the search space. The state variable $y = [y_1, \dots, y_{N_s}]$ can be expressed as a function of the squared medium velocity u and the source(s) $f = [f_1, \dots, f_{N_s}]$ (where N_s are the number of sources):

$$y_\ell(u, f) = A(u)^{-1} f_\ell, \quad \text{for } \ell = 1, \dots, N_s. \quad (4)$$

Here, $A(u)$ denotes the forward Helmholtz problem operator in equation (3). By eliminating y_ℓ the optimization problem for the reduced-space approach reads

$$\arg \min_{u, f} \mathcal{F}(u, f), \quad \text{where } \mathcal{F}(u, f) = \frac{1}{2} \sum_{\ell=1}^{N_s} \|\hat{y}_\ell(u, f)\|_2^2 \quad (5)$$

with

$$\begin{aligned} \hat{y}_\ell(u, f) &= y_\ell(u, f) - y_\ell^{obs} \\ &= PA(u)^{-1} f_\ell - y_\ell^{obs}. \end{aligned}$$

The observed pressure variation by the microphones is denoted by $y^{obs} = [y_1^{obs}, \dots, y_{N_s}^{obs}]$ and P projects the computed pressure variation $y_\ell(u, f) = A(u)^{-1} f_\ell$ onto the microphones. The regularization functionals $\mathcal{R}_1(u)$ and $\mathcal{R}_2(f)$ can be added to the misfit functional.

Through the choice of $\mathcal{R}_1(u)$ and $\mathcal{R}_2(f)$, each parameter can be regularized separately according to a priori information on each parameter. Sometimes an additional constraint is added to the optimization [10] to penalize the difference between the structures of two parameters and thus avoid Cross-talk.

We will apply the Adaptive Eigenspace Inversion (AEI), where we can omit the regularization functionals $\mathcal{R}_1(u)$ and $\mathcal{R}_2(f)$, by using the Eigenspace Expansion of u and f (see Sec. 2.1). This will not only improve the reconstruction but also the stability of the reconstruction significantly. For the optimization of the medium u and f , we use the inexact quasi-Newton (Gauss-Newton) method with the Eisenstat-Walker stopping criteria [18, 26, 27] for the internal conjugate gradient (CG) iteration.

2.1 Adaptive Eigenspace (AE) Expansion

We apply the AEI from [15, 16, 27] for the Helmholtz inversion to the joint inverse medium and optimal control problem: in addition to the unknown squared medium velocity u , the sources f are unknown as well. Hence, we use the AE of the squared medium velocity u and of all the sources f_ℓ for $\ell = 1, \dots, N_s$.

As in [16], instead of using a standard nodal basis, such as Finite Difference (FD) or Finite Elements (FE) grid-based discretization, we shall use bases of global eigenfunctions $\{\phi_m\}_{m \geq 1}$ and $\{\varphi_l^f\}_{l \geq 1}$ for each parameter, to represent the squared medium velocity $u(x)$ and the source $f_\ell(x)$ as

$$\begin{aligned} u(x) &\approx u^{AE}(x, \beta) = u_0(x) + \sum_{m=1}^{K_1} \beta_m \phi_m(x), \\ f_\ell(x) &\approx f_\ell^{AE}(x, \gamma) = f_0^\ell(x) + \sum_{l=1}^{K_2} \gamma_l^f \varphi_l^f(x). \end{aligned} \quad (6)$$

In [15], the values of K_1 and K_2 are linearly depend on the time-frequency ω . This reduces the number of unknowns drastically in

comparison to the standard nodal basis approach. Further, we use the eigenspace of the TV regularization gradient

$$\mu(x) = \frac{1}{\sqrt{|\nabla u(x)|^2 + \varepsilon^2}} \quad (7)$$

for the AEI ($\varepsilon > 0$ is a small value, e.g. $\varepsilon = 10^{-6}$). Hence, the eigenfunctions ϕ_m are given by the following eigenspace problem

$$\begin{cases} -\nabla \cdot (\mu(x) \nabla \phi_m(x)) &= \lambda_m \phi_m(x), \quad \forall x \in \Omega^o \\ \phi_m(x) &= 0, \quad \forall x \in \Gamma \end{cases} \quad (8)$$

Following [15], we set the “background” $u_0(x) \in H^1(\Omega)$ as the eigenfunction of the zero eigenvalue with the boundary condition u_∞ on the exterior of u , namely

$$\begin{cases} -\nabla \cdot (\mu(x) \nabla u_0(x)) &= 0, \quad \forall x \in \Omega^o \\ u_0(x) &= u_\infty(x), \quad \forall x \in \Gamma \end{cases} \quad (9)$$

Similarly, we find the eigenfunctions φ_ℓ^f and the “background” f_0^f of the source f_ℓ , by replacing in equation (7), (8), and (9): ∇u , $\nabla \phi_m(x)$, $\phi_m(x)$, ∇u_0 , u_0 , and u_∞ with ∇f_ℓ , $\nabla \varphi_\ell^f(x)$, $\varphi_\ell^f(x)$, ∇f_0^f , f_0^f , and f_∞^f , respectively.

2.2 Adaptive Eigenspace Inversion (AEI) Algorithm

We transform our optimization problem (5) to account for the AEI basis. Instead of using the standard nodal basis, we expand u and f using the AE (see Sec. 2.1). To simplify the algorithm, we only use a single source $f = f_1$ (hence, $f^{AE} = f_1^{AE}$, $f_0 = f_0^1$, $\varphi_l = \varphi_1^1$, $\gamma_l = \gamma_1^1$, and $y^{obs} = y_1^{obs}$). However, it can easily be expanded to multiple sources. Our new reduced-space objective reads

$$\arg \min_{\beta, \gamma} \mathcal{F}(u^{AE}(\beta), f^{AE}(\gamma)), \quad (10)$$

where

$$\mathcal{F}(u^{AE}(\beta), f^{AE}(\gamma)) = \frac{1}{2} \left\| \hat{y}(u^{AE}(\beta), f^{AE}(\gamma)) \right\|_2^2, \quad (11)$$

with

$$\begin{aligned} \hat{y}(u^{AE}(\beta), f^{AE}(\gamma)) &= y(u^{AE}(\beta), f^{AE}(\gamma)) - y^{obs} \\ &= P \left[A(u^{AE}(\beta)) \right]^{-1} f^{AE}(\gamma) - y^{obs}. \end{aligned}$$

We set the gradient of $\mathcal{F}(u^{AE}(\beta), f^{AE}(\gamma))$ as

$$\nabla \mathcal{F} = \begin{bmatrix} \nabla_\beta \mathcal{F} \\ \nabla_\gamma \mathcal{F} \end{bmatrix}, \quad (12)$$

where

$$\begin{aligned} \nabla_\beta \mathcal{F} &= \left[\nabla_\beta u^{AE}(\beta) \right]^\top \nabla_{u^{AE}} \mathcal{F} \\ \nabla_\gamma \mathcal{F} &= \left[\nabla_\gamma f^{AE}(\gamma) \right]^\top \nabla_{f^{AE}} \mathcal{F}, \end{aligned} \quad (13)$$

with

$$\begin{aligned} \nabla_{u^{AE}} \mathcal{F} &= \left(\frac{\partial y(u^{AE}, f^{AE})}{\partial u^{AE}} \right)^\top P^\top \hat{y}(u^{AE}, f^{AE}) \\ \nabla_{f^{AE}} \mathcal{F} &= \left(\frac{\partial y(u^{AE}, f^{AE})}{\partial f^{AE}} \right)^\top P^\top \hat{y}(u^{AE}, f^{AE}) \\ &= \left[A(u^{AE}) \right]^{-\top} P^\top \hat{y}(u^{AE}, f^{AE}). \end{aligned} \quad (14)$$

To minimize the objective function (10), we use conjugate quasi-Newton method, with the Gauss-Newton approximation of the Hessian [18, 26]. We use the Eisenstat-Walker criteria [8] and the safeguards of Nash [30] to terminate the inner CG method.

For this, we need the Jacobi-Matrix \mathcal{J} , hence equation (12) reads

$$\nabla \mathcal{F} = \mathcal{J}^\top \hat{y}(u^{AE}, f^{AE}) \quad (15)$$

where

$$\mathcal{J} = [\mathcal{J}_\beta, \mathcal{J}_\gamma]. \quad (16)$$

From (13) and (14) we deduce

$$\begin{aligned} \mathcal{J}_\beta &= P \left[\frac{\partial y(u^{AE}, f^{AE})}{\partial u^{AE}} \right]^\top \nabla_\beta u^{AE}(\beta) \\ \mathcal{J}_\gamma &= P \left[A(u^{AE}) \right]^{-\top} \nabla_\gamma f^{AE}(\gamma). \end{aligned}$$

Finally, we adapt the inexact Newton algorithm of [16] in Algorithm 1 so that we can apply AEI for the joint problem. We note that we do not store the full Jacobi-Matrix, rather all the operations can be reduced to Matrix-Vector multiplication [18]. This is essential for the success of the inversion. Further, we use frequency stepping: starting at ω_1 and slowly increase the frequency up to ω_N .

3 CROSS-TALK

Cross-talk between the squared medium velocity u and the source(s) f can cause undesired artifacts. In this section, we visualize the challenges of Cross-talk, with the help of two numerical examples. To simplify these examples, we assume that we have Gaussian sources $\tilde{f}(x, \tilde{x}) = (\tilde{f}_1, \dots, \tilde{f}_{N_s})$ with the centers at $\tilde{x} = (\tilde{x}^1, \dots, \tilde{x}^{N_s})^\top$. Since the form of the sources are known, we can write the reduced-space approach as follow:

$$\arg \min_{u, \tilde{x}} \mathcal{F}(u, \tilde{f}), \quad \text{where } \mathcal{F}(u, \tilde{f}) = \frac{1}{2} \sum_{\ell=1}^{N_s} \left\| \hat{y}_\ell(u, \tilde{f}) \right\|_2^2 \quad (17)$$

with

$$\begin{aligned} \hat{y}_\ell(u, \tilde{f}) &= y_\ell(u, \tilde{f}) - y_\ell^{obs} \\ &= PA(u)^{-1} \tilde{f}_\ell - y_\ell^{obs}. \end{aligned}$$

3.1 The Gradients of the Multi-Parameter Inverse Problem

In the following, we are investigating the reduced-space gradient of two examples and we do not optimize or reconstruct either example.

```

input :
• initial guess for squared medium velocity  $u$ 
• initial guess for source  $f$ 
• observed pressure variation  $y^{obs}$ 

output:
• computed squared medium velocity  $u$  and source  $f$ 

1 for  $\omega \leftarrow \omega_1, \dots, \omega_N$  do
2   // Adaptive Eigenspace Expansion of  $u$  and  $f$ , see (6);
3   Choose number of eigenfunctions  $K_1$  and  $K_2$ ;
4    $u^{AE} \leftarrow u_0 + \sum_{m=1}^{K_1} \beta_m \phi_m$ ;
5    $f^{AE} \leftarrow f_0 + \sum_{l=1}^{K_2} \gamma_l \varphi_l$ ;
6   // Optimize;
7   while  $\|\nabla \mathcal{F}\|_2 < \text{tolerance}$  do
8     Update  $A(u^{AE})$ ;
9     Update Jacobi-Matrix  $\mathcal{J}$ ;
10    Update  $\nabla \mathcal{F}$ ;
11    // Solve conjugate quasi-Newton (GN);
12    solve  $\mathcal{J}^T \mathcal{J} p = -\nabla \mathcal{F}$  for  $p$ ;
13    //  $p$  is divided for updating  $\beta$  and  $\gamma$ ;
14     $\begin{bmatrix} p_\beta \\ p_\gamma \end{bmatrix} \leftarrow p$ 
15    find step-size  $\alpha$  using Armijo backtracking;
16    // update  $\beta$  and  $\gamma$ ;
17     $\beta \leftarrow \beta + \alpha p_\beta$ ;
18     $\gamma \leftarrow \gamma + \alpha p_\gamma$ ;
19    // update  $u^{AE}$  and  $f^{AE}$  with the new  $\beta$  and  $\gamma$ ;
20     $u^{AE} \leftarrow u_0 + \sum_{m=1}^{K_1} \beta_m \phi_m$ ;
21     $f^{AE} \leftarrow f_0 + \sum_{l=1}^{K_2} \gamma_l \varphi_l$ ;
22  end
23  Update  $u$  and  $f$ ;
24   $u \leftarrow u^{AE}$ ;
25   $f \leftarrow f^{AE}$ ;
26 end
27 return  $u$  and  $f$ ;

```

Algorithm 1: Adaptive Eigenspace Inversion (AEI) using Adaptive Eigenspace (AE) Expansion and inexact quasi-Newton using the Gauss-Newton (GN) approximation of the Hessian and frequency stepping to solve equation (10).

Similar to (14) the multi-parameter gradients are coupled and are given in the directions of u and \tilde{x} as

$$\nabla_u \mathcal{F}(u, \tilde{f}) = \sum_{\ell=1}^{N_s} \left(\frac{\partial y_\ell(u, \tilde{f})}{\partial u} \right)^T P^T \hat{y}_\ell(u) \quad (18)$$

and

$$\begin{aligned} \nabla_{\tilde{x}} \mathcal{F}(u, \tilde{f}) &= \left(\nabla_{\tilde{x}} \tilde{f}_\ell \right)^T \nabla_{\tilde{f}_\ell} \mathcal{F}(u, \tilde{f}) \\ &= \left(\nabla_{\tilde{x}} \tilde{f}_\ell \right)^T \left(\frac{\partial y_\ell(u, \tilde{f})}{\partial \tilde{f}_\ell} \right)^T P^T \hat{y}_\ell(u, \tilde{f}) \quad (19) \\ &= \left(\nabla_{\tilde{x}} \tilde{f}_\ell \right)^T [A(u)]^{-T} P^T \hat{y}_\ell(u, \tilde{f}). \end{aligned}$$

If u and \tilde{x} are set to the true value, the gradients will read

$$\begin{aligned} \nabla_u \mathcal{F}(u, \tilde{f})|_{u=u^{true}, \tilde{x}=\tilde{x}^{true}} &= 0 \\ \nabla_{\tilde{x}} \mathcal{F}(u, \tilde{f})|_{u=u^{true}, \tilde{x}=\tilde{x}^{true}} &= 0. \end{aligned}$$

for $\ell = 1, \dots, N_s$. However, the parameters appear in both gradients, hence, a small change in one parameter can influence the gradient of the other [33]. In our case, it causes a non-zero gradient for both, even if one of the parameters already equals the true value.

We chose two slightly different examples to illustrate the issue of coupled gradients for the joint medium-control inverse problem. Both examples are chosen, such that one parameter is set to the true value while the other parameter is very close to the true value. In the first example, we modify the variable u slightly and assume, that we have a single source $\tilde{f} = \tilde{f}_1$ at the true position $\tilde{x} = \tilde{x}^1$. In the second example, we make a small modification to the position \tilde{x} of the source \tilde{f} and fix the parameter u at the true solution. Unlike when the gradients are independent – zero gradient in the direction of this parameter and non-zero gradient in the other – our gradient will be nonzero in both directions. Thus, we show that the squared medium velocity u and the source \tilde{f} perturb each others gradient.

3.2 Numerical Examples for Cross-talk

Similar to [27], we visualize the Cross-talk between the squared medium velocity u and the source \tilde{f} . For this, we consider the following setup for the reduced-space gradient, we use

- a two-dimensional bounded region $\Omega = [0, 1] \times [0, 1]$,
- a Gaussian source $\tilde{f}(x, \tilde{x}) = \exp\left(-\frac{(x_1 - \tilde{x}_1)^2 + (x_2 - \tilde{x}_2)^2}{2R^2}\right)$ centered at $\tilde{x} = (\tilde{x}_1, \tilde{x}_2)$, where $x = (x_1, x_2) \in \Omega$ are the horizontal and vertical directions, respectively. Further, we use \tilde{f} instead of f for the Helmholtz equation (3).
- the time-frequency $\omega = 8$,
- and a second order staggered FD method to discretize u and \tilde{f} onto a 200×200 Cartesian grid.

In Fig. 1 we present a two-parameter profile in Ω . The squared medium velocity u is chosen as a piece-wise constant inside a circle \mathcal{O} centered at $x = (0.5, 0.5)$ with a radius of 0.1 and we set the true values of the parameter u and the true position of the source $\tilde{x} = (\tilde{x}_1, \tilde{x}_2)$ as follows:

$$u(x) = \begin{cases} 1.2 & x \in \mathcal{O} \\ 1 & x \in \Omega \setminus \mathcal{O} \end{cases}, \quad \tilde{x} = (0.5, 0.8). \quad (20)$$

The profile u and the wave initiated by \tilde{f} at \tilde{x} with the time-frequency $\omega = 8$ are illustrated in Fig. 1.

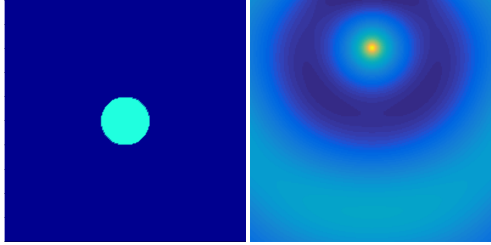


Figure 1: The true value of the squared medium velocity u (left) and the real part of the wave initiated at $\tilde{x} = (0.5, 0.8)$ propagating through the medium (right).

3.2.1 *Example 1:* For the initial guess, we slightly perturb the true value of u inside \mathcal{O} by 0.01 but keep the position of \tilde{f} at the true value:

$$u(x) = \begin{cases} 1.19 & x \in \mathcal{O} \\ 1 & x \in \Omega \setminus \mathcal{O} \end{cases}, \quad \tilde{x} = (0.5, 0.8) \quad (21)$$

On the left side of Fig. 2 we show the gradients for u and \tilde{x} . We note that both gradients are non-zero, although the source position \tilde{x} (and the source \tilde{f}) are equal to the true value.

3.2.2 *Example 2:* For the second example, we slightly change the true position of \tilde{x} :

$$u(x) = \begin{cases} 1.2 & x \in \mathcal{O} \\ 1 & x \in \Omega \setminus \mathcal{O} \end{cases}, \quad \tilde{x} = (0.49, 0.8), \quad (22)$$

in particular, we shift the \tilde{x}_1 position of the source for 0.01 and keep the vertical position \tilde{x}_2 and the parameter u unchanged.

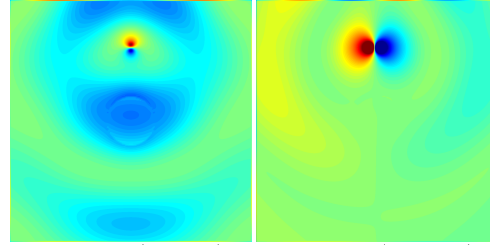
On the right side of Fig. 2 we show the gradients for u and \tilde{x} . Again, both gradients are non-zero although the squared medium velocity u is set to the true value.

3.2.3 *The Reduced Gradient:* In both examples, we get a non-zero gradient for all the parameters, even if we set one parameter to the optimal value and only perturb the other parameters slightly. However, a zero gradient at the optimal value of any parameter is essential for successful optimization.

In both examples shown in Fig. 2, a small modification in one parameter causes perturbations in the other parameter's gradient. This illustrates the Cross-talk between the parameters and the ill-posedness of the problem. We may have regularization problems and the gradients with an initial guess close to the true profile may point in a direction of a false solution.

4 NUMERICAL EXAMPLES

In the following, we show the challenges of the Cross-talk in the joint inverse medium and optimal control problem. Further, we propose the AE shown in Sec. 2.1 as a possible solution. We give three examples: in two examples the form of the source(s) are unknown, and one when the form of the sources are known.



$$\nabla_{\tilde{x}} \mathcal{F}(u, \tilde{f}) = \begin{pmatrix} -0.197 \\ 0.0002 \end{pmatrix} \quad \nabla_{\tilde{x}} \mathcal{F}(u, \tilde{f}) = \begin{pmatrix} -0.0001 \\ 0.7811 \end{pmatrix}$$

Figure 2: Reduced gradient $\mathcal{F}(u, \tilde{f})$ for the profile (20): the two images visualize $\nabla_u \mathcal{F}(u, \tilde{f})$ and beneath them we show the computed $\nabla_{\tilde{x}} \mathcal{F}(u, \tilde{f})$. Left: first example with the initial guess (21). Right: second example with the initial guess (22).

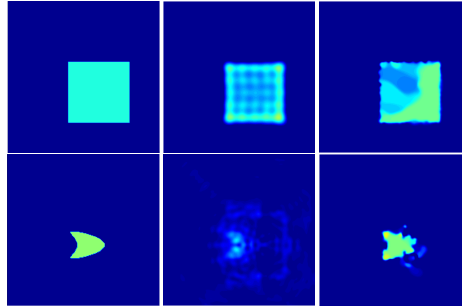


Figure 3: Top: source f . Bottom: squared medium velocity u . From left to right: True parameters u and f ; illustrating Cross-talk using inexact Newton method; Adaptive Eigenspace Inversion (AEI) reduces Cross-talk.

4.1 Unknown Form of the Source

On the left side of Fig. 3, we show the target profiles of the source f (top) and for the squared medium velocity u (bottom). The parameters u and f are given by

$$u(x) = \begin{cases} 1.5 & x \in \mathcal{D} \\ 1 & x \in \Omega \setminus \mathcal{D} \end{cases} \quad f(x) = \begin{cases} 0.4 & x \in \mathcal{Q} \\ 0 & x \in \Omega \setminus \mathcal{Q} \end{cases}, \quad (23)$$

where \mathcal{D} is a kite shaped object and \mathcal{Q} is a square with a side length of 0.4 centered at $(0.45, 0.4)$. To reconstruct the squared medium velocity u and the form of the source f , we consider the Helmholtz equation (3) in the unit square $\Omega = [0, 1] \times [0, 1]$. The wave field y and the control variables u and f are discretized using second order FD.

We first illustrate the challenges of Cross-talk in the joint inverse medium and optimal control problem and apply the AEI to overcome them.

4.1.1 Nodal-Basis. To illustrate the challenges of Cross-talk, we use the nodal basis approach to reconstruct the squared medium velocity u and the source f . We apply the inexact Newton (quasi-Newton) method using the Gauss-Newton approximation of the Hessian and frequency stepping at $\omega = 8, 10, \dots, 78, 80$.

The reconstructed u and f for the nodal basis approach are shown in the middle column of Fig. 3. Both shapes of \mathcal{D} and \mathcal{Q} are reconstructed, but the values inside the shapes are poorly deduced. On the bottom – at the reconstructed squared medium velocity u – we see a trace of the source shaped structure, i.e. an undesired Cross-talk between the source f and the squared medium velocity u . The relative L^2 -error of u , defined by

$$\frac{\|u^{\text{true}} - u\|_2}{\|u^{\text{true}}\|_2},$$

is 6.93%. The from of the source f holds a relative error, defined by

$$\frac{\|f^{\text{true}} - f\|_2}{\|f^{\text{true}}\|_2},$$

of 56.91%.

4.1.2 Adaptive Eigenspace Inversion (AEI). We apply the AEI approach for multi-parameter inverse problems [16] to tackle the Cross-talk. This time we use the AE for u and f (see Sec. 2.1) to solve the previous example. We solve equation (10) and use Algorithm 1 for the same observations as for the nodal basis at the same time-frequencies. On the right side of Fig. 3 we see, that the AE reduces Cross-talk and improves reconstruction of the squared medium velocity u . The results of the AE approach reduces the relative L^2 -error of u to 3.03% and f is reduced to 40.17%. Still, the problem is severely ill-posed and the reconstruction here is not perfect, but the improvement with respect to the nodal basis is clear.

4.2 Unknown positions of the Sources

Now, we assume that we have multiple Gaussian sources with unknown positions. The true squared medium velocity u is composed of three layers and a kite-shaped obstacle \mathcal{D} on the middle layer. For $x = (x_1, x_2) \in \Omega$ we have

$$u(x) = \begin{cases} 3 & x \in \mathcal{D} \\ 2.5 & 0.1 < x_2 \leq 0.3 \\ 2 & 0.3 < x_2 \leq 0.5 \quad \& \quad x \notin \mathcal{D} \\ 1.5 & 0.5 < x_2 \leq 0.9 \\ 1 & \text{else} \end{cases}$$

and for the Gaussian sources $\tilde{f} = [\tilde{f}_1, \tilde{f}_2, \tilde{f}_3]$. We consider three sources at the time-frequencies $\omega = 8, 10, \dots, 118, 120$ initiated in

$$\tilde{x}^{\text{true}} = \begin{pmatrix} 0.2, 0.8 \\ 0.5, 0.8 \\ 0.7, 0.8 \end{pmatrix},$$

see left of Fig. 4. The wave field y and the variables u and \tilde{f} are discretized with second order FD (200×200 equidistant grid for \tilde{f} and y and y^{obs} on a finer non-coupled grid). The initial guess for u is $u = 1$ everywhere in Ω^p . Further, we assume that u is known on the boundary Γ ($u_{\infty}(x)$ is known in equation (9)) and since only the positions but not the form of the sources are unknown, we

just need to provide an initial value for \tilde{x} . For all three sources we choose the center of the domain:

$$\tilde{x} = \begin{pmatrix} 0.5, 0.5 \\ 0.5, 0.5 \\ 0.5, 0.5 \end{pmatrix}. \quad (24)$$

4.2.1 Nodal basis approach. We apply the nodal basis approach using the inexact Newton (quasi-Newton) method, to solve (17). The position of one of the sources was converging to a wrong position. Since this problem is severely ill-posed, a change in the initial guess can assist in finding the solution. Accordingly, we change the initial guess of the first source to $(0.5, 0.6)$, instead of $(0.5, 0.5)$:

$$\tilde{x} = \begin{pmatrix} 0.5, 0.6 \\ 0.5, 0.5 \\ 0.5, 0.5 \end{pmatrix}.$$

Now, all three sources are found with a small relative L^2 -error, defined by

$$\frac{\|\tilde{x}^{\text{true}} - \tilde{x}\|_2}{\|\tilde{x}^{\text{true}}\|_2},$$

of 0.1%. The squared medium velocity u was reconstructed with a relative L^2 -error close to 20%. Artifacts of the sources can be seen in the reconstruction of the medium velocity. Additionally, the bottom layer is poorly reconstructed.

4.2.2 Adaptive Eigenspace Inversion (AEI). Similar to (10) and (17) the reduced-space objective reads

$$\arg \min_{\beta, \tilde{x}} \mathcal{F}(u^{AE}(\beta), \tilde{f}(\tilde{x})) \quad (25)$$

with

$$\mathcal{F}(u^{AE}(\beta), \tilde{f}(\tilde{x})) = \frac{1}{2} \sum_{\ell=1}^{N_s} \|\hat{y}_{\ell}(u^{AE}(\beta), \tilde{f}(\tilde{x}))\|_2^2,$$

for $\ell = 1, \dots, N_s$ and $N_s = 3$ the number of sources. The method is very similar to the one described in Sec. 2.2, however, we only apply the AE on $u(x)$. We define

$$\nabla \mathcal{F} = \begin{bmatrix} \nabla_{\beta} \mathcal{F} \\ \nabla_{\tilde{x}} \mathcal{F} \end{bmatrix}, \quad (26)$$

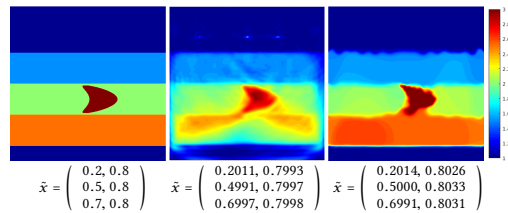


Figure 4: Left to right: the true value of the squared medium velocity u (top) and source positions \tilde{x} of \tilde{f} (bottom); Reconstructed parameters u (top) and \tilde{x} (bottom) by solving equation (17); Adaptive Eigenspace Inversion (AEI) to solve equation (25), thus avoiding Cross-talk.

where similar to (19) we have

$$\nabla_{\tilde{x}^\ell} \mathcal{F}(u^{AE}, \tilde{f}) = \left(\nabla_{\tilde{x}^\ell} \tilde{f} \right)^\top \left[A(u^{AE}) \right]^{-\top} P^\top \hat{y}_\ell(u^{AE}, \tilde{f}), \quad (27)$$

and we use

$$\tilde{x} = \begin{pmatrix} \tilde{x}^1 \\ \vdots \\ \tilde{x}^{N_s} \end{pmatrix} \quad \text{and} \quad \nabla_{\tilde{x}} \mathcal{F} = \begin{pmatrix} \nabla_{\tilde{x}^1} \mathcal{F}(u^{AE}, \tilde{f}_1) \\ \vdots \\ \nabla_{\tilde{x}^{N_s}} \mathcal{F}(u^{AE}, \tilde{f}_{N_s}) \end{pmatrix}. \quad (28)$$

With a small modification of Algorithm 1 (increasing the number of sources and solving (25) instead of (10)), we are able to reconstruct the parameters u and \tilde{x} using the initial guess (24).

The reconstructed u and \tilde{x} are shown on the right of Fig. 4. We see, that the position of the sources are reconstructed with the small relative L^2 -error of 0.34%. Further, all three layers combined with the kite-shaped obstacle \mathcal{D} are fully reconstructed. The relative L^2 -error for u is 6.28%, which is about three times smaller in comparison with the nodal approach.

4.3 Unknown Form of Multiple Sources

In this example, we have two unknown forms of the sources. Here, we apply the FE method (the success of the AE is not dependent in the underlying discretization [15]). First, we reconstruct the medium and the sources using a linearly increasing number of eigenfunctions (K_1 and K_2) dependent in the time-frequency ω . We tested different number of eigenfunction and show an example where we have an improvement of the reconstruction using different strategy. This shows that further research in the automation of choosing the number of eigenfunction must be done.

We extend the reduce space approach of (10) to multiple sources:

$$\mathcal{F}(u^{AE}(\beta), f^{AE}(y)) = \frac{1}{2} \sum_{\ell=1}^{N_s} \left\| \hat{y}_\ell(u^{AE}(\beta), f^{AE}(y)) \right\|_2^2, \quad (29)$$

with

$$\begin{aligned} \hat{y}_\ell(u^{AE}(\beta), f^{AE}(y)) &= y_\ell(u^{AE}(\beta), f^{AE}(y)) - y_\ell^{obs} \\ &= P \left[A(u^{AE}(\beta)) \right]^{-1} f_\ell^{AE}(y) - y_\ell^{obs}. \end{aligned}$$

We have a bounded region on $\Omega = [0, 1] \times [0, 1]$ and apply the AE of the squared medium velocity u and the sources f . Here, we use the FE approach on \mathcal{P}^1 elements (piece-wise linear continuous elements). Algorithm 1 is then computed with *Freefem* [19] as well as the FE approach of the Helmholtz equation. In this Example, the values on the boundary $\Gamma = \partial\Omega$ are known and the microphones are placed on it. Hence, $u = u_\infty$ and $y^{obs} = (y_1^{obs}, \dots, y_{N_s}^{obs})$ is defined on $\Gamma = \partial\Omega$.

On the top of Fig. 5 we have the true parameters of u and $f = (f_1, f_2)$. The true squared medium velocity u has a layer \mathcal{L} and on it an ellipse \mathcal{E} . The two squares sources (\mathcal{S}_1 and \mathcal{S}_2) are centered at $(0.75, 0.75)$ and $(0.35, 0.75)$ with a side length of 0.2. Hence, the parameters u and f are given by

$$u(x) = \begin{cases} \frac{3}{2} & x \in \mathcal{L} \\ 2 & x \in \mathcal{E} \\ 1 & \text{else} \end{cases}, \quad f_1(x) = \begin{cases} \frac{1}{2} & x \in \mathcal{S}_1 \\ 0 & \text{else} \end{cases}, \quad f_2(x) = \begin{cases} 1 & x \in \mathcal{S}_2 \\ 0 & \text{else} \end{cases}.$$

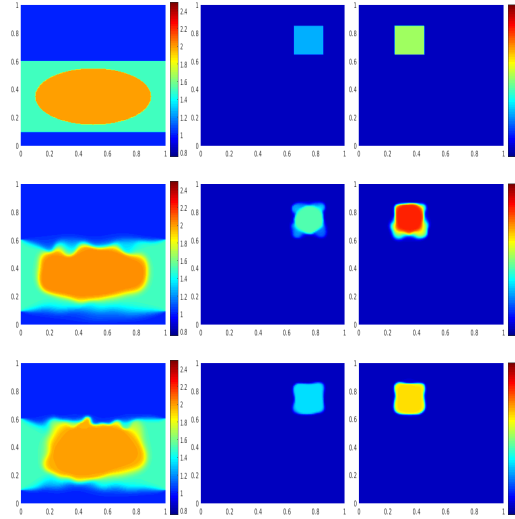


Figure 5: Left to right: squared medium velocity u , source f_1 and source f_2 . From top to bottom: True parameters of u and $f = (f_1, f_2)$; reconstruction using AEI with $K_1 = K_2 = \omega$; reconstruction with $K_1 = \omega$ and $K_2 = 10$.

4.3.1 Adaptive Eigenspace Inversion (AEI). With a small modification of Algorithm 1, we solve (10) for multiple sources using (29). We computed the algorithm on an *Intel(R) Xeon(R) CPU E5-2680 v4 @ 2.40GHz* CPU with the initial guess $u = 1$ and $f = 0$ with frequency stepping at $\omega = 8, 10, \dots, 48, 50$ on a grid with 101×101 points.

First, we solve the AEI with linear dependency of the eigenfunctions

$$K_1 = \omega \quad \text{and} \quad K_2 = \omega,$$

similar to [15, 16]. We get a good reconstruction for the squared medium velocity u , with a relative L^2 -error of 7.92% (Fig. 6), but the amplitude of the sources are poorly deduce (see middle of Fig.5). The relative error of the sources f_1 and f_2 are 64% and 70%, respectively (see Fig. 6).

We can improve the reconstruction of the sources f by choosing a constant number of eigenfunction for the sources (see last row of Fig. 5):

$$K_1 = \omega \quad \text{and} \quad K_2 = 10.$$

The relative L^2 -error of the squared medium velocity increased slightly, with 8.82%. However, the relative L^2 -error of the sources improved drastically: f_1 and f_2 have an error of 31% and 34%, respectively. In addition, we save computational cost for the AE approach, as we compute less eigenfunctions at each time-frequency (see Fig. 6).

Here we see, that the choice of the number of eigenfunctions is critical for the success of the reconstruction. Further, we note

PASC '19, June 12–14, 2019, Zurich, Switzerland

Nahum and Seppi, et al.

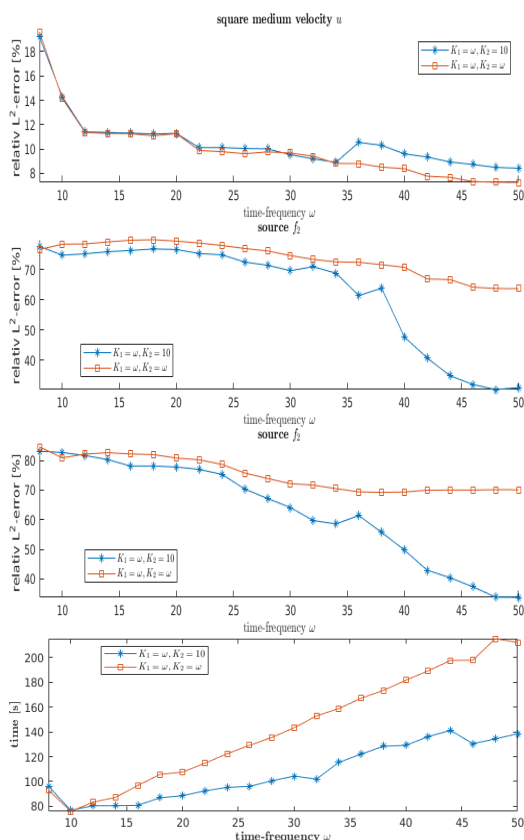


Figure 6: Comparison of different numbers of eigenfunctions (K_1 for u , K_2 for f_1 and f_2) in the Adaptive Eigenspace (AE) expansion. From top to bottom: relative L^2 -error of u , f_1 and f_2 . Computation time for the AE Expansion of the squared medium velocity u and the sources $f = (f_1, f_2)$ for each time-frequency ω .

that finding an optimal number of eigenfunctions will improve the results. This may save computational time by computing a smaller number of eigenfunctions and by reducing dramatically the search space of the optimization.

5 CONCLUSION & DISCUSSION

We show in this paper the challenges that Cross-talk and ill-posedness bring in to the Helmholtz inversion when the source(s) f and the squared medium velocity u are unknown. Further, we apply the Adaptive Eigenspace Inversion (AEI) method for the joint inverse medium and optimal control problem and show in numerical experiments that this method can reduce these challenges. Although

we have an improvement of the Cross-talk with the Adaptive Eigenspace (AE) in comparison to the nodal presentation, the joint inverse medium and optimal control problem is severely ill-posed and a small change in the parameters might change the solution. Hence, an extended investigation for the optimal number of basis functions in the AE and further parameters has to be done.

We believe that this AEI approach will not only be a valuable contribution in medical applications, but also in geophysics. In the future, we plan to parallelize the Helmholtz inversion and investigate the challenges of Cross-talk on large scale modules and in three space dimensions. Further, we would like to attach several acoustic sources to an endoscope, and use this approach to collect information of its surrounding tissues and finding its exact position in the body.

ACKNOWLEDGMENTS

The authors thank Marcus J. Grote and Jet H. Tang for useful discussions.

REFERENCES

- [1] Matthias Baumhauer, Marco Feuerstein, Hans-Peter Meinzer, and J Rassweiler. 2008. Navigation in endoscopic soft tissue surgery: perspectives and limitations. *Journal of endourology* 22, 4 (2008), 751–766.
- [2] Alvin Bayliss, Max Gunzburger, and Eli Turkel. 1982. Boundary conditions for the numerical solution of elliptic equations in exterior regions. *SIAM J. Appl. Math.* 42, 2 (1982), 430–451.
- [3] Alvin Bayliss and Eli Turkel. 1980. Radiation boundary conditions for wave-like equations. *Comm. Pure Appl. Math.* 33, 6 (1980), 707–725. <https://doi.org/DOI:10.1002/cpa.3160330603>
- [4] J.-P. Berenger. 1994. A Perfectly Matched Layer for the Absorption of Electromagnetic Waves. *J. Comput. Phys.* 114 (Oct. 1994), 185–200. <https://doi.org/10.1006/jcph.1994.1159>
- [5] Maya de Buhan and Marie Kray. 2013. A new approach to solve the inverse scattering problem for waves: combining the TRAC and the Adaptive Inversion methods. *Inverse Problems* 29, 8 (2013), 085009. <https://doi.org/doi:10.1088/0266-5611/29/8/085009>
- [6] Maya de Buhan and Axel Osses. 2009. A stability result in parameter estimation of the 3D viscoelasticity system. *C. R. Acad. Sci. Paris Ser. I* 347 (2009), 1373–1378.
- [7] Daisuke Deguchi, Kensaku Mori, Yasuhito Suenaga, Jun-ichi Hasegawa, Junichiro Toriwaki, Hiroshi Natori, and Hirotsugu Takabatake. 2003. New calculation method of image similarity for endoscope tracking based on image registration in endoscope navigation. In *International Congress Series*, Vol. 1256. Elsevier, 460–466.
- [8] Stanley C. Eisenstat and Homer F. Walker. 1996. Choosing the forcing terms in an inexact Newton method. *SIAM J. Sci. Comput.* 17, 1 (1996), 16–32. <https://doi.org/DOI:10.1137/0917003>
- [9] Björn Engquist and Andrew J. Majda. 1977. Absorbing boundary conditions for the numerical simulation of waves. *Math. Comp.* 31, 139 (1977), 629–651.
- [10] A. Luis Gallardo and Meju A. Max. 2004. Joint Two-Dimensional DC Resistivity and Seismic Travel Time Inversion with Cross-Gradients Constraints. *Journal of Geophysical Research* 109, B3 (2004). <https://doi.org/10.1029/2003JB002716>
- [11] Guy Gilboa, Michael Moeller, and Martin Burger. 2016. Nonlinear spectral analysis via one-homogeneous functionals: Overview and future prospects. *Journal of Mathematical Imaging and Vision* 56, 2 (2016), 300–319.
- [12] Marie Graff, Marcus Grote, Frédéric Nataf, and Franck Assous. 2019. How to solve inverse scattering problems without knowing the source term: a three-step strategy. (2019).
- [13] Marcus Grote, Frédéric Nataf, Jet Hoe Tang, and Pierre-Henri Tournier. 2019. Parallel Controllability Methods For the Helmholtz Equation. (2019).
- [14] Marcus J. Grote, Johannes Huber, Drosos Kourounis, and Olaf Schenk. 2014. Inexact Interior-Point Method for PDE-Constrained Nonlinear Optimization. *SIAM J. Sci. Comp.* 36, 3 (2014), A1251–A1276. <https://doi.org/DOI:10.1137/13091283>
- [15] Marcus J Grote, Marie Kray, and Uri Nahum. 2017. Adaptive eigenspace method for inverse scattering problems in the frequency domain. *Inverse Problems* 33, 2 (2017), 025006. <http://stacks.iop.org/0266-5611/33/i=2/a=025006>
- [16] Marcus J Grote and Uri Nahum. 2019. Adaptive eigenspace for multi-parameter inverse scattering problems. *Computers & Mathematics with Applications* (2019).
- [17] Marcus J Grote and Imbo Sim. 2009. Perfectly matched layer for the second-order wave equation. In *Waves* 09, 370–371.

- [18] Eldad Haber, Uri M. Ascher, and Doug Oldenburg. 2000. On optimization techniques for solving nonlinear inverse problems. *Inverse Problems* 16 (2000), 1263. Issue 5. <https://doi.org/DOI:10.1088/0266-5611/16/5/309>
- [19] F. Hecht. 2012. New development in FreeFem++. *J. Numer. Math.* 20, 3-4 (2012), 251–265.
- [20] Jim C Hu, Xiangmei Gu, Stuart R Lipsitz, Michael J Barry, Anthony V D'Amico, Aaron C Weinberg, and Nancy L Keating. 2009. Comparative effectiveness of minimally invasive vs open radical prostatectomy. *Jama* 302, 14 (2009), 1557–1564.
- [21] Johannes Huber. 2013. *Interior-Point Methods for PDE-Constrained Optimization*. Ph.D. Dissertation. University of Basel.
- [22] Lorenzo Iafolla, Lilian Witthauer, Azhar Zam, Georg Rauter, and Philippe Claude Cattin. 2018. Proof of principle of a novel angular sensor concept for tracking systems. *Sensors and Actuators A: Physical* 280 (2018), 390–398.
- [23] Takakazu Kawamata, Hiroshi Iseki, Takao Shibusaki, and Tomokatsu Hori. 2002. Endoscopic augmented reality navigation system for endonasal transsphenoidal surgery to treat pituitary tumors. *Neurosurgery* 50, 6 (2002), 1393–1397.
- [24] R Lapeer, MS Chen, G Gonzalez, A Linney, and G Alusi. 2008. Image-enhanced surgical navigation for endoscopic sinus surgery: evaluating calibration, registration and tracking. *The International Journal of Medical Robotics and Computer Assisted Surgery* 4, 1 (2008), 32–45.
- [25] James D Luketich, Miguel Alvelo-Rivera, Percival O Buenaventura, Neil A Christie, James S McCaughan, Virginia R Litle, Philip R Schauer, John M Close, and Hiran C Fernando. 2003. Minimally invasive esophagectomy: outcomes in 222 patients. *Annals of surgery* 238, 4 (2003), 486.
- [26] Ludovic Métivier, Romain Brossier, Jean Virieux, and Stéphane Operto. 2013. Full Waveform Inversion and the Truncated Newton Method. *SIAM J. Sci. Comput.* 35, 2 (2013), B401–B437. <https://doi.org/DOI:10.1137/120877854>
- [27] Uri Nahum. 2016. *Adaptive eigenspace for inverse problems in the frequency domain*. Ph.D. Dissertation. University of Basel.
- [28] Uri Nahum and Philippe C. Cattin. 2018. Adaptive Eigenspace Segmentation. *arXiv e-prints*, Article arXiv:1810.12771 (Oct 2018), arXiv:1810.12771 pages. [arXiv:math.NA/1810.12771](https://arxiv.org/abs/1810.12771)
- [29] Uri Nahum, Azhar Zam, and Philippe C Cattin. 2018. Bone reconstruction and depth control during laser ablation. In *International Workshop on Computational Methods and Clinical Applications in Musculoskeletal Imaging*. Springer, 126–135.
- [30] Stephen G. Nash. 2000. A survey of truncated-Newton methods. *J. Comput. Appl. Math.* 124, 1-2 (2000), 45–59. [https://doi.org/DOI:10.1016/S0377-0427\(00\)00426-X](https://doi.org/DOI:10.1016/S0377-0427(00)00426-X)
- [31] Weynyong Pan and Kris Innanen. 2016. Suppress Parameter Cross-talk for Elastic Full-waveform Inversion: Parametrization and Acquisition Geometry. *GeoConvention* (2016).
- [32] Mathieu Pernot, Gabriel Montaldo, Mickael Tanter, and Mathias Fink. 2006. "Ultra-sonic stars" for time-reversal focusing using induced cavitation bubbles. *Applied physics letters* 88, 3 (2006), 034102.
- [33] Bas Peters and Felix J. Hermann. 2014. A Sparse Reduced Hessian Approximation for Multi-Parameter Wavefield Reconstruction Inversion. *SEG Denver Annual Meeting* (2014).
- [34] Vincent Prieux, Romain Brossier, Stéphane Operto, and Jean Virieux. 2013. Multiparameter full waveform inversion of multicomponent Ocean-Bottom-Cable data from Valhall field. Part 1: imaging compressional wave speed, density and attenuation. *Geophys. J. Int.* 194, 3 (2013), 1640–1664. <https://doi.org/DOI:10.1093/gji/ggt177>
- [35] Samaneh Manavi Roodsari, Lilian Witthauer, Lorenzo Iafolla, Georg Rauter, Azhar Zam, and Philippe C Cattin. 2018. Temperature-compensated FBG-based 3D shape sensor using single-mode fibers. In *Specialty Optical Fibers*. Optical Society of America, JTu6C-1.
- [36] T Saratoon, T Tarvainen, BT Cox, and SR Arridge. 2013. A gradient-based method for quantitative photoacoustic tomography using the radiative transfer equation. *Inverse Problems* 29, 7 (2013), 075006.
- [37] I Singer and E Turkel. 2004. A perfectly matched layer for the Helmholtz equation in a semi-infinite strip. *J. Comput. Phys.* 201, 2 (2004), 439–465.
- [38] Albert Tarantola. 1984. Inversion of Seismic Reflection Data in the Acoustic Approximation. *Geophysics* 49, 8 (1984), 1259–1266.
- [39] Chao Wang, David Yingest, John Brittan, and Jacques Leveille. 2014. Fast Multi-Parameter Anisotropic Full Waveform Inversion With Irregular Shot Sampling. *Society of Exploration Geophysicists* (2014), 1147–1151. <https://www.onepetro.org/conference-paper/SEG-2014-0234>

Chapter 5

Bone Ablation Depth Estimation from Er:YAG Laser-generated Acoustic Waves

The previous approach to reconstructing the bone with the acoustic wave using the **FE** method was too slow and not applicable for a real-time simulation. In addition, there are many unknown factors, and therefore we could not confirm our results (resp. the correctness of our forward problem simulation) in an *ex-vivo* experiment. Therefore, we simplify the problem and reduce the unknown factors as much as possible. In previous work, they could differentiate the different tissue being ablated [45]. We investigate the viability of predicting the depth of a cut in a bone resulting from the ablation process. In [14], they found that the ablation process is non-linear, so counting the number of ablations to predict the depth is insufficient. We analyze the prediction of the depth of the laser cut using the acoustic wave created during the ablation process with the help of a **NN**. We conclude that depth information is indeed embedded in the acoustic wave.

Publication The following paper [78] was published on the 30th of November 2022 in the *IEEE Access* Journal.

GitHub code: <https://gitlab.com/cian.unibas.ch/ablaiton-depth-estimation>

Received 4 October 2022, accepted 9 November 2022, date of publication 30 November 2022, date of current version 7 December 2022.

Digital Object Identifier 10.1109/ACCESS.2022.3225651



RESEARCH ARTICLE

Bone Ablation Depth Estimation From Er:YAG Laser-Generated Acoustic Waves

CARLO SEPPI^{1,2}, ANTAL HUCK^{1,2}, ARSHAM HAMIDI^{1,3}, EVA SCHNIDER^{1,2}, MASSIMILIANO FILIPOZZI^{1,2}, GEORG RAUTER^{1,4}, (Member, IEEE), AZHAR ZAM^{1,3,5,6}, AND PHILIPPE C. CATTIN^{1,2}, (Member, IEEE)

¹Department of Biomedical Engineering, University of Basel, 4001 Basel, Switzerland

²Center for Medical Image Analysis and Navigation (CIAN), 4123 Allschwil, Switzerland

³Biomedical Laser and Optics Group (BLOG), 4123 Allschwil, Switzerland

⁴Bio-Inspired Robots for Medicine-Laboratory (BIROMED-Lab), 4123 Allschwil, Switzerland

⁵Division of Engineering, New York University Abu Dhabi (NYUAD), Abu Dhabi, United Arab Emirates

⁶Department of Biomedical Engineering, Tandon School of Engineering, New York University, Brooklyn, NY 11201, USA

Corresponding author: Carlo Seppi (carlo.seppi@unibas.ch)

This work was supported by the Werner Siemens Foundation through the Minimally Invasive Robot-Assisted Computer-Guided Laserosteotomy (MIRACLE) Project.

ABSTRACT Using a laser for cutting bones instead of the traditional saws improves a patient's healing process. Additionally, the laser has the potential to reduce the collateral damage to the surrounding tissue if appropriately applied. This can be achieved by building additional sensing elements besides the laser itself into an endoscope. To this end, we use a microsecond pulsed Erbium-doped Yttrium Aluminium Garnet (Er:YAG) laser to cut bones. During ablation, each pulse emits an acoustic shock wave that is captured by an air-coupled transducer. In our research, we use the data from these acoustic waves to predict the depth of the cut during the ablation process. We use a Neural Network (NN) to estimate the depth, where we use one or multiple consecutive measurements of acoustic waves. The NN outperforms the base-line method that assumes a constant ablation rate with each pulse to predict the depth. The results are evaluated and compared against the ground-truth depth measurements from Optical Coherence Tomography (OCT) images that measure the depth in real-time during the ablation process.

INDEX TERMS Acoustic feedback, depth control, laser ablation, neural network.

I. INTRODUCTION

Reducing the trauma of a patient during surgical procedures is paramount in improving the post-surgical standard of living. Consequently, minimally invasive alternatives to common interventions are a highly researched topic [1], [2]. One line of inquiry is the replacement of mechanical tools with laser-based ablation [3], [4], [5], [6], [7].

When the tissue is exposed to microsecond pulsed Er:YAG laser light, the water in the tissue heats up, vaporizes, and the expansion causes micro-explosions that ablate a small part of the tissue [8]. This process emits an acoustic wave that is captured by a transducer [9].

The associate editor coordinating the review of this manuscript and approving it for publication was Ahsan Khandoker.

In contrast to classical mechanical cutting tools, laser ablation does not provide direct haptic feedback on the progress of the cut to the surgeon. Furthermore, the laser system occludes the cutting location and impedes visual inspection. With the development of new tools that assist the surgeon in monitoring the depth of the cut, damaging sensitive tissue can be avoided.

A classical method to measure the cutting depth would be using an OCT [10], [11], [12], [13]. However, it can be challenging to integrate an OCT in combination with an Er:YAG laser for minimally invasive surgery. To this end, we propose an acoustic depth measurement technique that uses the acoustic wave created during the ablation process to determine the depth of the cut.

When the location of the ablation source is known, the depth of the cut can be estimated via various approaches. One

approach is to triangulate the source [14], [15], [16]. However, this approach requires multiple transducers to determine the source location. A different approach uses acoustic waves in a 2D simulation to detect the source position using just two transducers [17]. The main limitation of this approach is that the exact acoustic wave generator (form and the frequency composition of the source) has to be known. In another 2D simulation, the source position and its form were reconstructed in an unknown surrounding [18]. However, many transducers are required for the reconstruction, making this approach unsuitable for minimally invasive surgery.

There are several ways to determine the distance between an acoustic source and the transducer. One option is to estimate the time-of-flight (ToF). For example, in [19], the authors used auto-correlation between the transmitted and echoed signal. In [20], they exploited the phase shift between transmitting and measured signals. However, in our application, the source signal shape is unknown, and the signal may even change for different depths. In [21] and [22], the authors showed that the ToF correlates with the signal's distance and decay when ablating tissue with an Er:YAG laser and in [23], they used ToF to estimate the depth of the ablation with a Neodymium-doped Yttrium Aluminium Garnet (Nd:YAG) laser. However, the ToF option has a significant drawback. It requires the distance between the transducer and the bone surface to be constant, and the medium velocity of the ablated tissue must be known. As this can not be guaranteed in our envisioned application of robotic-guided laser osteotomy, we focus on different approaches to estimate the depth of the laser cut.

Since the use of Neural Networks [24] is well established in medical imaging [25], [26], [27], [28], speech, and signal processing [29], [30], [31], [32], we aim to estimate the ablation depth by interpreting the signal from one single air-coupled transducer with a neural network. We compare two approaches: The CA is used as a base-line approach, where we assume that the ablation rate per pulse is constant, and therefore, the depth is proportional to the number of ablation shots. The second approach uses one or multiple consecutive measurements of the acoustic waves during the ablation process. These acoustic waves are then used as input for an NN to predict the depth of the laser cut.

The goal of this work is to analyze the acoustic wave and to prove that there is depth information in the acoustic wave produced during the ablation process of the bone using the Er:YAG laser. In addition, we can show that one transducer is sufficient to measure the depth of the laser cut, simplifying the complexity of the setup in future work.

II. MATERIAL AND SETUP

An Er:YAG laser (Syneron Candela, litetouch LI-FG0001A) with an energy of 153 mJ, a wavelength of 2940 nm, with a repetition rate of 10 Hz, is used for ablating the bone. The ablation process emits an acoustic wave. A CaF_2 mirror diverts a small percentage of the laser beam to a PbSe photodiode (PbSe Fixed Gain Detector,

PDA20H, 1500 – 4800 nm), to trigger the acoustic measurement. The wideband transducer,¹ with a frequency range of 100 – 1000 kHz and a resonant frequency at 650 kHz, measures acoustic signals with a sample rate of 7.8125 MHz. It is placed at a distance of approximately 5 cm to the bone surface. The setup is displayed on the left of Fig. 1. We note that due to the limited acquisition rate of our setup, and the high repetition rate of the laser, we can only measure the acoustic wave of every second laser pulse.

A custom-made dichroic filter reflects the wavelength of the Er:YAG laser and transmits the OCT's wavelength, therefore, integrating the Er:YAG laser into the OCT system in a co-axial configuration. Consequently, we can monitor the ablation depth with a long-range Bessel-like beam OCT system [33] in real-time. The OCT has an imaging half-range of 22.21 mm in air and a field-of-view of 4.2 mm. The OCT system uses a swept-source laser (Insight Photonic Solution, Inc., Lafayette, Co, USA), with a scan rate of 104.17 kHz, a central wavelength of 1288.82 nm, and spectral bandwidth of 61.5 nm.

We used 13 cow femur bones as ablation material, bought in a local grocery store. The height of the bone varied between 2.4 cm to 2.9 cm. Muscle, fat, bone marrow, and tendons were carefully removed from the hard bone. To avoid dehydration of the bone, we submerged the samples in water between experiments.

We conducted our experiment by ablating a maximum of nine holes in each bone, each reaching a depth of up to 3.5 mm. The ablation process was stopped when we noticed that the cutting depth stagnated, i.e. if the bone started carbonizing. Bone carbonizes when insufficient water is in the tissue; hence, no micro-explosions remove the tissue, and the laser energy accumulates heating up the tissue. An exemplary bone is shown on the right of Fig. 1.

Since the frame rate of the OCT is 173.6167 Hz and the repetition rate of the laser is 10 Hz, we have a fixed number of OCT frames between the laser pulses. Therefore, we can align the OCT frames to the corresponding acoustic waves emitted during bone ablation. To generate a ground truth depth for each measured ablation wave, we locate the first pulse of the ablation in the OCT image stream. Then we labeled the 2443 OCT images by marking the bone's edge and the cut's end (see Fig. 2). We deduced the depth of the cut using the pixel resolution of the OCT of 10.86 μm .

III. METHOD

To assess the performance of our approaches, we divided our data into three mutually disjoint subgroups: training data, validation data, and testing data. Each bone was only part of one of these groups. Five-fold cross-validation was conducted to demonstrate the performance of the approach.

We investigated two approaches: (1) the first approach CA assumes that the ablation rate of the laser is constant, and

¹PHYSICAL ACOUSTICS WS& SNAK28
6.9.2022, physicalacoustics.com/content/literature/sensors/Model_WSa.pdf

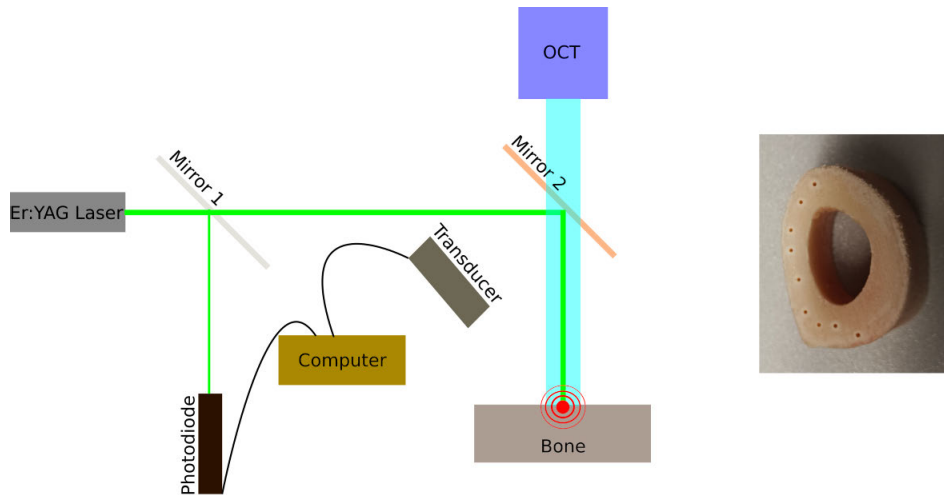


FIGURE 1. (Left) the setup of our experiment. Laser light ablates the bone while the air-coupled transducer measures the acoustic wave. The laser beam gets split at mirror 1, and a small percentage of the laser beam is redirected to the photodiode. The photodiode triggers the acquisition of the acoustic wave with the transducer (distance to the bone: 5 cm at a 45° angle to the ablation). Further, the laser light is diverted with mirror 2 (a custom-made dichroic filter that reflects the wavelength of the Er:YAG laser and transmits the OCT's wavelength) onto the bone for the ablation. At the same time, the OCT measures the depth of the ablation. (Right) an exemplary bone with nine holes after the ablation process.

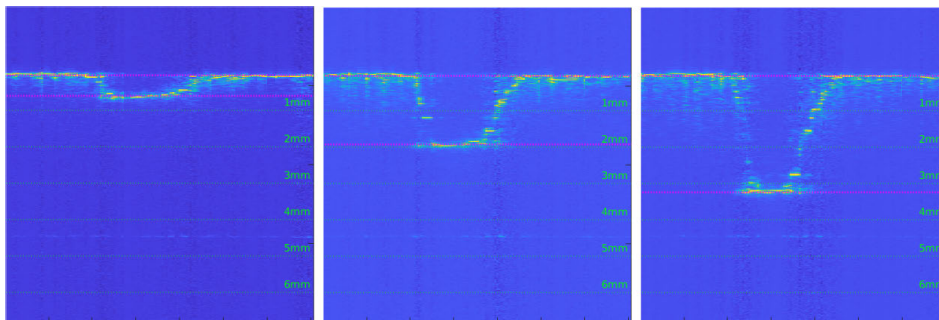


FIGURE 2. Exemplary OCT images, where we manually labeled the image after 10, 35, and 60 ablations. These corresponds to the depth of 0.5 mm, 1.9 mm, and 3.1 mm.

therefore when counting the number of shots, it can predict the depth of the laser cut. The ablation rate is estimated by the median value of the ablation rate of the training and validation data, and its performance is evaluated on the testing data. (2) In the second approach, we use a NN to predict the depth using the acoustic ablation waves.

A. NEURAL NETWORK (NN)

As the distance between the surface of the bone and the transducer can vary, all approaches using the ToF to estimate the cutting depth are of limited use. Furthermore, we wish to investigate if the depth information of a cut is embedded in other parts of the acoustic signal (excluding the ToF);

hence, we removed this information by cropping the signal as follows: First, we identified the maximum absolute value of the first 500 sample points (the time window of 64 μ s). Then we used 1.5 times this value as a noise threshold to remove the first part of the signal that only contained noise and no signal from the ablation (see Fig. 3, top left): We removed all sample points before the absolute value of the acoustic wave that first exceeded this threshold (see Fig. 3, top right, red dot) and solely used the window after that point (see Fig. 3, bottom left). In the final step, we normalized the area of interest of the acoustic wave w with:

$$w = \frac{w^* - \bar{w}}{\sigma_w} \quad (1)$$

where \bar{w} is the mean value and σ_w is the standard deviation of the preprocessed acoustic wave w^* (see Fig. 3, bottom right).

To reduce over-optimization during training, we applied non-linear scaling of the wave amplitudes as data augmentation: Each sample point of the acoustic wave w was scaled by the formula

$$\hat{w} = w \cdot (1 + \lambda \cdot \exp[|w|]) \quad (2)$$

with λ a uniformly distributed random scaling factor.

As an input for the NN, we tried three different variants; namely, one, five, or ten consecutively measured acoustic signals as the input to the NN₁, NN₅, and NN₁₀, respectively. The Output of the NNs was a single value corresponding to the depth of the laser cut in [mm] from the latest measurement from the input. We trained the network using the *Mean Square Error Loss* (MSELoss):

$$\mathcal{L}_{MSE}(x, y) = \frac{1}{N_B} \sum_{i=1}^{N_B} (x_i - y_i)^2 \quad (3)$$

where $x = (x_1, \dots, x_{N_B})$ is the output of the NN and $y = (y_1, \dots, y_{N_B})$ is the label, that we labeled manually using the OCT images (see Section II and Fig. 2), and N_B is the batch size.

B. HYPERPARAMETER SEARCH

We use a hyperparameter search [34], [35] approach with five consecutive acoustic waves to find an initial network with the following search constraints, as visualized in Table 1. The input size, which correspond to the number of sample points, varies between 2000, 3000, . . . , 7000. The numbers of convolutional and fully connected layers vary between 1 and 9. The parameters of the convolution layers can get the following values: Each output channel can allocate a value of 2^n , where n varies between $n = 1, \dots, 8$, the kernel size varies between 2 and 5, and the stride is 1 or 2. In addition, the maxpool kernel is 2 or 3 with a stride of 1 or 2. Batch normalization is applied randomly before any layer, and dropout is randomly applied to the fully connected layers with a dropout rate between 0 and 1. The number of neurons of the fully connected layer is $\min(2^n, out_{CNN})$, where n varies between $n = 3, \dots, 11$ and out_{CNN} is the number of neurons after the flattened output of the last convolutional layer. We use the Adam optimizer with a learning rate of 10^{-n} , where n varies between $n = 2, \dots, 5$. The maximum value λ of (2), varies between 0, 0.1, . . . , 1.

C. IMPLEMENTATION DETAILS

We implemented the network using the PyTorch² [36] framework and trained the networks on an NVIDIA Tesla V100 DGXS 16 GB. As a result of the hyperparameter search, a well-performing architecture is shown in Fig. 4, which uses 2000 sample points as the input size, namely a time window of 256 μ s, for the NN. It has 5 convolutional layers followed

TABLE 1. Overview of the parameter used in the hyperparameter search. Batch normalization is randomly applied before the convolutional and fully connected layers, and the dropout layers are randomly applied on the fully connected layers. out_{CNN} is the number of neurons after the flattened output of the last convolutional layer.

Input size (# of sample points):	{2000, 3000, . . . , 7000}
Convolutional Layer	
Number of layers:	{1, . . . , 9}
Output channels:	2^n , with $n \in \{1, \dots, 8\}$
Kernel size:	{2, 3, 4, 5}
Stride:	{1, 2}
Maxpool layer	
Kernel size:	{2, 3}
Stride:	{1, 2}
Fully connected layer	
Number of layers:	{1, . . . , 9}
Neurons:	$\min(2^n, out_{CNN})$, with $n \in \{3, \dots, 11\}$
Dropout:	$p \in \mathcal{U}(0.1, 0.8)$
Optimizer:	Adam
learning rate:	10^{-n} , with $n \in \{2, 3, 4, 5\}$
Data augmentation:	$\max[\lambda] \in \{0, 0.1, \dots, 1\}$

by 8 fully connected layers with 1024 neurons. The Adam optimizer had a learning rate of 10^{-3} , a batch size of $N_B = 32$, and the data augmentation parameter λ in (2) was a random value between -0.5 and 0.5 . In addition, batch normalization uses a momentum of 0.1 and $\text{eps}=1\text{e-}05$, while the maxpool layer had a padding of 0 with dilation of 1. The Dropout layer had the parameter $\text{inplace}=\text{False}$, and the Linear layers bias was set to true. The code is published on our GitLab page.³

IV. RESULTS

We evaluated the accuracy of our models through five-fold cross-validation, which included splitting the data into five mutually disjoint subsets and omitting one subset during training for unseen forward passes during testing.

We assumed a constant ablation rate in the first approach CA. The median error over all the five-fold cross-validation sets was 0.13 mm and the distance \mathcal{B} between the 25th percentile and the 75th percentile was 0.163 mm, as shown in Table 2. In Fig. 5, we visualize a box plot that shows the distribution of the deviating distance between the ground truth value and the output. As shown in Table 2, we see that the average box length was 0.271 mm with an average median value of -0.024 mm. At the interval between $\mathcal{I} = [3.25, 3.5]$ mm the median value was -0.076 mm with a box length of 0.396 mm. We note that the number of shots was counted from the start of the ablation process to determine the depth of the cut.

In the second approach, we used one, five, or ten consecutively measured acoustic waves as the input for the NN. We trained the network on the training data and used the best-performing network on the validation data to test the performance of the testing data. In Table 2, we give a detailed description of the results. The median error was 0.174 mm, 0.130 mm, and 0.092 mm for NN₁, NN₅, and NN₁₀, respectively. In the box plots of Fig. 5, we visualize the difference

²May 2022, pytorch.org

³<https://gitlab.com/cian.unibas.ch/ablation-depth-estimation>

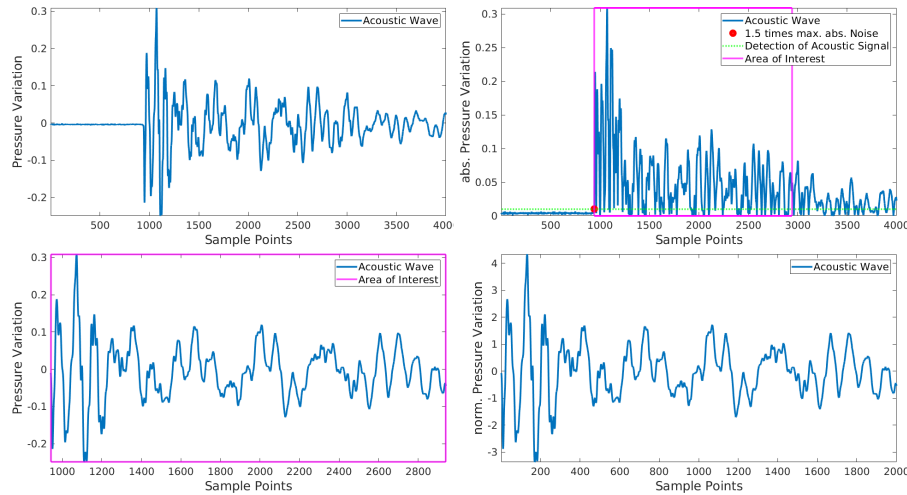


FIGURE 3. (Top left) measured acoustic wave with a sample rate of 7.8125 MHz. (Top right) multiply the maximum absolute value of the 500 first sample points (time window of $64 \mu\text{s}$) by 1.5 (green). Remove all the data before the intersection between the green line and the acoustic signal from the ablation (redpoint). The 2000 sample points (time window of $256 \mu\text{s}$) after the red dot are used for the further processing step (magenta). (Bottom left) the acoustic wave is visualized, where the time-of-flight is removed. (Bottom right) Normalized acoustic wave in the area of interest, which we use as input for the NN.

```
(0): Input(size= $N \times 2000$ ), BatchNorm1d()
(1a): Conv1d(out_c=8, k_size=4, s=1)
(1b): MaxPool1d(k_size=3, s=2)
(2a): Conv1d(out_c=32, k_size=4, s=2)
(2b): MaxPool1d(k_size=3, s=2)
(3a): Conv1d(out_c=64, k_size=4, s=1)
(3b): MaxPool1d(k_size=2, s=1)
(4a): Conv1d(out_c=256, k_size=5, s=2)
(4b): BatchNorm1d()
(4c): MaxPool1d(k_size=3, s=2)
(5a): Conv1d(out_c=256, k_size=4, s=2)
(5b): BatchNorm1d()
(5c): MaxPool1d(k_size=2, s=1)
(6): Flattening(size=6912)
(7a): Dropout(p=0.48536), Linear(out_f=1028)
(7b): BatchNorm1d()
(8a): Linear(out_f=1028)
(8b): BatchNorm1d()
(9a): Linear(out_f=1028)
(9b): BatchNorm1d()
(10): Dropout(p=0.54307), Linear(out_f=1028)
(11a): Dropout(p=0.43455), Linear(out_f=1028)
(11b): BatchNorm1d()
(12a): Dropout(p=0.56238), Linear(out_f=1028)
(12b): BatchNorm1d()
(13a): Dropout(p=0.19907), Linear(out_f=1028)
(13b): BatchNorm1d()
(14): Dropout(p=0.20917), Linear(out_f=1028)
(15): Linear(out_f=1)
⇒ Output for MSELoss
```

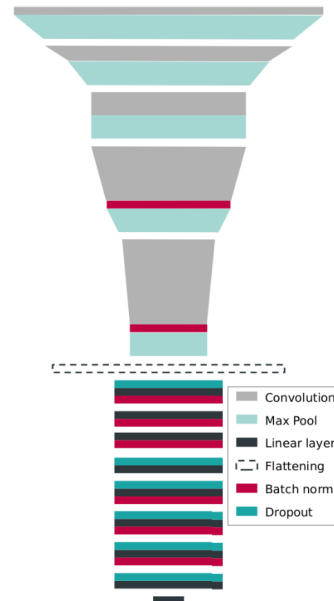


FIGURE 4. Detailed description of the neural network (left) and graphical visualization (right). It has 5 convolutional layers, followed by 8 fully connected layers. We chose a batch size of $N_B = 32$ and used the Adam optimizer. We note, that k_size represents the kernel size, s is the stride, out_c are the channel out, and out_f are the number output feature.

between the ground truth value and the label's output. Here, the mean length of the boxes \mathcal{B} were 0.336 mm, 0.253 mm, and 0.200 mm for NN_1 , NN_5 , and NN_{10} , with a mean median

value of -0.010 mm, -0.036 mm, and -0.027 mm, respectively. The largest errors were located at the interval \mathcal{I} (in the last box plot of each subfigure) with a median value of

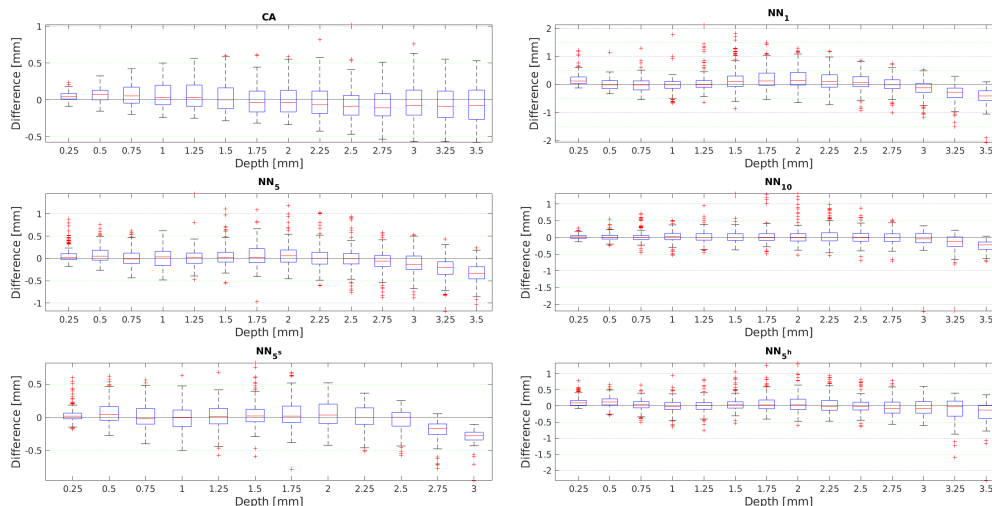


FIGURE 5. The box plots visualize the difference between the output and ground truth depth. CA is the method where we assume a constant ablation rate. NN_1 , NN_5 , and NN_{10} are the NN approaches with one, five, or ten consecutive acoustic measurements, respectively. NN_{5s} and NN_{5h} use five consecutive acoustic measurements as input. NN_{5s} data do not exceed the depth of 2.8 mm, and NN_{5h} uses some label augmentation. Each value on the x-axis corresponds to an interval, e.g., 0.25 mm represents the interval between 0 and 0.25 mm.

−0.407 mm, −0.332 mm, and −0.222 mm. The box length \mathcal{B} was 0.349 mm, 0.275 mm, and 0.218 mm for NN_1 , NN_5 , and NN_{10} , respectively.

V. DISCUSSION

We compared two approaches: CA, which assumes a linear estimation of the depth and a NN with either one (NN_1), five (NN_5), or ten (NN_{10}) consecutively measured acoustic waves as an input. In the box plots in Fig. 5, we observed that CA has fewer outliers than the NNs. The median value is close to 0 for all intervals, and even within the interval \mathcal{I} ($Distance_I$), the median value was close to 0. The NNs had more outliers, and the median value between the distance of the output and the ground truth depth shifts into the negative with increasing depth. Hence, it underestimated the depth of the cut, especially in the interval \mathcal{I} , as can be seen in Table 2 and Fig. 5. However, the box length \mathcal{B} was smaller for the NN than the CA for the interval \mathcal{I} . We further observed that CA outperforms the NN_1 and had a similar performance to NN_5 . The best performing network was NN_{10} .

To further investigate the underestimation of the depth, we retrained the Network NN_5 with data that reaches a maximum depth of 2.8 mm (NN_{5s}). We observe in Fig. 5 that both NN_5 and NN_{5s} had a significantly larger error in the reported interval \mathcal{I} and [2.75, 3]mm, respectively. This is also reflected in Table 2, where the median value at $Distance_I$ were −0.332 mm and −0.278 mm, with a box length of 0.275 mm and 0.117 mm, respectively. Therefore, we assume that underestimating the depth at the end is due to the lack of training data.

TABLE 2. In the top row, the error, in the centre row, the mean distance over all intervals between the estimation and the label from the box-plots in Fig. 5, and in the bottom row, the distance of the last interval from the box-plots $Distance_I$ are described. We show the median, 25th percentile (PCTL), 75th PCTL value, and the distance \mathcal{B} , which is the difference between the 25th and 75th PCTL, of all the testing data from the cross-validation. CA is the method where we assume a constant ablation rate. NN_1 , NN_5 , and NN_{10} are the approach with the NN that uses one, five, or ten consecutive acoustic measurements. NN_{5s} and NN_{5h} use 5 consecutive acoustic signals as input. NN_{5s} data do not exceed 2.8 mm depth, and therefore $Distance_I$ represents the interval 2.75 mm – 3 mm, while all the others represent the interval of $\mathcal{I} = [3.25, 3.5]$ mm. NN_{5h} was trained with some label augmentation.

mm	Median Value	25th PCTL	75th PCTL	distance \mathcal{B}
<i>Error</i>				
CA	0.130	0.065	0.228	0.163
NN_1	0.174	0.081	0.326	0.245
NN_5	0.130	0.060	0.252	0.192
NN_{10}	0.092	0.040	0.189	0.149
NN_{5s}	0.110	0.047	0.213	0.166
NN_{5h}	0.135	0.065	0.251	0.187
<i>Distance</i>				
CA	−0.024	−0.139	0.132	0.271
NN_1	−0.010	−0.1641	0.172	0.336
NN_5	−0.036	−0.158	0.096	0.253
NN_{10}	−0.027	−0.120	0.080	0.200
NN_{5s}	−0.026	−0.123	0.083	0.206
NN_{5h}	0.003	−0.136	0.143	0.278
<i>Distance_I</i>				
CA	−0.076	−0.263	0.133	0.396
NN_1	−0.407	−0.571	−0.222	0.349
NN_5	−0.332	−0.460	−0.185	0.275
NN_{10}	−0.222	−0.356	−0.138	0.218
NN_{5s}	−0.278	−0.340	−0.224	0.117
NN_{5h}	−0.127	−0.392	0.023	0.415

To this end, we retrained the network with label augmentation. Specifically, we added a random value r to the depth during the training of the network for all depths exceeding

3 mm. The value r is the absolute random number from the normal distribution $\mathcal{N}(0, 0.5)$, with the mean value of 0 mm and the standard deviation of 0.5 mm. We augmented the label as described above, leading to overestimating the depth during the network training. In Fig. 5 we can see that this strategy counteracts the general underestimation of the depth of the network at the last intervals. This is also reflected in Table 2, where the median value of $Distance_l$ was reduced from -0.332 mm to -0.127 mm. However, the box length B was increased to the value 0.275 mm to 0.415 mm. Therefore, augmenting the data improves the median accuracy but produces a higher output fluctuation.

VI. CONCLUSION

The experiments show that assuming a constant ablation rate already leads to good depth estimations of the cut by only counting the number of shots. This assumption, however, is limited to shallow cuts and does not hold for deep bone ablations that need a cooling system [37]. These cuts can reach a depth of up to 3 cm. Moreover, the number of shots must be maintained for a valid estimation. This is not stateless, meaning it needs all the information since the beginning of the ablation to estimate the depth. Therefore, it is not fail-safe since it may cause loss of depth information in case the number of the previous ablation gets lost.

It is essential for medical devices to continue working, even when a power failure occurs and all prior information is lost. Hence, we opt for a stateless method to ensure a fail-safe device. In this regard, the proposed approach with the NN is stateless (almost no prior information of previous ablations is needed) and, therefore, advantageous as it uses one or multiple consecutive acoustic waves as an input to predict the depth of the cut and does not need all information from the beginning of the ablation. Therefore, it is fail-safe and can predict the depth after only a few laser pulses. The NN approach has comparable accuracy but slightly more outliers due to its statelessness and sensitivity. The performance improved with an increasing number of consecutive acoustic waves used as input. Too many consecutive acoustic waves are disadvantageous because multiple acoustic waves are needed to estimate the depth accurately, increasing the risk of cutting the hole too deep and damaging sensitive tissue behind the bone.

In this work, we demonstrate the possibility of predicting the depth of a laser-ablated hole by analyzing the acoustic shock waves captured by a single transducer. The results encourage further investigations into the depth estimation during the laser ablation of tissue using acoustic waves. Our experiments were performed in a dry environment, and for future work, we plan depth estimation during a similar setup in wet conditions. Irrigation during laser ablation allows deeper cuts yet presents further challenges in combination with OCT systems. One of the challenges facing the irrigation system is that water accumulates in the hole, distorting depth measurement. In addition, the debris and water droplets pollute the OCT's protective window, reducing the image's

contrast. An important factor may be the heterogeneity and the age of the bone influence the ablation process and the prediction of the depth using acoustic waves, which needs to be investigated.

ACKNOWLEDGMENT

We acknowledge the funding by the Werner Siemens Foundation through the MIRACLE (Minimally Invasive Robot-Assisted Computer-guided Laserosteotomy) project. We are grateful to Peter Zimmermann (Institute of Anatomy, University Basel) for helping prepare the bone specimens.

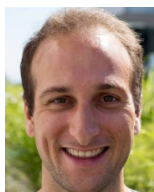
REFERENCES

- [1] J. C. Hu, X. Gu, S. R. Lipsitz, M. J. Barry, A. V. D'Amico, A. C. Weinberg, and N. L. Keating, "Comparative effectiveness of minimally invasive vs open radical prostatectomy," *JAMA*, vol. 302, no. 14, pp. 1557–1564, 2009.
- [2] J. D. Luketich, M. Alvelo-Rivera, P. O. Buenaventura, N. A. Christie, J. S. McCaughan, V. R. Little, P. R. Schauer, J. M. Close, and H. C. Fernando, "Minimally invasive esophagectomy: Outcomes in 222 patients," *Ann. Surg.*, vol. 238, no. 4, p. 486, 2003.
- [3] D. D. Lo, M. A. Mackanos, M. T. Chung, J. S. Hyun, D. T. Montoro, M. Grova, C. Liu, J. Wang, D. Palanker, A. J. Connolly, M. T. Longaker, C. H. Contag, and D. C. Wan, "Femtosecond plasma mediated laser ablation has advantages over mechanical osteotomy of cranial bone," *Lasers Surg. Med.*, vol. 44, no. 10, pp. 805–814, Dec. 2012.
- [4] S. R. Visuri, J. T. Walsh, and H. A. Wigdor, "Erbium laser ablation of dental hard tissue: Effect of water cooling," *Lasers Surg. Med.*, vol. 18, no. 3, pp. 294–300, 1996.
- [5] K.-W. Baek, W. Deibel, D. Marinov, M. Griessen, M. Dard, A. Bruno, H.-F. Zeilhofer, P. Cattin, and P. Juergens, "A comparative investigation of bone surface after cutting with mechanical tools and Er: YAG laser," *Lasers Surg. Med.*, vol. 47, no. 5, pp. 426–432, Jul. 2015.
- [6] K.-W. Baek, M. Dard, H.-F. Zeilhofer, P. C. Cattin, and P. Juergens, "Comparing the bone healing after cold ablation robot-guided Er:YAG laser osteotomy and piezoelectric osteotomy—A pilot study in a minipig mandible," *Lasers Surg. Med.*, vol. 53, no. 3, pp. 291–299, 2021. [Online]. Available: <https://onlinelibrary.wiley.com/doi/abs/10.1002/lsm.23281>, doi: 10.1002/lsm.23281.
- [7] M. Augello, W. Deibel, K. Nuss, P. Cattin, and P. Juergens, "Comparative microstructural analysis of bone osteotomies after cutting by computer-assisted robot-guided laser osteotomy and piezoelectric osteotomy: An in vivo animal study," *Lasers Med. Sci.*, vol. 33, no. 7, pp. 1471–1478, Sep. 2018.
- [8] H. Kang, I. Rizoïu, and A. Welch, "Hard tissue ablation with a spray-assisted mid-ir laser," *Phys. Med. Biol.*, vol. 52, no. 24, p. 7243, 2007.
- [9] H. K. N. Kenhagho, G. Rauter, R. Guzman, P. C. Cattin, and A. A. Zam, "Comparison of acoustic shock waves generated by micro and nanosecond lasers for a smart laser surgery system," *Proc. SPIE*, vol. 10484, Feb. 2018, Art. no. 104840P.
- [10] A. Fuchs, M. Schultz, A. Krüger, D. Kundrat, J. Díaz Díaz, and T. Ortmaier, "Online measurement and evaluation of the Er: YAG laser ablation process using an integrated OCT system," *Biomed. Eng. Biomedizinische Technik*, vol. 57, pp. 1–4, Jan. 2012.
- [11] J. D. Díaz, D. Kundrat, K.-F. Goh, O. Majdani, and T. Ortmaier, "Towards intra-operative OCT guidance for automatic head surgery: First experimental results," in *Medical Image Computing and Computer-Assisted Intervention—MICCAI 2013*, K. Mori, I. Sakuma, Y. Sato, C. Barillot, and N. Navab, Eds. Berlin, Germany: Springer, 2013, pp. 347–354.
- [12] Y. Zhang, T. Pfeiffer, M. Weller, W. Wieser, R. Huber, J. Raczkowski, J. Schipper, H. Wörn, and T. Klenzner, "Optical coherence tomography guided laser cochleostomy: Towards the accuracy on tens of micrometer scale," *BioMed Res. Int.*, vol. 2014, pp. 1–10, Sep. 2014.
- [13] Y. A. Bayhaqi, A. Hamidi, F. Canbaz, A. A. Navarini, P. C. Cattin, and A. Zam, "Kalman filtered depth prediction using Optical Coherence Tomography for laser bone cutting," Jun. 2021, doi: 10.5281/zenodo.4922992.
- [14] B.-W. Jang and C.-G. Kim, "Acoustic emission source localization in composite stiffened plate using triangulation method with signal magnitudes and arrival times," *Adv. Compos. Mater.*, vol. 30, no. 2, pp. 149–163, Mar. 2021.

- [15] B.-W. Jang, Y.-G. Lee, J.-H. Kim, Y.-Y. Kim, and C.-G. Kim, "Real-time impact identification algorithm for composite structures using fiber Bragg grating sensors," *Struct. Control Health Monitor.*, vol. 19, no. 7, pp. 580–591, Nov. 2012.
- [16] B.-W. Jang and C.-G. Kim, "Impact localization of composite stiffened panel with triangulation method using normalized magnitudes of fiber optic sensor signals," *Compos. Struct.*, vol. 211, pp. 522–529, Mar. 2019.
- [17] U. Nahum, A. Zam, and P. C. Cattin, "Bone reconstruction and depth control during laser ablation," in *Computational Methods and Clinical Applications in Musculoskeletal Imaging*, T. Vrtovec, J. Yao, G. Zheng, and J. M. Pozo, Eds. Cham, Switzerland: Springer, 2019, pp. 126–135.
- [18] U. Nahum, C. Seppi, and P. C. Cattin, "Joint inverse medium and optimal control problem for acoustic waves," in *Proc. Platform Adv. Sci. Comput. Conf.*, Jun. 2019, p. 8.
- [19] D. Marioli, C. Narduzzi, C. Offelli, D. Petri, E. Sardini, and A. Taroni, "Digital time-of-flight measurement for ultrasonic sensors," *IEEE Trans. Instrum. Meas.*, vol. 41, no. 1, pp. 93–97, Feb. 1992.
- [20] X. Chen, J. Xu, H. Chen, H. Ding, and J. Xie, "High-accuracy ultrasonic rangefinders via pMUTs arrays using multi-frequency continuous waves," *J. Microelectromech. Syst.*, vol. 28, no. 4, pp. 634–642, Aug. 2019.
- [21] H. N. Kenhagho, F. Canbaz, R. Guzman, P. Cattin, and A. Zam, "Miniaturized optoacoustic feedback sensor for smart laser osteotomy: Fiber-coupled Fabry-Pérot etalon sensor," *Sens. Actuators A, Phys.*, vol. 317, Jan. 2021, Art. no. 112394.
- [22] H. N. Kenhagho, I. Sugiarto, R. Guzman, P. Cattin, and A. Zam, "Contact-free Crater depth monitoring using measured acoustic shock waves for smart laser surgery applications: Preliminary result," in *Proc. Int. Conf. Radar, Antenna, Microw., Electron., Telecommun. (ICRAMET)*, Oct. 2019, pp. 118–121.
- [23] F. J. Landa, X. L. Deán-Ben, F. M. de Espinosa, and D. Razansky, "Non-contact monitoring of incision depth in laser surgery with air-coupled ultrasound transducers," *Opt. Lett.*, vol. 41, no. 12, pp. 2704–2707, Jun. 2016.
- [24] Y. Bengio, A. Courville, and P. Vincent, "Representation learning: A review and new perspectives," *IEEE Trans. Pattern Anal. Mach. Intell.*, vol. 35, no. 8, pp. 1798–1828, Aug. 2013.
- [25] S. N. Deepa, "A survey on artificial intelligence approaches for medical image classification," *Indian J. Sci. Technol.*, vol. 4, no. 11, pp. 1583–1595, Nov. 2011.
- [26] Q. Li, W. Cai, X. Wang, Y. Zhou, D. D. Feng, and M. Chen, "Medical image classification with convolutional neural network," in *Proc. 13th Int. Conf. Control Autom. Robot. Vis. (ICARCV)*, Dec. 2014, pp. 844–848.
- [27] A. Kumar, J. Kim, D. Lyndon, M. Fulham, and D. Feng, "An ensemble of fine-tuned convolutional neural networks for medical image classification," *IEEE J. Biomed. Health Inform.*, vol. 21, no. 1, pp. 31–40, Jan. 2016.
- [28] E. Schindler, A. Horváth, G. Rauter, A. Zam, M. Müller-Gerbl, and P. C. Cattin, "3D segmentation networks for excessive numbers of classes: Distinct bone segmentation in upper bodies," in *Machine Learning in Medical Imaging*, M. Liu, P. Yan, C. Lian, and X. Cao, Eds. Cham, Switzerland: Springer, 2020, pp. 40–49.
- [29] A. S. Miller, B. H. Blott, and T. K. Hames, "Review of neural network applications in medical imaging and signal processing," *Med. Biol. Eng. Comput.*, vol. 30, no. 5, pp. 449–464, Sep. 1992.
- [30] S. Kiranyaz, T. Ince, and M. Gabbouj, "Real-time patient-specific ECG classification by 1-D convolutional neural networks," *IEEE Trans. Biomed. Eng.*, vol. 63, no. 3, pp. 664–675, Aug. 2015.
- [31] Y. Han and K. Lee, "Convolutional neural network with multiple-width frequency-delta data augmentation for acoustic scene classification," in *Proc. IEEE AASP Challenge Detection Classification Acoustic Scenes Events*, Jun. 2016, pp. 1–4. [Online]. Available: https://dcase.community/documents/challenge2016/technical_reports/DCASE2016_Lee_1034.pdf
- [32] H. Kamper, W. Wang, and K. Livescu, "Deep convolutional acoustic word embeddings using word-pair side information," in *Proc. IEEE Int. Conf. Acoust., Speech Signal Process. (ICASSP)*, Mar. 2016, pp. 4950–4954.
- [33] A. Hamidi, Y. A. Bayhaqi, F. Canbaz, A. A. Navarini, P. Cattin, and A. Zam, "Long-range optical coherence tomography with extended depth-of-focus: A visual feedback system for smart laser osteotomy," *Biomed. Opt. Exp.*, vol. 12, no. 4, pp. 2118–2133, 2021.
- [34] L. Li, K. Jamieson, G. DeSalvo, A. Rostamizadeh, and A. Talwalkar, "Hyperband: A novel bandit-based approach to hyperparameter optimization," *J. Mach. Learn. Res.*, vol. 18, no. 1, pp. 6765–6816, 2017.
- [35] J. Bergstra, D. Yamins, and D. Cox, "Making a science of model search: Hyperparameter optimization in hundreds of dimensions for vision architectures," in *Proc. Int. Conf. Mach. Learn.*, 2013, pp. 115–123.
- [36] A. Paszke et al., "Pytorch: An imperative style, high-performance deep learning library," in *Advances in Neural Information Processing Systems*, H. Wallach, H. Larochelle, A. Beygelzimer, F. d'Alché-Buc, E. Fox, and R. Garnett, Eds. Red Hook, NY, USA: Curran Associates, 2019, pp. 8024–8035.
- [37] L. M. B. Bernal, F. Canbaz, A. Droneau, N. F. Friederich, P. C. Cattin, and A. Zam, "Optimizing deep bone ablation by means of a microsecond Er: YAG laser and a novel water microjet irrigation system," *Biomed. Opt. Exp.*, vol. 11, no. 12, pp. 7253–7272, 2020.



CARLO SEPPI received the degree in mathematics from the Mathematical Institute, University of Basel, Basel, Switzerland, in 2009, the B.Sc. and M.Sc. degrees in mathematics, in 2013 and 2015, respectively. He is currently pursuing the Ph.D. degree with the Planning and Navigation Group, Department of Biomedical Engineering, University of Basel. He worked as a Teaching Assistant with the Mathematical Institute during his studies. He started his Swiss Civil Service at the Department of Biomedical Engineering, University of Basel, in 2016. He helped to develop novel visualization methods for nuclear medicine to detect sentinel lymph nodes. His project involves solving inverse problems in medical applications: e.g., finding the position of sentinel lymph nodes using a pinhole collimator (reconstructing a ^{99m}Tc source using a single image of the detector), reconstruction of the medium velocity and the acoustic source with the help of the Helmholtz equation, and extracting information of the acoustic wave during the ablation of tissue.



ANTAL HUCK was born in Basel, Switzerland. He received the B.Sc. and M.Sc. degrees in mathematics from the University of Basel, Switzerland, with a focus on numerical analysis, and the Ph.D. degree from the Faculty of Medicine, University of Basel, in 2019, working on the research project "Segmentation of the Gray and White Matter in the Human Spinal Cord." Since then, he has been a Postdoctoral Researcher with the Group of Prof. Philippe Cattin, Department of Biomedical, University of Basel.



ARSHAM HAMIDI received the B.Sc. degree in physics from the University of Arak, Iran, in 2014, and the M.Sc. degree in photonics from the Institute of Advanced Studies in Basic Science (IASBS), Iran, in 2017. He is currently pursuing the Ph.D. degree with the Biomedical Laser and Optics Group (BLOG), Department of Biomedical Engineering, University of Basel, Switzerland. His main research interests include optical coherence tomography (OCT), biomedical imaging, and smart laser osteotomy.



EVA SCHNIDER received the M.Sc. degree in mathematics from the University of Basel, Switzerland, in 2018, with a thesis on spectral decomposition as a regularization method for inverse problems involving the acoustic wave equation in breast tumor detection. She is currently pursuing the Ph.D. degree with the MIRACLE Planning and Navigation Group of Prof. Philippe Cattin, Department of Biomedical Engineering, University of Basel. Her thesis focuses on the development of machine learning algorithms for distinct bone segmentation in CT images. The results of which will then be used in the group's virtual reality surgical planning systems. She has Interned at Novartis in Basel, and at Google Research, Zürich and London, working on clinical trial data embeddings, machine perception, and on fairness aspects of machine learning for time series predictions. Her research interests include medical image segmentation, neural network architectures for 3-D image modalities, and fairness for machine learning.



MASSIMILIANO FILIPOZZI received the B.Sc. degree in aerospace engineering and the M.Sc. degree in mechatronic engineering from the Politecnico di Torino, Italy, in 2016 and 2019, respectively. In 2018, he spent six months of his studies at the Universidad Nacional de Cordoba, Argentina. He started to work for his master's thesis at the end of 2018 at the Planning and Navigation Group of the MIRACLE project, Department of Biomedical Engineering, University of Basel.

His activity focused on an opto-mechanical position sensor (ASTRAS) for medical tracking systems. Since August 2019, he has started his Ph.D. in the same department continuing the investigation and advancement in the sensor tracking system technology for minimally invasive surgery.



AZHAR ZAM received the B.Sc. degree in medical physics from the University of Indonesia, Depok City, Indonesia, in 2004, the M.Sc. degree in biomedical engineering from the University of Lübeck, Lübeck, Germany, in 2007, and the Ph.D. degree in advanced optical technologies from Friedrich-Alexander University Erlangen–Nuremberg, Germany, with the focus on optical feedback for tissue-specific laser surgery, in 2011. He held a research positions at the University of Waterloo, Waterloo, ON, Canada; the University of Galway, Galway, Ireland; the Toronto Metropolitan University, Toronto, ON, Canada; and the University of California at Davis, Davis, CA, USA, before he joined the Department of Biomedical Engineering, University of Basel, Allschwil, Switzerland, in 2016, as an Assistant Professor, where he founded and leads the Biomedical Laser and Optics Group (BLOG). Since 2022, he has been an Associate Professor of bioengineering at the Division of Engineering, New York University Abu Dhabi (NYUAD). He is also an Associated Faculty with the Department of Biomedical Engineering, Tandon School of Engineering, New York University, Brooklyn, NY, USA. He has authored over 90 peer-reviewed articles, book chapters, books, and patents. His main research interests include the development of smart devices for medical therapy, diagnostics, and monitoring using novel optical technologies, which include smart laser surgery, optical coherence tomography (OCT), photoacoustics, biomedical spectroscopy, AI-aided optical diagnostics and imaging, optical-based smart wearable biosensors, and miniaturized systems.

His main research interests include the development of smart devices for medical therapy, diagnostics, and monitoring using novel optical technologies, which include smart laser surgery, optical coherence tomography (OCT), photoacoustics, biomedical spectroscopy, AI-aided optical diagnostics and imaging, optical-based smart wearable biosensors, and miniaturized systems.



GEORG RAUTER (Member, IEEE) received the degree in mechanical engineering from TU-Graz, the degree in mathematical and mechanical modeling from MATMECA, Bordeaux, and the Ph.D. degree in robotics from ETH Zurich. From 2014 to 2016, he was a Postdoc in rehabilitation robotics at ETH Zurich, University of Southern California, and the University of Zurich. In 2016, he commercialized the gait rehabilitation robot the FLOAT in collaboration with the company Lutz Medical Engineering and the Spinal Cord Injury Center at the Balgrist, Zurich. Since May 2016, he has been heading the BIROMED-Laboratory, as an Assistant Professor of medical robotics and mechatronics at the Department of Biomedical Engineering, University of Basel. Since March 2022, he has been continuing to head the BIROMED-Laboratory, as an Associate Professor of surgical robotics. He has been the Chair of IFToMM Switzerland, since 2019, and an Associate Member of the National Centre of Competence in Research (NCCR) Robotics, since 2020.

Since March 2022, he has been continuing to head the BIROMED-Laboratory, as an Associate Professor of surgical robotics. He has been the Chair of IFToMM Switzerland, since 2019, and an Associate Member of the National Centre of Competence in Research (NCCR) Robotics, since 2020.



PHILIPPE C. CATTIN (Member, IEEE) was born in Switzerland, in 1967. He received the B.Sc. degree from the University of Applied Science, Brugg/Windisch, in 1991, the M.Sc. degree in computer science and the Ph.D. degree in robotics from ETH Zurich, Switzerland, in 1995 and 2003, respectively. From 2003 to 2007, he was a Postdoctoral Fellow with the Computer Vision Laboratory, ETH Zurich. In 2007, he became an Assistant Professor at the University of Basel and promoted to an Associate Professor, in 2015 and to a Full Professor, in 2019. He is the Founder of the Center for Medical Image Analysis and Navigation (CIAN), Medical Faculty of the University of Basel. He is also the Founding Head and the Head of the Department of Biomedical Engineering, University of Basel. He was a Research Fellow at the Brigham and Women's Hospital, Boston, MA, USA, in 2017. His research interests include medical image analysis, image-guided therapy, robotics-guided laser osteotomy, and virtual reality. As a Principal Investigator, he has finished many projects in these areas and published over 250 papers, patents, and book chapters. He is also the founder of three spin-off companies and licensed his patents and software to medical device companies.

As a Principal Investigator, he has finished many projects in these areas and published over 250 papers, patents, and book chapters. He is also the founder of three spin-off companies and licensed his patents and software to medical device companies.

...

Chapter 6

Discussion and Conclusion

“Life is like riding a bicycle. To keep your balance, you must keep moving.”
– Albert Einstein

The objectives of this PhD thesis can be divided into two parts. In the first part, we reconstructed $\text{Tc}^{99\text{m}}$ sources using measurements of γ -rays, and in the second part, we used acoustic waves to extract information of the surroundings.

6.1 Reconstruction of $\text{Tc}^{99\text{m}}$ Sources

The first objective was to reconstruct $\text{Tc}^{99\text{m}}$ sources from a single 2D measurement. One or multiple $\text{Tc}^{99\text{m}}$ sources were placed in front of a detector. A multi-pinhole collimator was mounted between the detector and the sources. The γ -rays were emitted by the $\text{Tc}^{99\text{m}}$ source and detected by the detector. From the resulting detector image, the source position was reconstructed.

6.1.1 Contribution

The main contribution of our work [66], was the improvement of the setup and the optimization of the algorithm from our previous work [79]. In [79] we used a [Weighted Projected Gradient for \$\ell_1\$ -norm Minimization \(WSPGL1\)](#) [60] to reconstruct the $\text{Tc}^{99\text{m}}$ sources. To get a good reconstruction, a careful segmentation of the detector image and some post-processing of the reconstruction were needed. This is due to the fact that the forward problem does not take into account photons penetrating the collimator walls. One of our contributions to this thesis was that we developed a new algorithm. Our fingerprinting algorithm extracts the most dominant information on the detector and assigns it a position in the 3D subspace. Multiple sources are found when this method is applied recursively, without any pre-processing of the measurement and post-processing of the reconstruction. In addition, this method has a much lower computational time and is suitable for real-time implementation.

The second contribution of this work was the design of the collimator. In previous work, the authors of [69, 79] used a pinhole collimator where each pinhole was in the center of a

compartment. The main idea was that we could get depth information from a single measurement, as opposed to the parallel collimator, which requires multiple measurements at different angles to reconstruct the position of the Tc^{99m} source. The advantage of the septum walls is that they reduce the complexity of the forward problem. Depending on which compartment activity was measured, it is possible to limit the area of interest where the Tc^{99m} source is located. This reduces the complexity of the reconstruction. However, such a collimator design has some drawbacks. One of them is that information is lost due to the septum walls. In a regular pinhole pattern, there is no additional information from multiple holes due to the effect of symmetries, or even worse, it can lead to a reconstruction of positions that do not exist. In [66], discussed in Chapter 3, we addressed these challenges. The first step was to remove the septum walls, hence, increasing the complexity of the forward and inverse problem. This increased the computational time of the WSPGL1 algorithm. However, with our new fingerprinting algorithm, it was still feasible in an efficient way. To further improve the reconstruction, we created a new collimator design. We applied the algorithm described in [31] to find new pinhole distributions on the collimator and concluded that a random-looking distribution seems to be a good approach. We confirmed these assumptions in our research, by comparing the regular pinhole collimator with and without septum walls, and a collimator with a random distribution of pinholes.

6.1.2 Conclusion and Future Work

The results of this thesis are very promising. We were able to speed up the algorithm drastically and showed in an experimental and theoretical part that a random-like distribution improves the reconstructions of the Tc^{99m} sources. However, we still face some challenges. We managed to reconstruct multiple sources, but when two sources were located behind each other, it was still challenging. If the sources were located very closed behind each other, the fingerprinting algorithm failed to distinguish them. We believe that by measuring the Tc^{99m} sources from two different angles, the reconstruction can be improved drastically. Another possibility is that using other reconstruction methods, e.g. the CG algorithm in a recursive way, can detect if there are two sources behind each other. With additional constraints and regularization, it might be possible to reconstruct the shape of the Tc^{99m} source instead of just locating it. Another way to improve the results is with a better collimator design. To this end, we propose a different approach to finding the distribution of pinholes on the collimator. Instead of solving the tedious inverse problem to find the pinhole distributions, we can measure the performance of different collimators just by solving the forward problem of the algorithm described in [31]. To this end, we propose to use different distributions and numbers of pinholes and compare their performance. In addition, a realistic *ex-vivo* experiment should be designed that resembles the distribution of Tc^{99m} in the SLN of a patient.

6.2 Reconstruction using Acoustic Waves

The second objective was to extract information from an acoustic wave. To do so, we first used a purely mathematical approach, where we solved the Helmholtz equation to extract the shape, medium velocity, and position of the acoustic source of an area of interest. In the second method,

we used an experimental approach. Here, we ablated hard bone with an [Er:YAG](#) laser, and used the resulting acoustic waves to predict the depth of the cut using a [NN](#).

6.2.1 Contribution

Previous work [63], showed that the Adaptive Eigenspace method works for reconstructing the medium velocity of objects using the Helmholtz equation. With the work of [64], the authors introduced a method, for given basis functions, to reconstruct the bone and the depth of the cut. This was done in a 2D simulation, and one of the challenges they faced was that the acoustic wave generator (the ablation point) was not well known. Our contribution of the work in [65], described in Chapter 4, was to reconstruct the medium velocity and the shape of the acoustic wave generator (source). We used the Adaptive Eigenspace method, which reduced the number of unknown parameters during the optimization process. However, the eigenfunction had to be computed after each iteration, and the number of transducers needed for a good reconstruction was not applicable in our setup. Another challenge was that the method used in a 3D simulation dramatically increased the computational cost and time, making it inapplicable for a real-time feedback system.

Therefore, we took a different approach in [78], described in Chapter 5, where we decided to focus only on the depth of the laser-cut. During the ablation process of the bone with the [Er:YAG](#) laser, we recorded the acoustic waves, and with the [OCT](#) image, the depth of the cut. We trained our [NN](#) using the acoustic measurement as an input to predict the depth of the cut. Our contribution was that we were able to find a correlation between the depth of the cut and the acoustic wave using only a single transducer during the ablation of the bone. A trained [NN](#) solves the forward problem (where the input is the acoustic wave and the output is the predicted depth of the cut) very quickly. Therefore, this approach can be implemented in a real-time matter during tissue ablation.

6.2.2 Conclusion and Future Work

I believe that real-time reconstruction of the shape of the bone and surrounding tissue during bone ablation with an [Er:YAG](#) laser by solving the Helmholtz equation with the Adaptive Eigenspace is not applicable. The required computational resources are too high. In addition, too many transducers are needed. However, I believe that the method can find another use in medical applications. One of them is to improve ultrasound imaging. In ultrasound, the wave generator is well known. Apart from that, the ultrasound image can be a good initial guess for the reconstruction with the Adaptive Eigenspace method. One of the challenges of this method is the computational cost. However, these reconstructed images can be used as a post-analysis, therefore the computational cost is not a limiting factor. Nevertheless, one of the major issues that still needs to be investigated is whether the forward problem of the Helmholtz equation holds up in the real world. Therefore, the 3D simulation should first be confirmed in an *ex-vivo* experiment before analyzing in which field it can be applied.

Using the [NN](#) to predict the depth of cut with the acoustic wave seems very promising and encourages further research. One of the main advantages is that a trained [NN](#) is very efficient in solving the forward problem. However, a disadvantage is that a lot of training data is needed

to have a good predictive NN. It needs to be investigated how realistic the *ex-vivo* experiments are compared to the *in-vivo* experiments. However, first the ablation should be performed in a wet condition to ensure that the acoustic wave correlates with the depth and not with the amount of water in the tissue. Another advantage of wet ablation is that the bone is not carbonized, and deep bone ablation is possible. One of the challenges will be to ensure exactly where the acoustic wave is generated. For example, if the hole is filled with water, then the ablation will not be at the bottom of the hole. Another approach that needs to be investigated is the position of the transducer and whether a contact transducer improves accuracy.

6.3 Final Thoughts

In this thesis, we investigated different approaches to solving inverse problems. One of the main challenges we faced was to find a mathematical model that would hold up in the real world. For this purpose, the NNs have a great advantage. These models require experimental data to work efficiently, so it is not necessary to understand the physics and mathematics behind the experiment to make an accurate prediction. However, this can also be a challenge and even a disadvantage. If the settings of the experiment change, a NN may suffer from inaccuracy due to previously unseen data. Therefore, we believe it is important to bring together the understanding of mathematical reconstruction, physical understanding, and the speed and efficiency of the NN. A closed collaboration between these topics can improve the reconstruction and make it more robust to unseen circumstances.

Chapter 7

Appendix

*“True Beauty shines in many ways, and order is one of them.”
– Friedrich Pukelsheim*

Theorem 7.1. *The highest known prime number found in 2018 ¹ is*

$$p = 2^{82\,589\,933} - 1$$

(a Mersenne prime number) has the following property

$$p \pmod{5} \equiv 1.$$

Proof. Let $n = 82\,589\,933$. Hence, we have

$$\begin{aligned} p \pmod{5} &\equiv 2^n - 1 \equiv 2^n + 4 \equiv 4(2^{n-2} + 1) \equiv -1(2^{n-2} + 1) \\ &\equiv -1(2^{n-2} - 4) \equiv -4(2^{n-4} - 1) \equiv 1(2^{n-4} - 1) \\ &\equiv 2^{n-4} - 1 \equiv \dots \equiv 2^{n-4i} - 1 \equiv 2^{n \pmod{4}} - 1 \\ &\equiv 2^1 - 1 \equiv 1 \pmod{5} \end{aligned}$$

□

Theorem 7.2. *Let $A \in \mathbb{R}^{N \times M}$ be a matrix.*

$$H = A^T A \implies H \text{ is a symmetric matrix.}$$

Proof. Let

$$A = \begin{bmatrix} a_{1,1} & \cdots & a_{1,M} \\ \vdots & \ddots & \vdots \\ a_{N,1} & \cdots & a_{N,M} \end{bmatrix} = [a_{i,j}]_{1 \leq i \leq N, 1 \leq j \leq M} \in \mathbb{R}^{N \times M}.$$

¹June 2022, <https://primes.utm.edu/largest.html>

Hence, we have

$$A^T A = \begin{bmatrix} a_{1,1} & \cdots & \cdots & \cdots & a_{N,1} \\ \vdots & \ddots & \ddots & \ddots & \vdots \\ a_{1,i} & \cdots & a_{j,i} & \cdots & a_{N,i} \\ \vdots & \ddots & \ddots & \ddots & \vdots \\ a_{1,M} & \cdots & \cdots & \cdots & a_{N,M} \end{bmatrix} \begin{bmatrix} a_{1,1} & \cdots & a_{1,j} & \cdots & a_{1,M} \\ \vdots & \ddots & \vdots & \ddots & \vdots \\ \vdots & \ddots & a_{i,j} & \ddots & \vdots \\ \vdots & \ddots & \vdots & \ddots & \vdots \\ a_{N,1} & \cdots & a_{N,j} & \cdots & a_{N,M} \end{bmatrix} = [\hat{a}_{i,j}]_{1 \leq i,j \leq M}.$$

Therefore, we can write for a given i, j in $1 \leq i, j \leq M$

$$\begin{aligned} [\hat{a}_{i,j}] &= a_{1,i}a_{1,j} + \cdots + a_{j,i}a_{i,j} + \cdots + \cdots + a_{N,i}a_{N,j} \\ &= \sum_{n=1}^N a_{n,i}a_{n,j} = \sum_{n=1}^N a_{n,j}a_{n,i}, \\ &= a_{1,j}a_{1,i} + \cdots + a_{i,j}a_{j,i} + \cdots + \cdots + a_{N,j}a_{N,i} \\ &= [\hat{a}_{j,i}] \end{aligned}$$

hence, it is clear that

$$(A^T A)^T = [\hat{a}_{i,j}]_{1 \leq i,j \leq M}^T = [\hat{a}_{i,j}]_{1 \leq i,j \leq M} = [\hat{a}_{j,i}]_{1 \leq i,j \leq M} = A^T A,$$

and therefore $H = A^T A$ is a symmetric matrix of the size $\mathbb{R}^{M \times M}$. □

Lemma 1. Let $H = A^T A$ with $A \in \mathbb{R}^{N \times M}$,

$$\text{if } H \text{ is invertible} \implies \text{rank}(A) = M \leq N$$

Proof. It is clear, that $H \in \mathbb{R}^{M \times M}$ and therefore, if H is invertible, we know that

$$\text{rank}(H) = M.$$

Hence, we get

$$M = \text{rank}(H) = \text{rank}(A^T A) \leq \min(\text{rank}(A^T), \text{rank}(A)) \leq \min(N, M).$$

This equation is only true, if $M \leq N$, and therefore we have

$$\text{rank}(A) = \text{rank}(A^T) = M.$$

□

Theorem 7.3. Let $H = A^T A$ with $A \in \mathbb{R}^{N \times M}$,

$$\text{if } H \text{ is invertible} \implies H \text{ is positive-definite}$$

Proof. We remind the reader that H is positive-definite if and only if

$$x^T H x > 0 \quad \forall x \in \mathbb{R}^M \setminus \{0\}.$$

Since $H = A^T A$ we can write

$$x^T H x = x^T A^T A x = (Ax)^T A x = \|Ax\|_2^2 \geq 0.$$

Case 1, $N = M$: Hence, we have $A \in \mathbb{R}^{M \times M}$ and with Lemma 1 it follows that

$$\text{rank}(A) = M,$$

and therefore, A is invertible. Since A is invertible, we know there exists exactly one solution for

$$Ax = 0,$$

hence, $x = 0$. Therefore we get

$$x^T H x = \|Ax\|_2^2 > 0 \quad \forall x \in \mathbb{R}^M \setminus \{0\}.$$

Case 2, $N > M$: Hence, we have $A \in \mathbb{R}^{N \times M}$ and with Lemma 1 it follows that

$$\text{rank}(A) = M.$$

Since $N > M$, we can deduce that the linear system

$$Ax = y$$

with M unknowns ($x \in \mathbb{R}^M$) has more linear equations, namely N , than unknowns. Because $\text{rank}(A) = M$, we know that there exists at most one solution x for a given y . Hence, we can deduce that $x = 0$ is the only solution for

$$Ax = 0.$$

Therefore we get

$$x^T H x = \|Ax\|_2^2 > 0 \quad \forall x \in \mathbb{R}^M \setminus \{0\}.$$

Hence, we proved the theorem with *Case 1* and *Case 2*. □

Theorem 7.4. *If E is the identity matrix and $\lambda > 0$, then*

$$H = A^T A + \lambda E$$

is positive-definite for all $A \in \mathbb{R}^{N \times M}$.

Proof. For all $x \in \mathbb{R} \setminus \{0\}$ we have $\|x\|_2^2 > 0$ and therefore we can write

$$\begin{aligned} x^T H x &= x^T (A^T A + \lambda E) x = x^T A^T A x + x^T \lambda E x \\ &= (Ax)^T (Ax) + \lambda x^T x = \|Ax\|_2^2 + \lambda \|x\|_2^2 \geq \lambda \|x\|_2^2 > 0 \end{aligned}$$

and hence, H is positive-definite. □

Bibliography

- [1] H. Abbasi, F. Canbaz, R. Guzman, P. C. Cattin, and A. Zam. Highly flexible fiber delivery of a high peak power nanosecond Nd:YAG laser beam for flexiscope applications. *Biomedical Optics Express*, 12(1):444–461, 2021.
- [2] S. Andermatt. Automated brain lesion segmentation in magnetic resonance images. *PhD Thesis, University of Basel, Switzerland*, 2018.
- [3] L. Armijo. Minimization of functions having lipschitz continuous first partial derivatives. *Pacific Journal of mathematics*, 16(1):1–3, 1966.
- [4] M. Augello, C. Baetscher, M. Segesser, H.-F. Zeilhofer, P. Cattin, and P. Juergens. Performing partial mandibular resection, fibula free flap reconstruction and midfacial osteotomies with a cold ablation and robot-guided Er:YAG laser osteotome (CARLO®)—a study on applicability and effectiveness in human cadavers. *Journal of Cranio-Maxillofacial Surgery*, 46(10):1850–1855, 2018.
- [5] M. Augello, W. Deibel, K. Nuss, P. Cattin, and P. Jürgens. Comparative microstructural analysis of bone osteotomies after cutting by computer-assisted robot-guided laser osteotome and piezoelectric osteotome: an in vivo animal study. *Laser in Medical Science*, 2018.
- [6] K.-W. Baek, W. Deibel, D. Marinov, M. Griessen, A. Bruno, H.-F. Zeilhofer, P. Cattin, and P. Juergens. Clinical applicability of robot-guided contact-free laser osteotomy in cranio-maxillo-facial surgery: in-vitro simulation and in-vivo surgery in minipig mandibles. *British Journal of Oral and Maxillofacial Surgery*, 53(10):976–981, 2015.
- [7] K.-W. Baek, W. Deibel, D. Marinov, M. Griessen, M. Dard, A. Bruno, H.-F. Zeilhofer, P. Cattin, and P. Juergens. A comparative investigation of bone surface after cutting with mechanical tools and Er:YAG laser. *Lasers in surgery and medicine*, 47(5):426–432, 2015.
- [8] Y. A. Bayhaqi, A. Hamidi, F. Canbaz, A. A. Navarini, P. C. Cattin, and A. Zam. Deep learning models comparison for tissue classification using optical coherence tomography images: toward smart laser osteotomy. *OSA Continuum*, 4(9):2510–2526, Sep 2021.
- [9] Y. A. Bayhaqi, A. Hamidi, F. Canbaz, A. A. Navarini, P. C. Cattin, and A. Zam. Kalman filtered depth prediction using optical coherence tomography for laser bone cutting. June 2021.

- [10] A. Bayliss, M. Gunzburger, and E. Turkel. Boundary conditions for the numerical solution of elliptic equations in exterior regions. *SIAM Journal on Applied Mathematics*, 42(2):430–451, 1982.
- [11] A. Bayliss and E. Turkel. Radiation boundary conditions for wave-like equations. *Comm. Pure Appl. Math.*, 33(6):707–725, 1980.
- [12] Y. Bengio, A. Courville, and P. Vincent. Representation learning: A review and new perspectives. *IEEE transactions on pattern analysis and machine intelligence*, 35(8):1798–1828, 2013.
- [13] L. M. B. Bernal, F. Canbaz, S. E. Darwiche, K. M. R. Nuss, N. F. Friederich, P. C. Cattin, and A. Zam. Optical fibers for endoscopic high-power Er:YAG laserosteotomy. *Journal of Biomedical Optics*, 26(9):095002, 2021.
- [14] L. M. B. Bernal, F. Canbaz, A. Droneau, N. F. Friederich, P. C. Cattin, and A. Zam. Optimizing deep bone ablation by means of a microsecond Er:YAG laser and a novel water microjet irrigation system. *Biomedical Optics Express*, 11(12):7253–7272, 2020.
- [15] L. M. B. Bernal, F. Canbaz, N. F. Friederich, P. C. Cattin, and A. Zam. Measurements of coupling efficiency of high power Er:YAG laser in different types of optical fibers. *Optical Fibers and Sensors for Medical Diagnostics and Treatment Applications XX*, 11233:178–183, 2020.
- [16] O. Cartiaux, L. Paul, P.-L. Docquier, B. Raucant, E. Dombre, and X. Banse. Computer-assisted and robot-assisted technologies to improve bone-cutting accuracy when integrated with a freehand process using an oscillating saw. *JBJS*, 92(11):2076–2082, 2010.
- [17] A. Cauchy et al. Méthode générale pour la résolution des systemes d’équations simultanées. *Comp. Rend. Sci. Paris*, 25(1847):536–538, 1847.
- [18] S. Deepa, B. A. Devi, et al. A survey on artificial intelligence approaches for medical image classification. *Indian Journal of Science and Technology*, 4(11):1583–1595, 2011.
- [19] W. Deibel, A. Schneider, M. Augello, A. E. Bruno, P. Juergens, and P. Cattin. A compact, efficient, and lightweight laser head for CARLO: integration, performance, and benefits. *Novel optical systems design and optimization XVIII*, 9579:957905, 2015.
- [20] C. Duverney, H. Abbasi, M. Berkelaar, K. Peltari, P. C. Cattin, A. Barbero, A. Zam, and G. Rauter. Sterile tissue ablation using laser light—system design, experimental validation, and outlook on clinical applicability. *Journal of Medical Devices*, 15(1), 2021.
- [21] B. Engquist and A. J. Majda. Absorbing boundary conditions for the numerical simulation of waves. *Math. Comp.*, 31(139):629–651, 1977.
- [22] J. Eriksson. Optimization and regularization of nonlinear least squares problems. *PhD Thesis, Department of Computing Sciences, Umeå University, Sweden*, 1996.

- [23] S. Esterhazy and J. M. Melenk. On stability of discretizations of the Helmholtz equation. *Numerical analysis of multiscale problems*, pages 285–324, 2012.
- [24] M. Eugster, C. Duverney, M. Karnam, N. Gerig, P. C. Cattin, and G. Rauter. Robotic endoscope system for future application in minimally invasive laser osteotomy: first concept evaluation. *IEEE Transactions on Medical Robotics and Bionics*, 4(3):621–633, 2022.
- [25] M. Eugster, J.-P. Merlet, N. Gerig, P. C. Cattin, and G. Rauter. Miniature parallel robot with submillimeter positioning accuracy for minimally invasive laser osteotomy. *Robotica*, 40(4):1070–1097, 2022.
- [26] M. Eugster, E. I. Zoller, P. Krenn, S. Blache, N. F. Friederich, M. Müller-Gerbl, P. C. Cattin, and G. Rauter. Quantitative evaluation of the thickness of the available manipulation volume inside the knee joint capsule for minimally invasive robotic unicondylar knee arthroplasty. *IEEE Transactions on Biomedical Engineering*, 68(8):2412–2422, 2020.
- [27] B. Faludi, E. I. Zoller, N. Gerig, A. Zam, G. Rauter, and P. C. Cattin. Direct visual and haptic volume rendering of medical data sets for an immersive exploration in virtual reality. *International Conference on Medical Image Computing and Computer-Assisted Intervention*, pages 29–37, 2019.
- [28] L. Fasel, N. Gerig, P. C. Cattin, and G. Rauter. Control evaluation of antagonistic series elastic actuation for a robotic endoscope joint. *Journal of Bionic Engineering*, pages 1–10, 2022.
- [29] C. A. Floudas and P. M. Pardalos. Encyclopedia of optimization. *Springer Science & Business Media*, 2008.
- [30] C. F. Gauss. *Theoria motus corporum coelestium in sectionibus conicis solem ambientium*. *FA Perthes*, 7, 1877.
- [31] E. Haber, L. Horesh, and L. Tenorio. Numerical methods for experimental design of large-scale linear ill-posed inverse problems. *Inverse Problems*, 24(5):055012, 2008.
- [32] Y. Han and K. Lee. Convolutional neural network with multiple-width frequency-delta data augmentation for acoustic scene classification. *IEEE AASP Challenge on Detection and Classification of Acoustic Scenes and Events*, 2016.
- [33] K. Hayami. Convergence of the conjugate gradient method on singular systems. *arXiv preprint arXiv:1809.00793*, 2018.
- [34] M. R. Hestenes and E. Stiefel. Methods of conjugate gradients for solving. *Journal of research of the National Bureau of Standards*, 49(6):409, 1952.
- [35] K. Hornik. Approximation capabilities of multilayer feedforward networks. *Neural networks*, 4(2):251–257, 1991.

- [36] J. C. Hu, X. Gu, S. R. Lipsitz, M. J. Barry, A. V. D’Amico, A. C. Weinberg, and N. L. Keating. Comparative effectiveness of minimally invasive vs open radical prostatectomy. *Jama*, 302(14):1557–1564, 2009.
- [37] L. Iafolla, M. Filipozzi, S. Freund, A. Zam, G. Rauter, and P. C. Cattin. Proof of concept of a novel absolute rotary encoder. *Sensors and Actuators A: Physical*, 312:112100, 2020.
- [38] L. Iafolla, M. Filipozzi, S. Freund, A. Zam, G. Rauter, and P. C. Cattin. Machine learning-based method for linearization and error compensation of a novel absolute rotary encoder. *Measurement*, 169:108547, 2021.
- [39] L. Iafolla, L. Witthauer, A. Zam, G. Rauter, and P. C. Cattin. Proof of principle of a novel angular sensor concept for tracking systems. *Sensors and Actuators A: Physical*, 280:390–398, 2018.
- [40] C. Johnson. Numerical solution of partial differential equations by the finite element method. *Courier Corporation*, 2012.
- [41] E. F. Kaasschieter. Preconditioned conjugate gradients for solving singular systems. *Journal of Computational and Applied mathematics*, 24(1-2):265–275, 1988.
- [42] H. Kamper, W. Wang, and K. Livescu. Deep convolutional acoustic word embeddings using word-pair side information. *2016 IEEE International Conference on Acoustics, Speech and Signal Processing (ICASSP)*, pages 4950–4954, 2016.
- [43] M. Karnam, M. Zelechowski, P. C. Cattin, G. Rauter, and N. Gerig. Augmented reality for 6-dof motion recording, preview, and execution to enable intuitive surgical robot control. *Current Directions in Biomedical Engineering*, 8(2):225–228, 2022.
- [44] H. N. Kenhagho, F. Canbaz, R. Guzman, P. Cattin, and A. Zam. Miniaturized optoacoustic feedback sensor for smart laser osteotome: Fiber-coupled fabry-pérot etalon sensor. *Sensors and Actuators A: Physical*, 317:112394, 2021.
- [45] H. N. Kenhagho, G. Rauter, R. Guzman, P. C. Cattin, and A. Zam. Optoacoustic tissue differentiation using a Mach-Zehnder interferometer. *IEEE Transactions on Ultrasonics, Ferroelectrics, and Frequency Control*, 66(9):1435–1443, 2019.
- [46] F. Khan, A. Pearle, C. Lightcap, P. J. Boland, and J. H. Healey. Haptic robot-assisted surgery improves accuracy of wide resection of bone tumors: a pilot study. *Clinical Orthopaedics and Related Research*, 471(3):851–859, 2013.
- [47] D. P. Kingma and J. Ba. Adam: A method for stochastic optimization. *arXiv preprint arXiv:1412.6980*, 2014.
- [48] S. Kiranyaz, T. Ince, and M. Gabbouj. Real-time patient-specific ecg classification by 1-d convolutional neural networks. *IEEE Transactions on Biomedical Engineering*, 63(3):664–675, 2015.

- [49] A. Kumar, J. Kim, D. Lyndon, M. Fulham, and D. Feng. An ensemble of fine-tuned convolutional neural networks for medical image classification. *IEEE journal of biomedical and health informatics*, 21(1):31–40, 2016.
- [50] B. Kyung-Won, M. Dard, H.-F. Zeilhofer, P. Cattin, and P. Jürgens. Comparing the bone healing after cold ablation robot-guided Er:YAG laser osteotomy and piezoelectric osteotomy – a pilot study in minipig mandible. *Lasers in Surgery and Medicine*, 2020.
- [51] C. Lemaréchal. Cauchy and the gradient method. *Doc Math Extra*, 251(254):10, 2012.
- [52] M. Leshno, V. Y. Lin, A. Pinkus, and S. Schocken. Multilayer feedforward networks with a nonpolynomial activation function can approximate any function. *Neural networks*, 6(6):861–867, 1993.
- [53] Q. Li, W. Cai, X. Wang, Y. Zhou, D. D. Feng, and M. Chen. Medical image classification with convolutional neural network. *2014 13th International Conference on Control Automation Robotics & Vision (ICARCV)*, pages 844–848, 2014.
- [54] Z. Li and X. Li. Centroid computation for shack-hartmann wavefront sensor in extreme situations based on artificial neural networks. *Optics Express*, 26(24):31675–31692, 2018.
- [55] D. D. Lo, M. A. Mackanos, M. T. Chung, J. S. Hyun, D. T. Montoro, M. Grova, C. Liu, J. Wang, D. Palanker, A. J. Connolly, et al. Femtosecond plasma mediated laser ablation has advantages over mechanical osteotomy of cranial bone. *Lasers in surgery and medicine*, 44(10):805–814, 2012.
- [56] J. D. Luketich, M. Alvelo-Rivera, P. O. Buenaventura, N. A. Christie, J. S. McCaughan, V. R. Litle, P. R. Schauer, J. M. Close, and H. C. Fernando. Minimally invasive esophagectomy: outcomes in 222 patients. *Annals of surgery*, 238(4):486, 2003.
- [57] P. M. Maloca, B. Faludi, M. Zelechowski, C. Jud, T. Vollmar, S. Hug, P. L. Müller, E. R. de Carvalho, J. Zarranz-Ventura, M. Reich, et al. Validation of virtual reality orbitometry bridges digital and physical worlds. *Scientific Reports*, 10(1):1–9, 2020.
- [58] S. Manavi, T. Renna, A. Horvath, S. Freund, A. Zam, G. Rauter, W. Schade, and P. C. Cattin. Using supervised deep-learning to model edge-FBG shape sensors: a feasibility study. *Optical Sensors 2021*, 11772:79–88, 2021.
- [59] S. Manavi, L. Witthauer, L. Iafolla, A. Zam, G. Rauter, and P. C. Cattin. Temperature-compensated FBG-based 3d shape sensor using single-mode fibers. *Integrated Photonics Research, Silicon and Nanophotonics*, 2018.
- [60] H. Mansour. Beyond l_1 -norm minimization for sparse signal recovery. *2012 IEEE Statistical Signal Processing Workshop (SSP)*, pages 337–340, 2012.
- [61] J. Melenk and S. Sauter. Convergence analysis for finite element discretizations of the Helmholtz equation with dirichlet-to-neumann boundary conditions. *Mathematics of Computation*, 79(272):1871–1914, 2010.

- [62] A. Miller, B. Blott, et al. Review of neural network applications in medical imaging and signal processing. *Medical and Biological Engineering and Computing*, 30(5):449–464, 1992.
- [63] U. Nahum. Adaptive eigenspace for inverse problems in the frequency domain. *PhD Thesis, University of Basel, Switzerland*, 2016.
- [64] U. Nahum and P. C. Cattin. Adaptive eigenspace segmentation. *arXiv preprint arXiv:1810.12771*, 2018.
- [65] U. Nahum, C. Seppi, and P. C. Cattin. Joint inverse medium and optimal control problem for acoustic waves. *Proceedings of the Platform for Advanced Scientific Computing Conference*, pages 1–9, 2019.
- [66] U. Nahum, C. Seppi, P. A. von Niederhäusern, S. Pezold, S. K. Haerle, and P. C. Cattin. Sentinel lymph node fingerprinting. *Physics in Medicine & Biology*, 64(11):115028, 2019.
- [67] U. Nahum, A. Zam, and P. C. Cattin. Bone reconstruction and depth control during laser ablation. *International Workshop on Computational Methods and Clinical Applications in Musculoskeletal Imaging*, pages 126–135, 2018.
- [68] H. Nguendon Kenhagho, F. Canbaz, A. Hopf, R. Guzman, P. Cattin, and A. Zam. Toward optoacoustic sciatic nerve detection using an all-fiber interferometric-based sensor for endoscopic smart laser surgery. *Lasers in Surgery and Medicine*, 54(2):289–304, 2022.
- [69] P. A. v. Niederhäusern, O. C. Maas, M. Rissi, M. Schneebeli, S. Haerle, and P. C. Cattin. Augmenting scintigraphy images with pinhole aligned endoscopic cameras: a feasibility study. *International Conference on Medical Imaging and Augmented Reality*, pages 175–185, 2016.
- [70] K. G. Nilsson, A. Henricson, B. Norgren, and T. Dalén. Uncemented HA-coated implant is the optimum fixation for TKA in the young patient. *Clinical Orthopaedics and Related Research®*, 448:129–139, 2006.
- [71] A. Paszke, S. Gross, F. Massa, A. Lerer, J. Bradbury, G. Chanan, T. Killeen, Z. Lin, N. Gimelshein, L. Antiga, A. Desmaison, A. Kopf, E. Yang, Z. DeVito, M. Raison, A. Tejani, S. Chilamkurthy, B. Steiner, L. Fang, J. Bai, and S. Chintala. Pytorch: An imperative style, high-performance deep learning library. pages 8024–8035. Curran Associates, Inc., 2019.
- [72] F. Pukelsheim. Optimal design of experiments. 1993.
- [73] G. Rauter. The miracle. pages 247–253. Springer, 2020.
- [74] S. M. Roodsari, S. Freund, A. Zam, G. Rauter, and P. C. Cattin. Fabrication and characterization of a flexible FBG-based shape sensor using single-mode fibers. *IEEE Transactions on Biomedical Engineering*, 69(8):2488–2498, 2022.

- [75] E. Schnider, A. Horváth, G. Rauter, A. Zam, M. Müller-Gerbl, and P. C. Cattin. 3d segmentation networks for excessive numbers of classes: Distinct bone segmentation in upper bodies. *International Workshop on Machine Learning in Medical Imaging*, pages 40–49, 2020.
- [76] E. Schnider, A. Huck, M. Toranelli, G. Rauter, M. Müller-Gerbl, and P. C. Cattin. Improved distinct bone segmentation from upper-body CT using binary-prediction-enhanced multi-class inference. *International Journal of Computer Assisted Radiology and Surgery*, pages 1–8, 2022.
- [77] E. Schnider, A. Huck, M. Toranelli, G. Rauter, A. Zam, M. Müller-Gerbl, and P. Cattin. Ensemble uncertainty as a criterion for dataset expansion in distinct bone segmentation from upper-body CT images. *arXiv preprint arXiv:2208.09216*, 2022.
- [78] C. Seppi, A. Huck, A. Hamidi, E. Schnider, M. Filipozzi, G. Rauter, A. Zam, and P. C. Cattin. Bone ablation depth estimation from Er:YAG laser-generated acoustic waves. *IEEE Access*, 10:126603–126611, 2022.
- [79] C. Seppi, U. Nahum, P. A. von Niederhäusern, S. Pezold, M. Rissi, S. K. Haerle, and P. C. Cattin. Compressed sensing on multi-pinhole collimator SPECT camera for sentinel lymph node biopsy. *International Conference on Medical Image Computing and Computer-Assisted Intervention*, pages 415–423, 2017.
- [80] N. Sharma, D. Welker, S. Aghlmandi, M. Maintz, H.-F. Zeilhofer, P. Honigmann, T. Seifert, and F. M. Thieringer. A multi-criteria assessment strategy for 3d printed porous polyetheretherketone (peek) patient-specific implants for orbital wall reconstruction. *Journal of Clinical Medicine*, 10(16):3563, 2021.
- [81] T. Shoaib, D. S. Soutar, D. G. MacDonald, I. G. Camilleri, D. J. Dunaway, H. W. Gray, G. M. McCurrach, R. G. Bessent, T. I. MacLeod, and A. G. Robertson. The accuracy of head and neck carcinoma sentinel lymph node biopsy in the clinically n0 neck. *Cancer: Interdisciplinary International Journal of the American Cancer Society*, 91(11):2077–2083, 2001.
- [82] S. J. Stoeckli, H. Steinert, M. Pfaltz, and S. Schmid. Sentinel lymph node evaluation in squamous cell carcinoma of the head and neck. *Otolaryngology—Head and Neck Surgery*, 125(3):221–226, 2001.
- [83] T. Sullivan. A brief introduction to weak formulations of PDEs and the finite element method. *University of Warwick*, 2020.
- [84] P. A. von Niederhäusern, O. C. Maas, M. Rissi, M. Schneebeli, S. Haerle, and P. C. Cattin. Augmenting scintigraphy images with pinhole aligned endoscopic cameras: a feasibility study. *International Conference on Medical Imaging and Augmented Reality*, pages 175–185, 2016.

- [85] P. A. von Niederhäusern, S. Pezold, U. Nahum, C. Seppi, G. Nicolas, M. Rissi, S. K. Haerle, and P. C. Cattin. Augmenting camera images with gamma detector data. *EJNMMI physics*, 6(1):1–21, 2019.
- [86] P. A. von Niederhäusern, C. Seppi, S. Pezold, G. Nicolas, S. Gkoumas, S. K. Haerle, and P. C. Cattin. Gamma source location learning from synthetic multi-pinhole collimator data. *International Workshop on Machine Learning for Medical Image Reconstruction*, pages 205–214, 2019.
- [87] P. A. von Niederhäusern, C. Seppi, R. Sandkühler, G. Nicolas, S. K. Haerle, and P. C. Cattin. Augmented reality for sentinel lymph node biopsy. *under review*, 2022.
- [88] E. W. Weisstein. Partial differential equation. <https://mathworld.wolfram.com/>, 2002.
- [89] E. W. Weisstein. Lagrange interpolating polynomial. <https://mathworld.wolfram.com/>, 2004.
- [90] S. Wright, J. Nocedal, et al. Numerical optimization. *Springer Science*, 35(67-68):7, 1999.
- [91] M. Żelechowski, B. Faludi, G. Rauter, and P. C. Cattin. Volume rendering-based patient registration for extended reality. *International Workshop on Medical and Service Robots*, pages 115–124, 2022.
- [92] M. Żelechowski, M. Karnam, B. Faludi, N. Gerig, G. Rauter, and P. C. Cattin. Patient positioning by visualising surgical robot rotational workspace in augmented reality. *Computer Methods in Biomechanics and Biomedical Engineering: Imaging & Visualization*, 10(4):451–457, 2022.
- [93] E. I. Zoller, B. Faludi, N. Gerig, G. F. Jost, P. C. Cattin, and G. Rauter. Force quantification and simulation of pedicle screw tract palpation using direct visuo-haptic volume rendering. *International journal of computer assisted radiology and surgery*, 15(11):1797–1805, 2020.

Carlo Seppi

Curriculum Vitae

Contact Information

	Basel Switzerland
e-mail	carlo.seppi@mail.ch

Education

2017–2023	PhD in Biomedical Engineering Department of Biomedical Engineering, University of Basel Supervisor: Prof. Dr. Philippe C. Cattin Topic: <i>Solving Inverse Problems for Medical Applications</i>
2013–2015	MSc in Mathematics , University of Basel Master's thesis: <i>Heilbronn's exponential sums</i>
2009–2013	BSc in Mathematics , University of Basel

Referees

	Prof. Dr. Philippe C. Cattin University of Basel Head of Department of Biomedical Engineering Gewerbstrasse 14 4123 Allschwil, Switzerland
phone	+41 61 207 54 00
e-mail	philippe.cattin@unibas.ch

	Prof. Dr. Azhar Zam New York University Abu Dhabi (NYUAD) Saadiyat Campus, P.O. Box 129188 Abu Dhabi, UAE
	New York University Tandon School of Engineering Brooklyn, NY, 11201, USA
phone	+971 2 628 7736 (UAE) +1 530 638 3452 (USA)
e-mail	azhar.zam@nyu.edu